1967

The plastic deformation behavior of long range ordered iron-aluminum alloys

Henry John Leamy
Iowa State University

THE PLASTIC DEFORMATION BEHAVIOR OF LONG RANGE ORDERED IRON-ALUMINUM ALLOYS

by

Harry John Leamy

A Dissertation Submitted to the
Graduate Faculty in Partial Fulfillment of
The Requirements for the Degree of
DOCTOR OF PHILOSOPHY

Major Subject: Metallurgy

Approved:

Signature was redacted for privacy.

In Charge of Major Work

Signature was redacted for privacy.

Head of Major Department

Signature was redacted for privacy.

Dean of Graduate College

Iowa State University
Of Science and Technology
Ames, Iowa

1967

TABLE OF CONTENTS

INTRODUCTION

The plastic deformation behavior of long range ordered alloys has long been an object of metallurgical research interest. Because perfect dislocations in long range ordered alloys often consist of two or more ordinary dislocations connected by a strip of antiphase boundary (APB), the deformation behavior of such alloys is profoundly affected by the presence of long range order (LRO). In addition, studies of the deformation behavior of alloys which possess LRO are of considerable theoretical interest because these alloys occupy an energetically intermediate position between pure metals and intermetallic compounds. Thus an understanding of their properties may be extrapolated to either extreme.

Because iron and aluminum exhibit many useful physical properties and are relatively abundant, the production of an alloy of these two metals which would exhibit the ferromagnetism and high strength characteristic of steel and the low density and high corrosion resistance of Al was a goal of the early investigators (1) of the Fe-Al alloy system. In fact, the iron rich alloys of these metals do exhibit, in varying degree, many of these desirable properties. Unfortunately, many of the potentially useful alloys in this system

are quite brittle and the search for an understanding of this behavior led to a large number of investigations of Fe-Al phase equilibria.

Among the early investigations of the Fe-Al phase diagram, the work of Bradley and Jay (2) is classic. These authors showed that the iron rich alloys of iron and aluminum form a continuous solid solution from zero to approximately 25 at.% Al and that the alloys accomodate the large atomic misfit through the formation of ordered phases based upon both the B2 and the DO_3 superlattice structures. A generalized illustration of the DO_3 structure in which the unit cell has been divided into four interpenetrating face centered cubic sublattices is shown in Figure 1. For perfect B2 type LRO the sublattice sites of type III and IV are occupied by aluminum atoms while for DO_3 type order only sublattice IV is occupied by aluminum atoms.

Although the work of Bradley and Jay stimulated many other experimental (3-7) and theoretical (8-11) studies of the Fe-Al system, the detailed nature of the reactions which occur in these alloys is still not well understood. A compilation of recent reliable data yields only the obviously incomplete diagram of Figure 2.

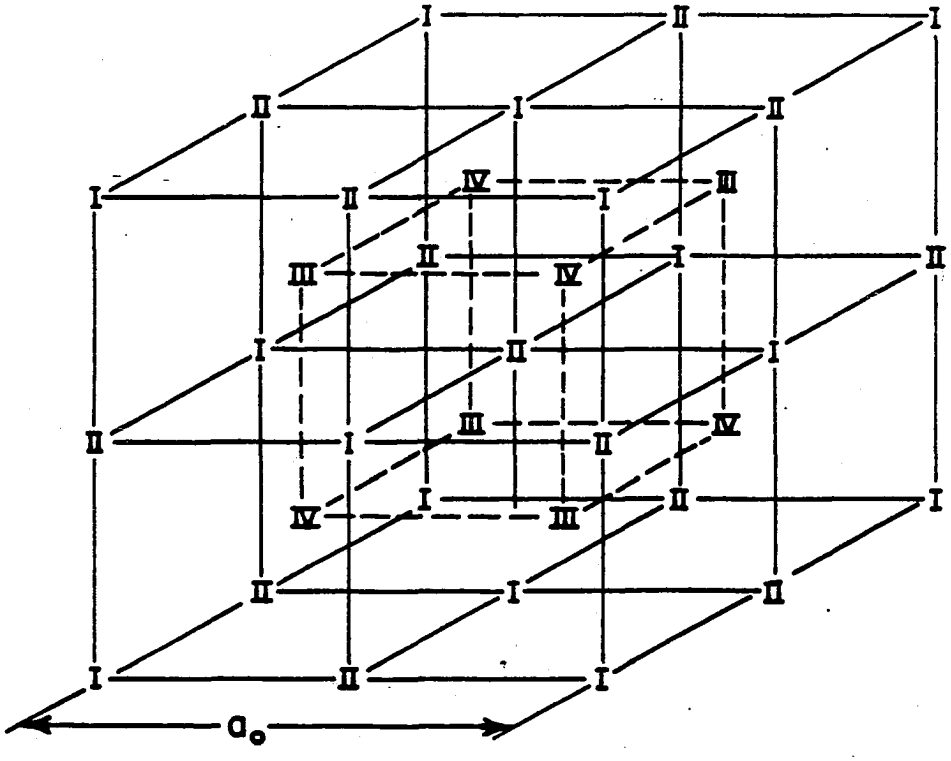

Figure 1. Schematic illustration of the DO_3 unit cell

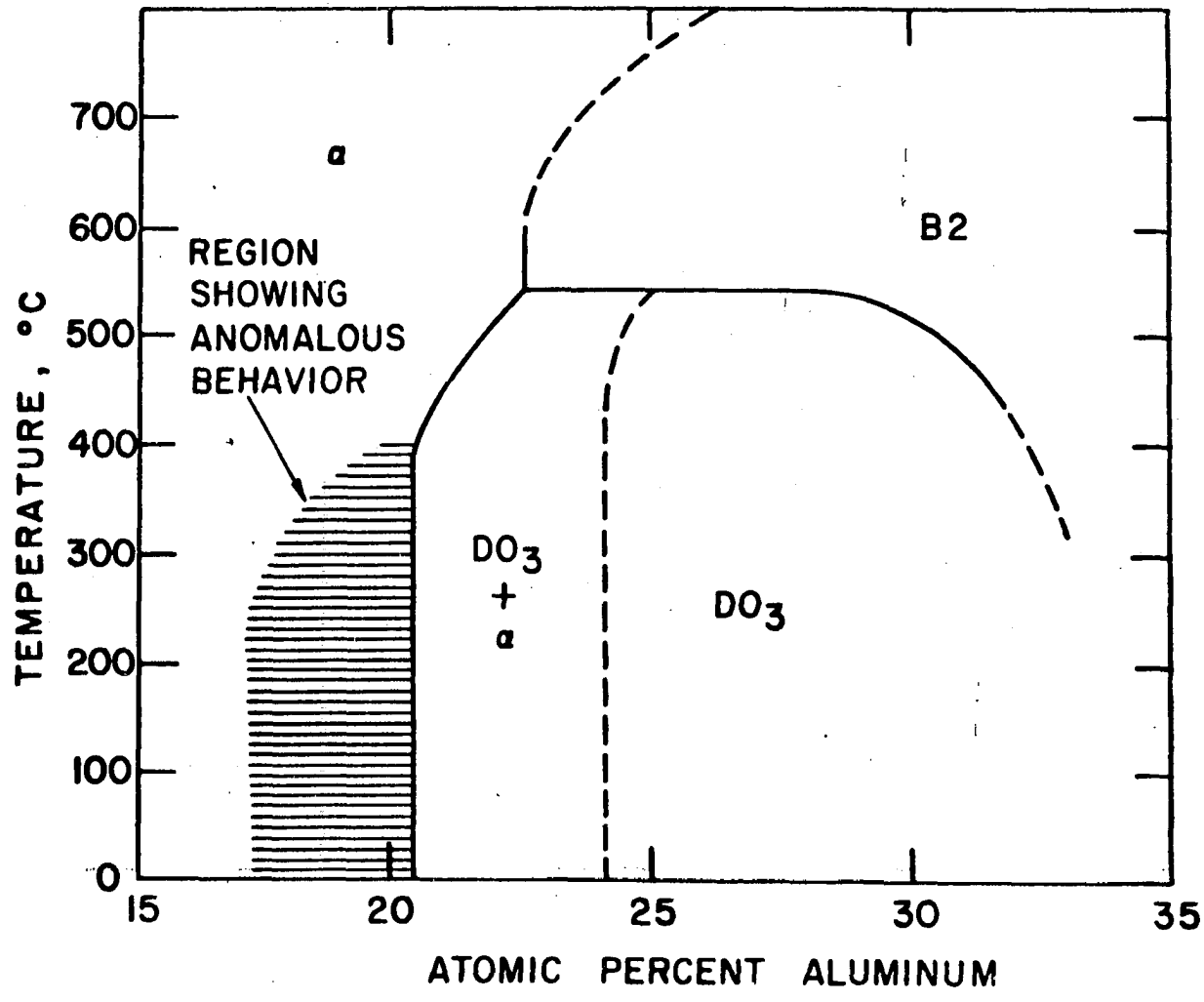

Figure 2. Phase relations for long range ordered Fe-Al alloys

The solid lines shown in Figure 2 are phase boundaries determined by Kayser (12) from discontinuities in plots of electrical resistivity vs. temperature and composition. The boundaries of the "anomalous behavior" region of Figure 2, which were also taken from the work of Kayser (12), describe the region within which the "k state" (12,13) electrical resistance anomaly occurs. The two phase field of Figure 2 is bounded on the aluminum rich side by a dotted line which was determined by combining the lever relations of Lütjering and Warlimont (14,15) with the iron rich boundary position given by Kayser. The transmission electron microscopy (TEM), study of Lütjering and Warlimont, who were first to observe the two phase structure, showed that spherical DO_3 particles precipitate coherently within the disordered phase so that crystals of these alloys are crystallographically continuous and contain only compositional discontinuities.

In addition to these investigations, Swann and Fisher (16) have recently presented transmission electron microscopical evidence for a first order reaction ($\alpha \rightleftharpoons B2$) above 550°C, which is induced by the presence of an external magnetic field while Rimlinger et al. (7) have reported X-ray diffraction experiments which suggest the existence of an additional two

phase field; DO_3 + B2. Although only the incomplete phase relations of Figure 2 are presently available, they do provide an adequate basis for discussion of the plastic deformation behavior of the alloys.

Since the literature concerning LRO in the Fe-Al system is quite voluminous, a complete review is not given here. However, a brief review of the available information concerning the mechanical properties of these alloys is necessary.

Among the many investigations (17-31) of the mechanical properties of Fe-Al alloys, the most complete is that of Kayser (29,30,31). Figures 3-7, which are taken from reference 31, serve to illustrate the salient features of the tensile deformation behavior of the alloys. Figure 3 shows that for dilute alloys, the addition of aluminum to iron effects an increase in the yield stress, 0.2% offset stress, and ultimate tensile stress of the material. For long range ordered alloys, the yield, offset, and ultimate stresses rise rapidly, reach a maximum and then decrease precipitously with increasing aluminum content. In this connection, it should be noted that the composition at which the precipitous decrease in yield stress occurs is dependent upon the temperature of deformation. Figure 4 shows that although the percent elonga-

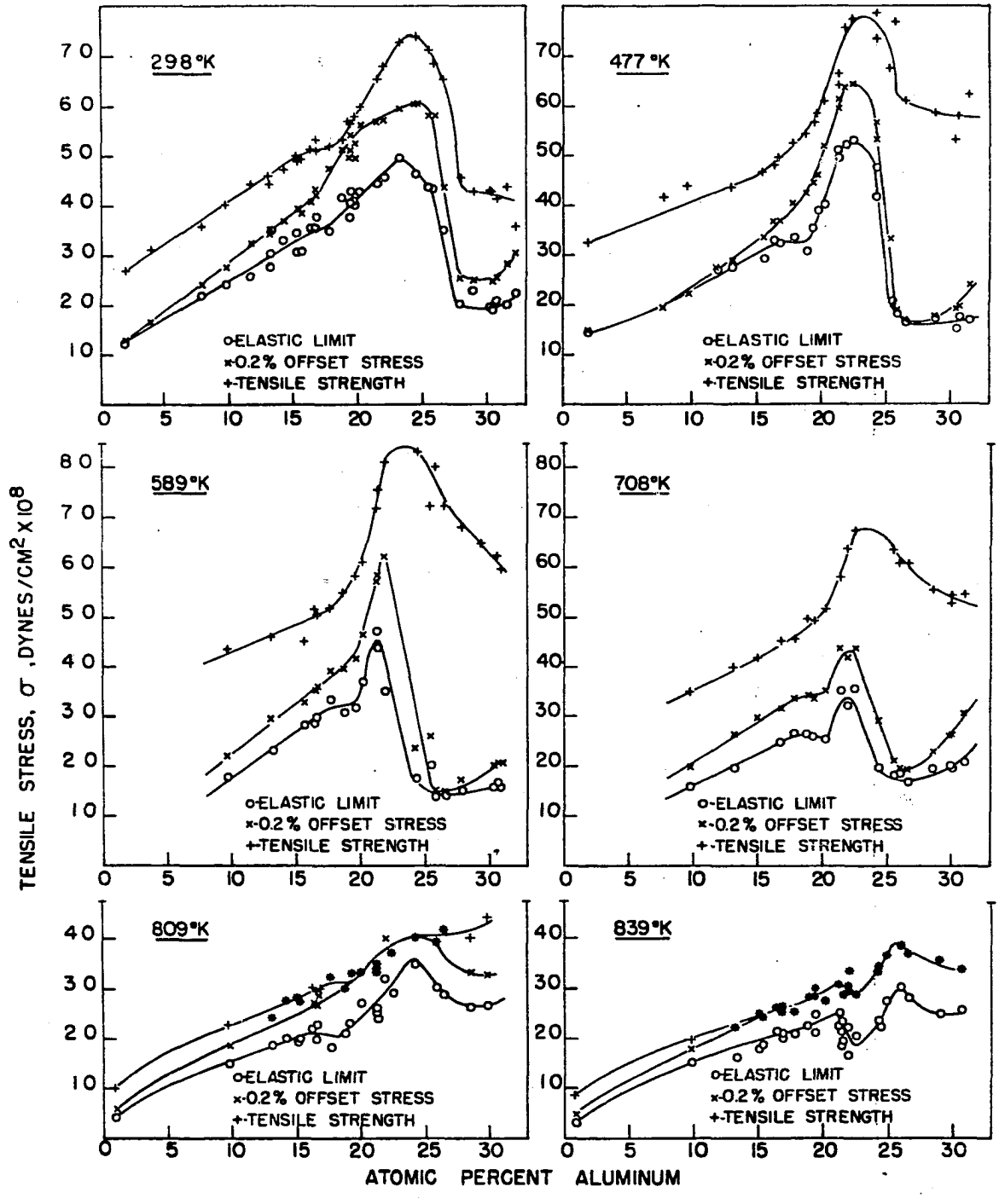

Figure 3. The composition dependence of the elastic limit, 0.2% offset stress, and the tensile strength of Fe-Al alloys tested at various temperatures

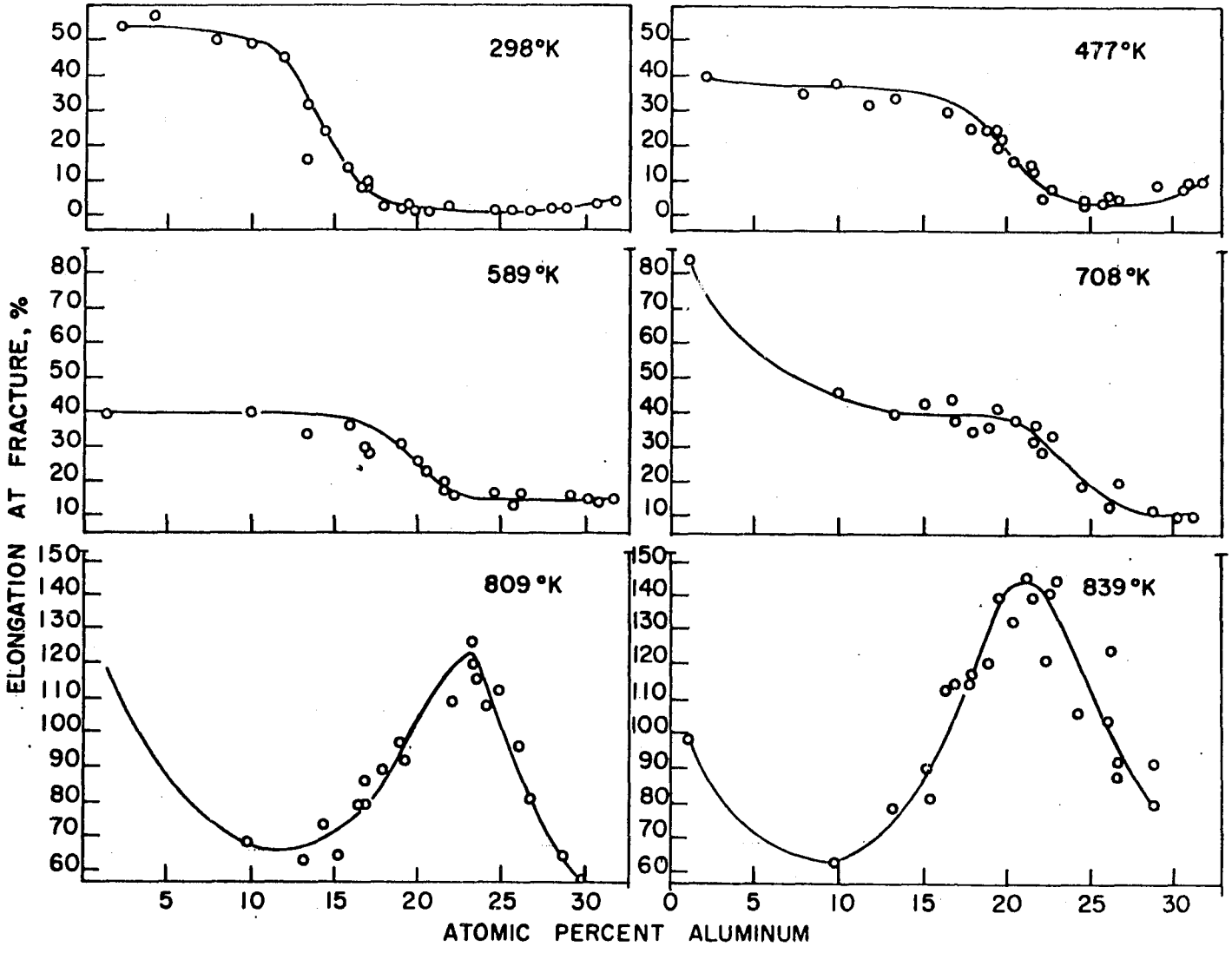

Figure 4. The elongation at fracture for Fe-Al alloys tested in tension at various temperatures

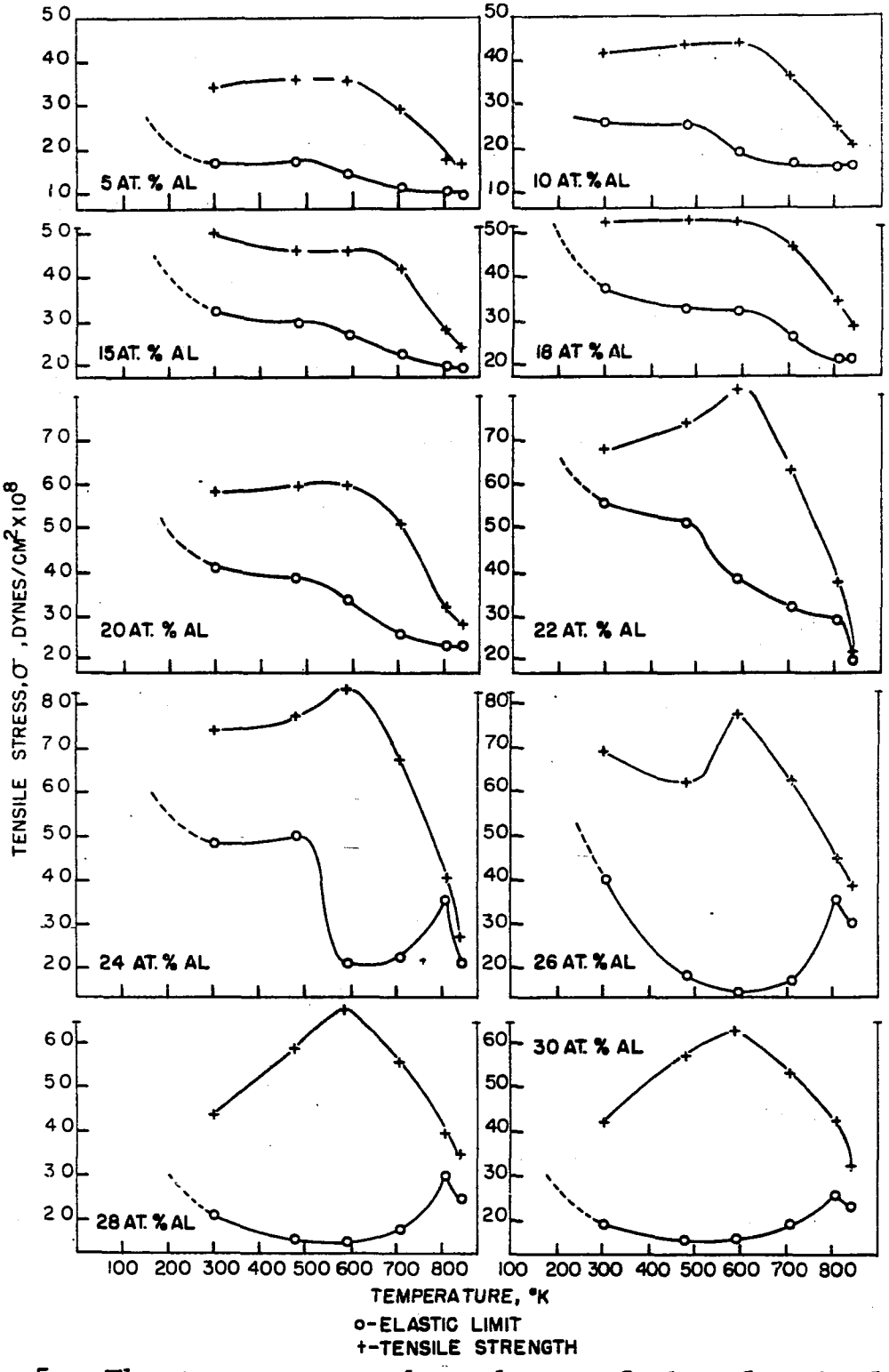

Figure 5. The temperature dependence of the elastic limit and tensile strength of several Fe-Al alloys

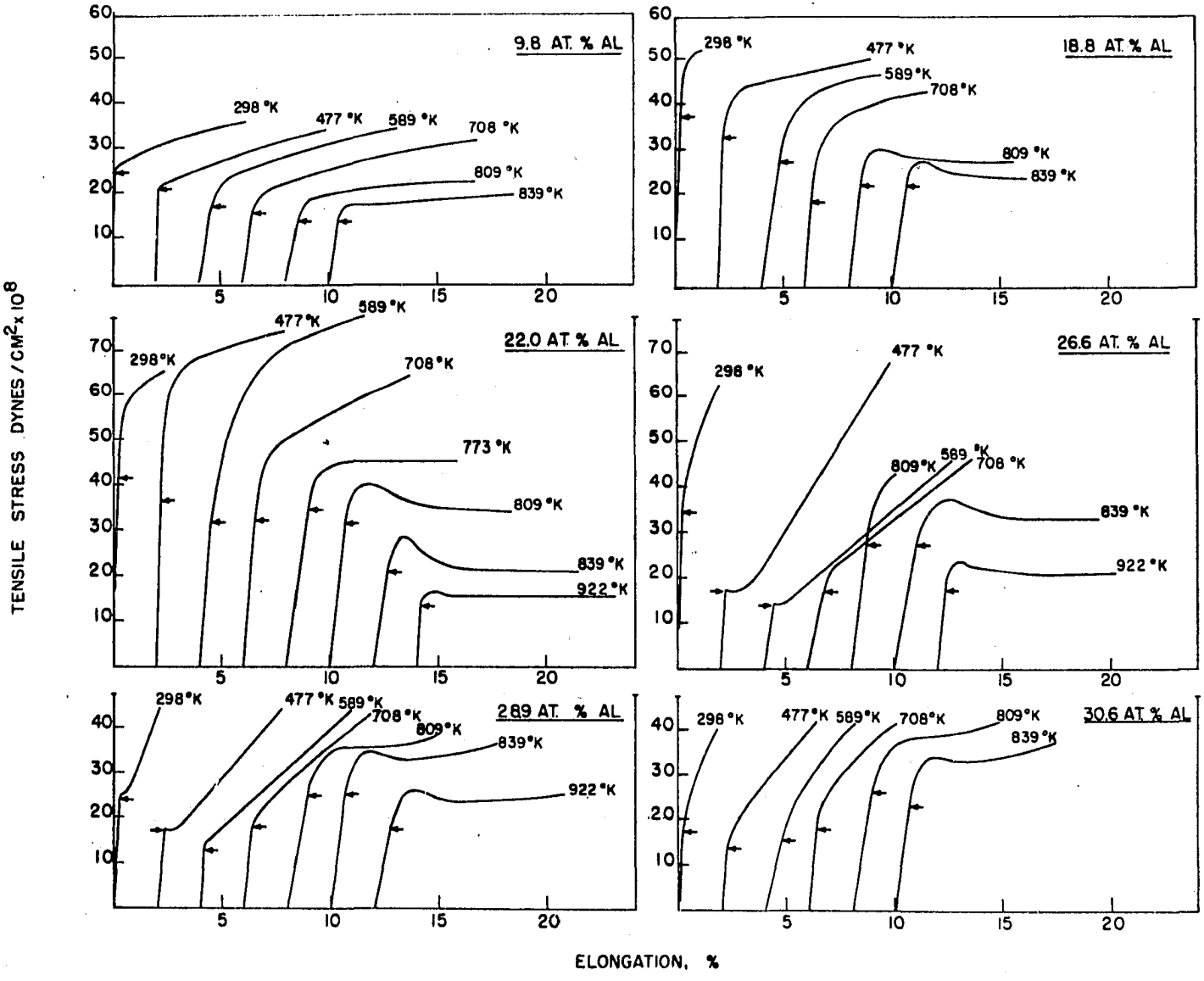

Figure 6. Representative tensile flow stress curves for several Fe-Al alloys

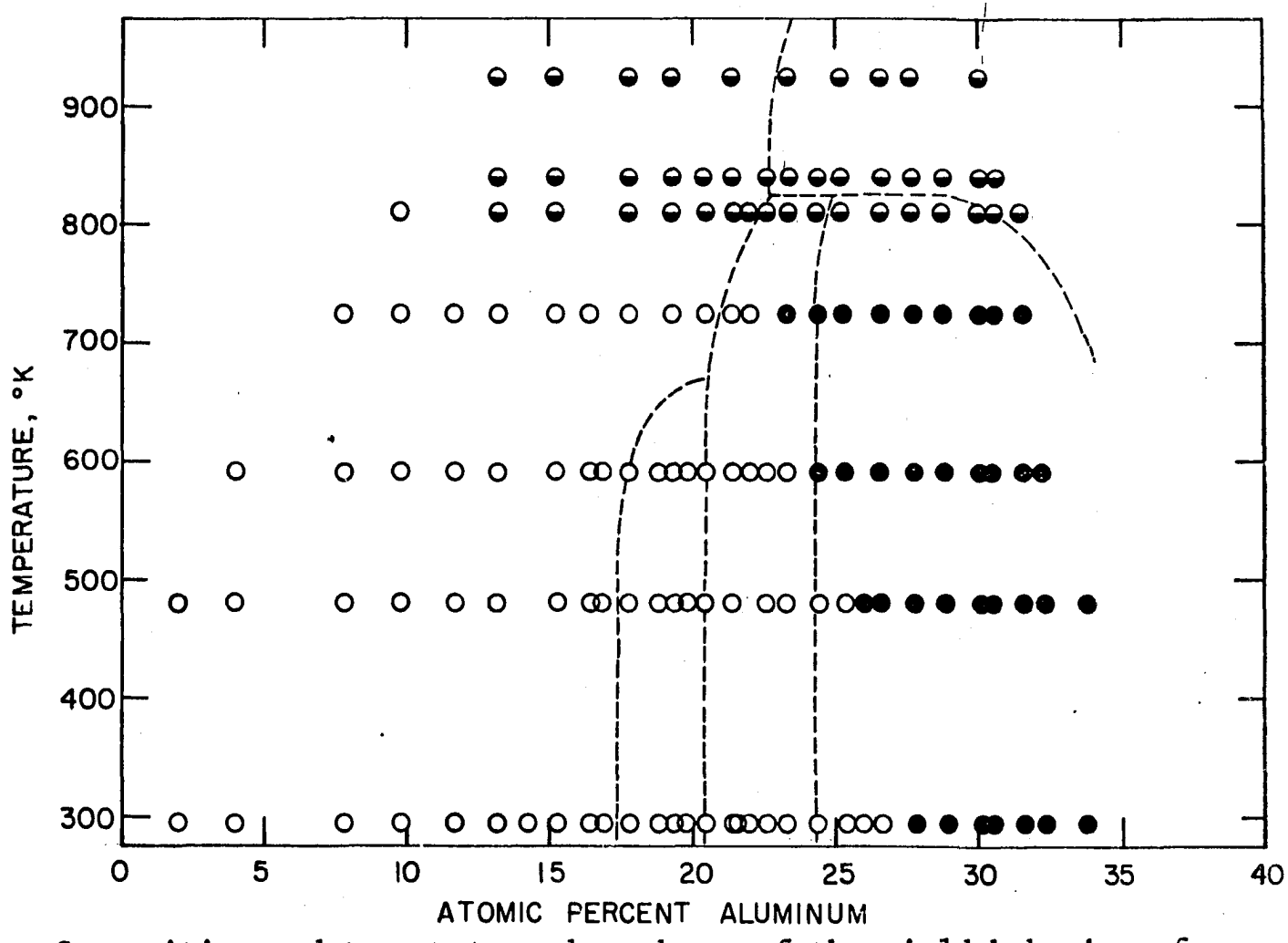

Figure 7. Composition and temperature dependence of the yield behavior of polycrystalline FeAl alloys. ◒ = rounded yield drop; ○ = parabolic work hardening; ● = linear work hardening

tion at fracture is quite small for long range ordered alloys at room temperature, the same alloys possess reasonable ductility when tested at temperatures above the critical temperature for DO_3 long range order, $T_c(DO_3)$. As shown in Figure 5, the temperature dependence of the yield and ultimate stresses are quite usual for the dilute alloys but are quite unusual for the long range ordered alloys. These alloys are characterized by the presence of a temperature and composition dependent decrease in the yield stress which is followed by a well documented (22,23,25,27-31) yield stress increase which occurs near $T_c(DO_3)$. Figure 5 also shows that within the range of temperature for which the yield stress of the alloys is low, the ultimate stress is reasonably high. Thus, for these brittle alloys, a high work hardening rate is inferred. This behavior is illustrated by the typical tensile stress-strain curves of Figure 6. These curves show that, depending upon composition, the low temperature deformation of the ordered alloys is characterized by high yield stresses and an approximately parabolic flow stress curve of low work hardening rate. At somewhat higher temperatures the flow stress curves are characterized by low yield stresses and subsequent linear stress-strain behavior of high work hardening rate. Furthermore, at temperatures near $T_c(DO_3)$ the

deformation of alloys which contain more than about 13 at.% Al is characterized by the presence of a rounded yield drop phenomenon (29). This yield effect has been observed in other materials (32,33) and has been treated theoretically for the case of Al-Mg alloys (34) as well as for the case of Fe_3Al (35).

In summary, the deformation of iron-aluminum alloys may proceed, depending upon temperature and composition, by three macroscopically distinguishable modes: (a) deformation characterized by high yield stresses and a nearly parabolic, low work hardening rate flow stress curve, (b) deformation characterized by a low yield stress, high work hardening rate, linear flow stress curve, and (c) deformation characterized by the presence of a rounded yield point followed by a deformation stage of low work hardening rate. Inspection of Figure 7, where the open points represent test results of type (a), the filled points type (b), and the half filled points those of type (c); shows that the deformation behavior of these alloys is not related in a simple way to the existence of the phase regions of Figure 2.

This thesis is, in essence, an account of a more detailed study of these deformation modes and the possible reasons for

their existence. Since the discussion of this study will draw heavily upon the concepts and language of dislocation theory, a brief review of the major points of this theory, as applied to the case of superlattices in general and Fe-Al alloys in particular, is in order.

Koehler and Seitz (36) first suggested that, if LRO is to be conserved across the slip plane during deformation, the dislocation configuration responsible for deformation in long range ordered alloys might consist of two or more ordinary dislocations bound by a strip of APB, i.e. the so called superlattice dislocation. Brown and Herman (37) first calculated the width of superlattice dislocations in stoichiometric beta brass and Marcinkowski and Brown (38) later extended this calculation to the case of stoichiometric Fe_3Al. These authors predicted that four dislocations of the type $\frac{1}{2}a_o\langle 111\rangle$ would be required for conservation of LRO across the slip plane of this alloy. However, a detailed TEM study of Fe_3Al, performed by these same authors, showed that room temperature deformation of Fe_3Al foils resulted in the formation of APB's by the motion of ordinary $\frac{1}{2}a_o\langle 111\rangle$ type dislocations. These authors (39) also observed thermally produced antiphase domains (APD's) in this alloy and presented a detailed

formulation for the calculation of DO_3 type APB energies.

The existence of the superlattice dislocation concept led to the formulation of a multitude of theoretical models for the deformation behavior of long range ordered alloys. Here again, the large number of published works (40-53) in this area precludes the presentation of a complete review. For this reason the reader is referred to the reviews by Marcinkowski (54), and by Stoloff and Davies (55); and to the theoretical analysis of Marcinkowski and Fisher (56) which is applied to the specific cases of DO_3 and B2 type superlattices.

EXPERIMENTAL PROCEDURE

Polycrystalline Specimen Preparation

Since previous studies of the mechanical properties of Fe-Al alloys were confined to the methods of tensile or hardness testing, and therefore to low strains, an exploratory study of the compressive deformation behavior of several polycrystalline alloy specimens was carried out. Specimens for this study were obtained from two sources. Alloys containing 22.0 and 25.0 at.% Al were produced by arc melting Glidden A104 electrolytic iron and Aluminum Company of America 99.999% aluminum into 150 gram finger ingots. These ingots were swaged in air at 900°C into rods of about ½ inch diameter which were then finish machined to a diameter of 0.220 inches and cut into 0.330 inch lengths. In order to facilitate unambiguous comparison of compression and tension test results, specimen blanks for the remaining compositions studied were machined directly from the threaded grip ends of fractured tensile specimens. These specimens, for which the melting and fabrication methods have already been adequately described (29), were kindly provided by Professor F. X. Kayser. The specimen blanks were homogenized for three days at 900°C and; following homogenization, several specimens of

each composition were analysed for aluminum, carbon and nitrogen. The arc melted specimens typically contained from 30 to 60 ppm of carbon, and nitrogen in 15 to 30 ppm amounts while the specimen blanks supplied by Kayser contained from 80 to 120 ppm of carbon and from 30 to 90 ppm of nitrogen. In order to determine the possible influence of this higher interstitial concentration upon the deformation behavior of the alloys, samples of several compositions were prestrained 3% in compression and subjected to an 800°C wet hydrogen purification treatment of 192 hours duration. Subsequent testing of these specimens, after heat treatment and polishing, revealed no discernable difference in deformation behavior between the hydrogen treated and the untreated specimens even though the carbon and nitrogen concentrations were reduced to levels of from 15 to 30 ppm by the purification treatment. The aluminum analyses verified the accuracy of the values reported by Kayser (29) and gave aluminum content results which were certain to within $\pm$ 0.1 at.% Al.

Prior to heat treatment, which will be described in a subsequent section, the specimen blanks were placed in vycor capsules which were filled with helium and partially evacuated before sealing. Heat treatment of the blanks was carried out

in a noninductively wound electrical resistance furnace within which the temperature was controlled to within $\pm$ 1.0°C. For all polycrystalline specimens, the homogenization treatment produced a uniform equiaxed structure of average grain diameter in the range from 0.2 mm to 0.35 mm which was unaffected by any subsequent heat treatment. Following heat treatment the compression faces of the specimens were carefully polished in a special jig and the cylindrical surfaces were electrochemically polished at 198°K in a 5 volume % perchloric acid in methanol solution.

In order to facilitate metallographic observation of slip lines, planar surfaces were machined parallel to the compression axis on several of the compression specimens. In addition, several sheet tensile specimens were fabricated from sheet stock containing 22.0, 25.0, and 30.0 at.% Al which was also kindly provided by Professor F. X. Kayser. These specimens were machined with a 1½ inch reduced section and a rectangular cross section of 0.25 by 0.125 inches. The interstitial concentration of this material was comparable to that listed previously. The specimens were homogenized in the manner described above and were step cooled in daily 20°C decrements from the homogenizing temperature before metallo-

graphic polishing and subsequent testing.

Single Crystalline Specimen Preparation

Because accurate shear stress and shear strain data and specimens suitable for TEM examination are best obtained from single crystalline specimens, a large number of single crystal deformation experiments were performed in the course of this study. The crystals required for these experiments were grown from the melt by lowering a homogeneous charge through the hot zone of a graphite tube furnace (57) at a rate of 0.125 inches per hour. The homogeneous ingots were produced by arc melting the elemental materials described previously into finger ingots which were then consumably melted into a one inch diameter, water cooled, copper mold. During crystal growth these ingots were contained in flat bottomed ZrO_2 crucibles and were maintained in an atmosphere of helium at a pressure of 35 mm of mercury.

Following crystal growth the crystals were homogenized at 900°C for three days and then slowly cooled at a rate of 20°C per day to 300°C. Further temperature reduction to room temperature was effected by daily 10°C reductions. In order to avoid the possible formation of field induced directional ordering this heat treatment was accomplished in a noninduc-

tively wound resistance furnace within which a dynamic atmosphere of argon was continuously maintained. Chemical analysis of samples cut from the tops and bottoms of the crystals after heat treatment indicated that they contained concentration gradients of approximately 2 at.% Al over their 1½ inch length and that they contained carbon in the range from 40 to 80 ppm and nitrogen in 15 to 30 ppm amounts.

The single crystal compression specimens were electromachined from the single crystals, after orientation by the usual Laue back reflection techniques, and were hand lapped and electrolytically polished before testing. The specimens employed in this study were usually square in cross section with width to height ratios of from 1:1.5 to 1:2.

Polycrystalline Specimen Testing Procedure

The polycrystalline compression specimens described previously were tested, after heat treatment, with an Instron testing machine at a constant crosshead velocity of 0.05 inches per minute. True polycrystalline stress-strain data were calculated from the load-crosshead displacement record, which was corrected for machine elasticity, by assuming that the specimen volume and cylindrical geometry remained constant during the test. Test temperatures other than 298°K were

maintained by already well described techniques (58). In every case the specimens were equilibrated at the test temperature for a period of not less than thirty minutes prior to testing.

Polycrystalline tensile deformation experiments were performed at room temperature with a Tinius Olsen testing machine and one inch gage length extensometer. The specimens were epoxy bonded to steel yokes which were pinned to universal joint grip ends in order to insure uniaxial loading. Since these experiments were carried out in conjunction with a metallographic slip line study, a rather low crosshead velocity of 0.005 inches per minute was employed.

Slip line information was obtained either by direct observation of unloaded tensile or compression specimens or by examination of replicas (59) taken from the unloaded specimens. Tensile specimens were commonly unloaded at strain increments of about ½% in order to obtain surface replicas.

Single Crystalline Specimen Testing Procedure

The single crystalline specimens were tested under conditions identical to those already described for the case of polycrystalline specimens. However, the treatment of the load-crosshead displacement data was somewhat different.

In most published accounts of single crystal compression experiments the specimen shape and orientation change accompanying deformation is calculated by the formulas first given by Schmid and Boas (60). The assumptions upon which the Schmid and Boas formulations are based are: (a) homogeneous deformation throughout the sample volume and (b), complete lack of friction at the compression anvil-specimen interface. If these conditions are reasonably fulfilled the compression test is entirely analogous to the tensile test and results from each may be compared directly. In practice, these conditions are difficult to attain although the use of teflon film lubricant does suffice to reduce the specimen-anvil friction constraint (61). For the alloys studied in this investigation, however, the use of teflon lubricant is not possible because of the high stress levels attained during testing and the crystals do not deform in the simple manner described by Schmid and Boas.

Figure 8 shows a typical specimen, oriented for maximum shear stress on $(\bar{3}12)$ planes, which deformed by "wavy" or "pencil" glide in the $[\bar{1}\bar{1}\bar{1}]$ direction. Inspection of this figure shows that shape changes are consistent with simple $[\bar{1}\bar{1}\bar{1}](\bar{3}12)$ shear deformation only within a well defined band

Figure 8. Deformation geometry of a typical single crystalline compression specimen

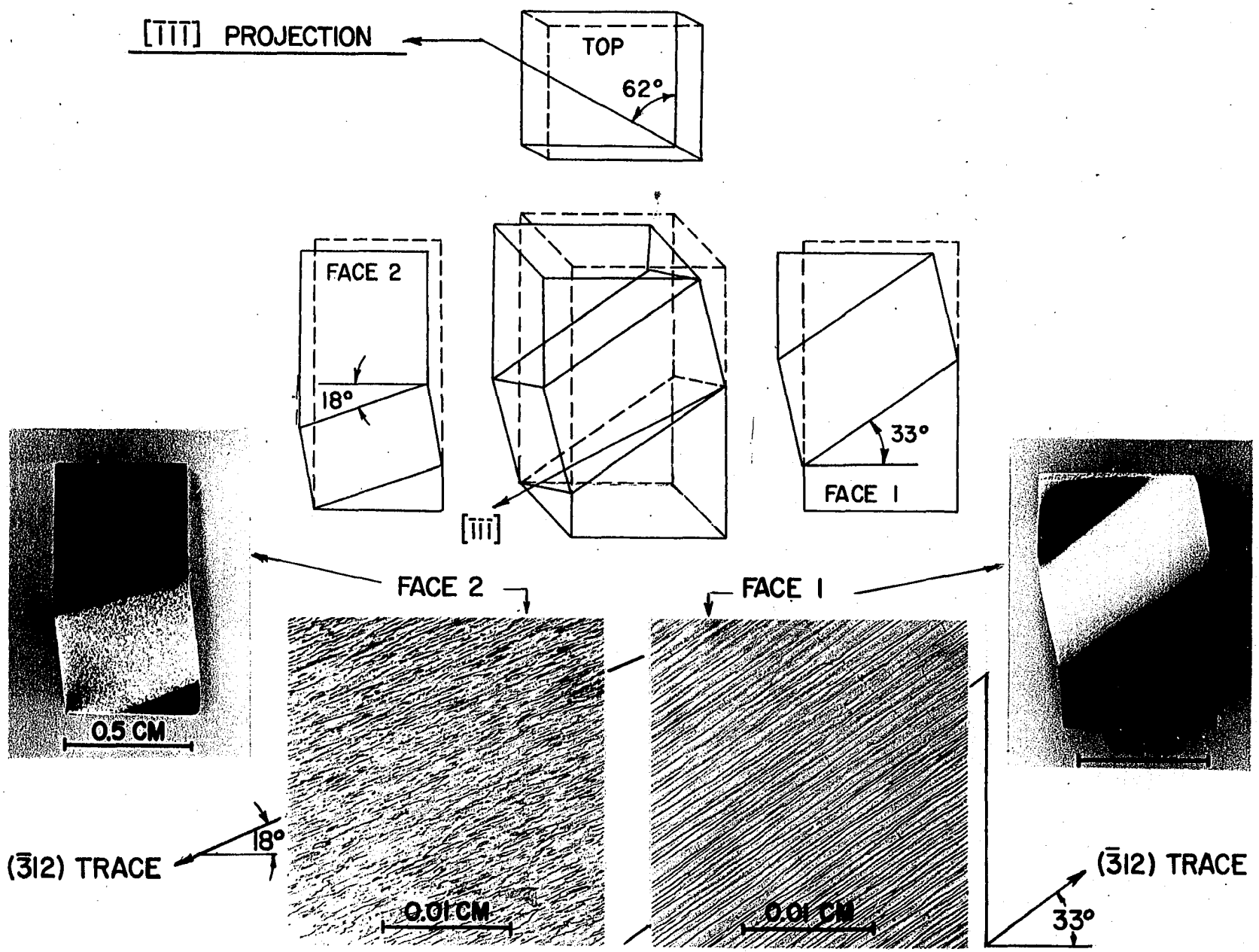
[TTT] PROJECTION
TOP
62°
FACE 2
18°
[TTT]
33°
FACE 1
FACE 2
FACE 1
0.5 CM
(3̄12) TRACE
18°
0.01 CM
0.01 CM
(3̄12) TRACE
33°

which is bounded roughly by the two slip planes of greatest perpendicular separation which do not intersect the compression faces. The higher magnification photographs of Figure 8 show that microscopically observed slip lines are only approximately consistent with the single slip plane model. This behavior is, of course, characteristic of wavy glide and has also been observed in crystals oriented for slip on $\{112\}$ and $\{110\}$ planes. The deformation behavior shown in Figure 8 is a result of specimen geometry and end effects. Slender crystals which contain a region within which no slip planes intersect the compression faces, may be deformed, within this band, quite without constraint provided that the compression faces are free to undergo horizontal translations with respect to the compression axis. That this is the case may be seen by examination of Figure 8. For these cases the lattice rotation and cross sectional area changes are negligible and only the shear deformation of the band itself, which may be easily related to the overall height change of the specimen, need be considered. It should be noted that the deformed band within the crystal shown in Figure 8 is slightly larger than that expected from the geometrical argument given above, due to nonuniform deformation of the specimen corners. In these

cases shear strains may be calculated by direct measurement of the band width. However, for crystals oriented with the slip direction parallel to a set of specimen faces the band width is accurately predicted by geometrical considerations and direct measurement is not necessary. This analysis may be applied to the cases of asymmetric and symmetric double slip, however, symmetric double slip may only be obtained when the specimen cross section is symmetric.

Preparation of Specimens for Transmission Electron Microscopy

Thin foils for use in the TEM portion of this study were prepared by electromachining 0.04 inch thick wafers from the specimens to be examined. These wafers were cemented to a holder and abraded on wet, 600 grit metallographic paper until a thickness of about 0.01 inch was attained. Finally, the electrochemical polishing method mentioned previously was employed for the final thinning process. A careful examination of annealed samples prepared by this method revealed no effects of sample preparation on the defect substructure of the alloys. All transmission electron micrographs were obtained at 100 KV with a Hitachi HU-11A electron microscope.

EXPERIMENTAL RESULTS AND DISCUSSION

The purpose of this section is to present the major portion of the experimental results obtained during this study and to discuss in a qualitative way the main features of these data.

Polycrystalline Specimen Deformation

In order to examine the general effect of long range order on the compressive deformation behavior of Fe-Al alloys, polycrystalline specimens were subjected to the following heat treatments prior to deformation at room temperature: (a) Specimens were cooled from 800°C to room temperature at a rate of 20°C per day in order to maximize the DO_3 APD size and degree of LRO. (b) Specimens were maintained at a temperature of 975°C for three hours and then water quenched in order to minimize the degree of DO_3 type LRO. (c) Specimens were cooled from 800°C to 600°C at a rate of 20°C per day and were held at this temperature for eight hours prior to water quenching in order to maximize the degree of B2 type LRO and APD size. The plastic strain portions of the flow stress curves obtained from specimens heat treated according to these schemes are shown in Figures 9, 10, and 11 for heat treatments (a), (b),

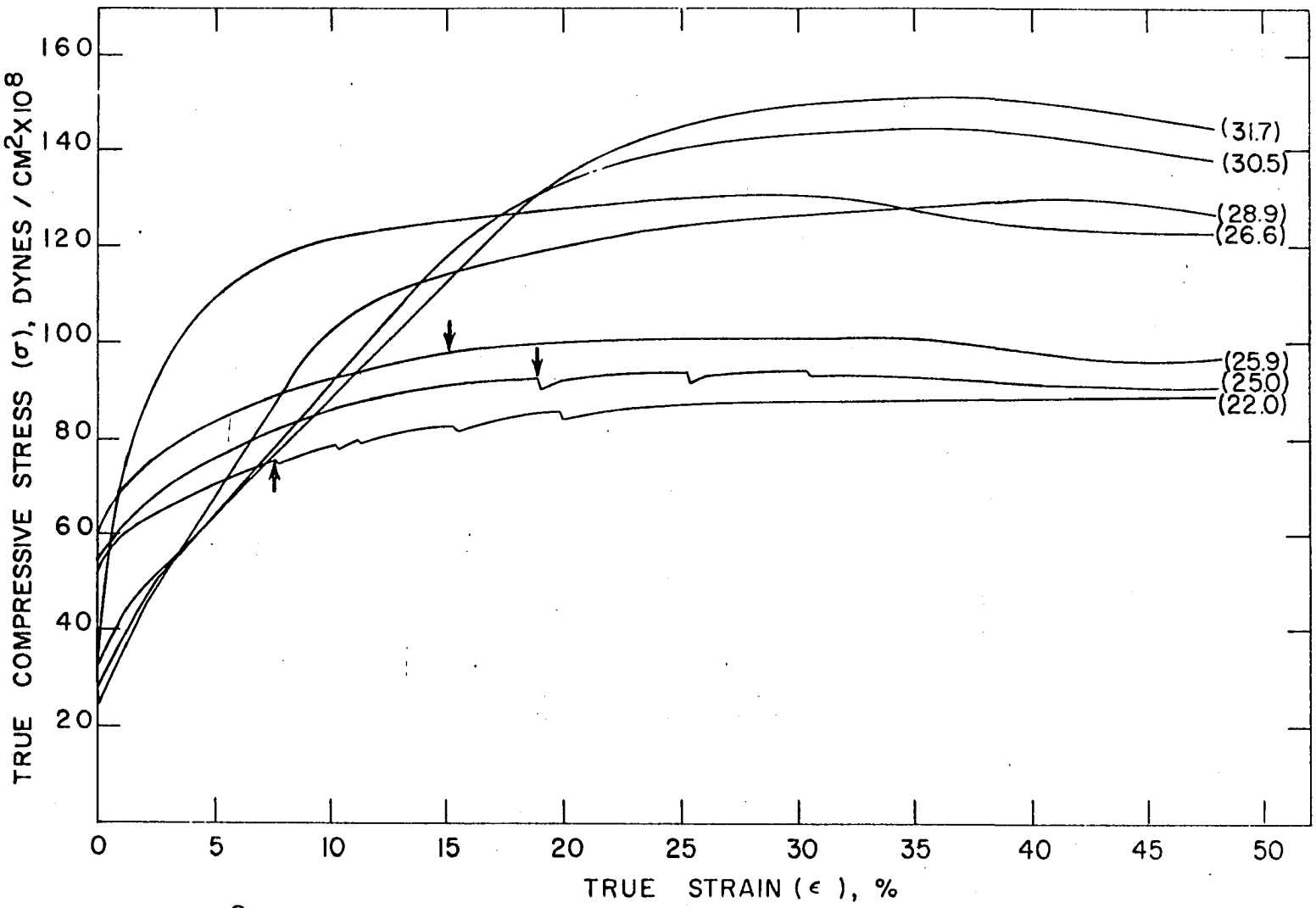

Figure 9. 298°K compressive flow stress curves for slowly cooled, polycrystalline Fe-Al alloys. Arrows mark position of first twin burst

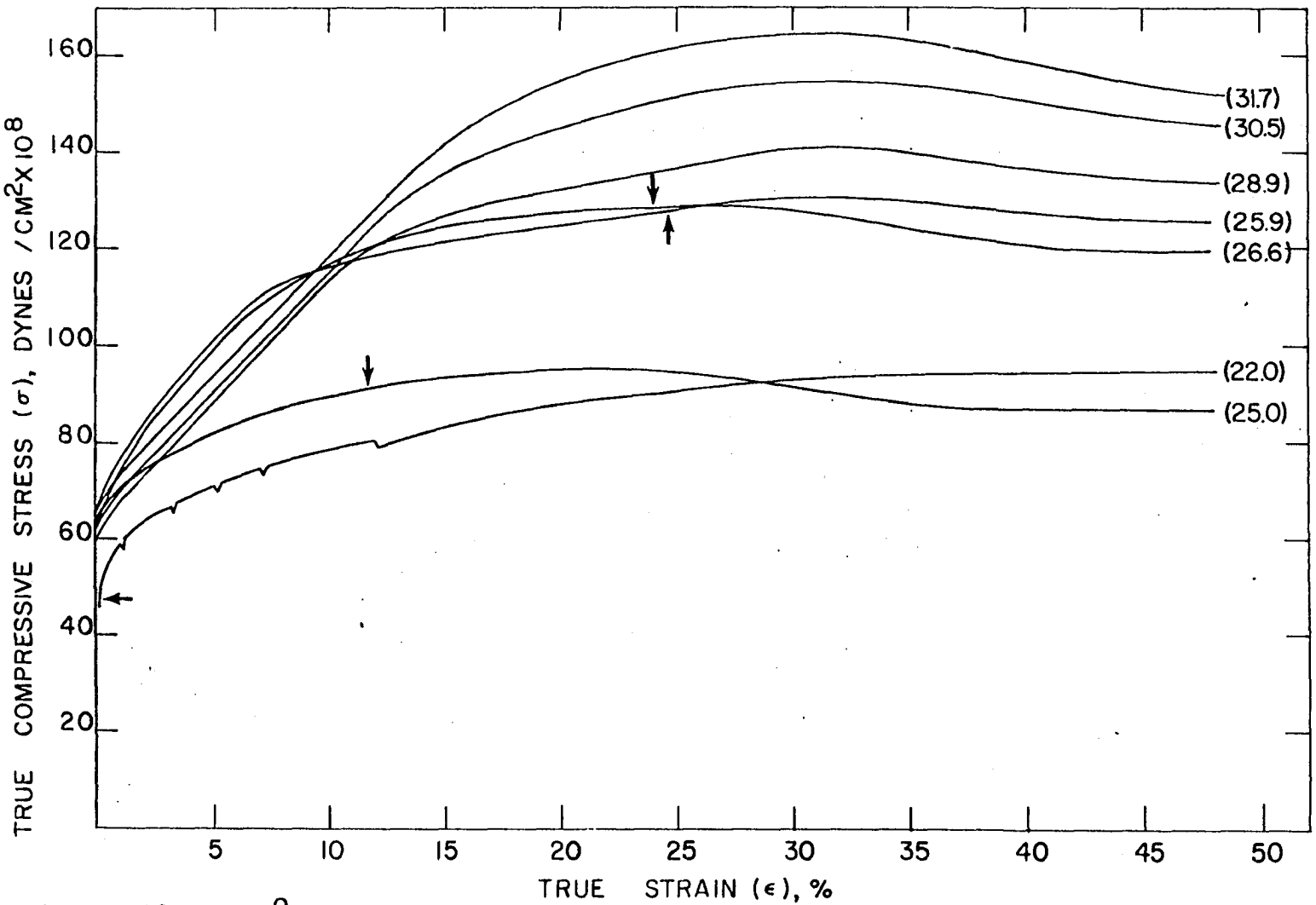

Figure 10. 298°K compressive flow stress curves for polycrystalline Fe-Al alloys quenched from 975°C. Arrows mark position of first twin burst

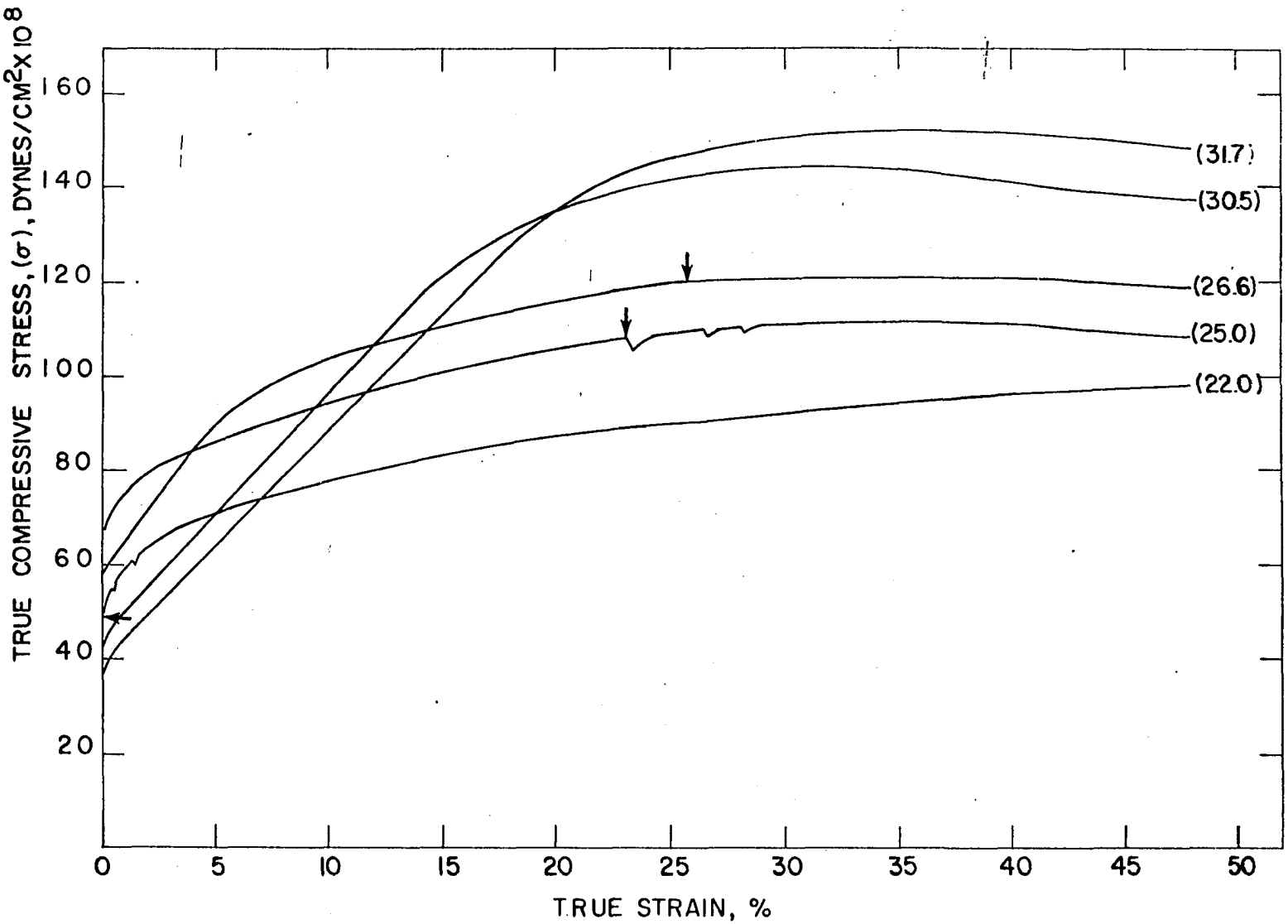

Figure 11. 298°K compressive flow stress curves for polycrystalline Fe-Al alloys quenched from 600°C. Arrows mark position of first twin burst

and (c) respectively.

These curves show that for the slowly cooled alloys, the composition dependence of the elastic limit stresses, σ_o, exhibits a precipitous decrease in good agreement with the data of Figure 3. In addition, the flow stress curves of Figures 9, 10, and 11 exhibit several rather striking features which are not observed at the low strains attained in tension experiments. Specifically, Figure 9 shows that the slowly cooled alloys which yield at low stress levels exhibit two distinct linear work hardening stages. These linear stages are followed at higher stress levels by the familiar iron type behavior which is also observed immediately following the yield in alloys of lower aluminum content. Like the yield stresses, the stress levels at the slope change in the linear portion of the curves, σ_{II}, the linear stage work hardening rates, and the flow stresses corresponding to the onset of the nearly parabolic behavior, σ_V, depend sensitively upon alloy composition. Cursory inspection of Figures 10 and 11 shows, remarkably, that the partial destruction of DO_3 type LRO by quenching serves to eliminate the first linear work hardening stage of deformation. Thus, the presence of the two linear stage behavior, which has also been observed in $Fe_3Si(DO_3)$

(48), is dependent upon the existence of a well ordered DO_3 structure which presumably deforms by the motion of DO_3 type superlattice dislocations. Indeed, Marcinkowski and Chessin (62) have shown that the motion of B2 type superlattice dislocations produces a linear work hardening stage in well ordered FeCo alloys and that the dissociation of these dislocations effects a change from the linear to a parabolic behavior characteristic of pure polycrystalline iron. This reasoning may be extended to the case of DO_3 superlattice deformation behavior as Lakso and Marcinkowski (48) have recently shown.

The various perfect superlattice dislocation types which may occur in the DO_3 structure are shown in Figures 12(a), 12(b) and 12(c) where the possible existence of partial dislocations, i.e. those for which $\bar{b} < \frac{1}{4}a_o\langle 111\rangle$, is neglected. Figure 12(a) shows that the individual dislocations in the predicted DO_3 superlattice dislocation are connected by APB's of two types, designated APB(1) and APB(2). Thus the three distinctly different deformation stages shown in Figure 9 may be associated with the motion of the three variants of the predicted DO_3 superdislocation shown in Figures 12(a), 12(d), and 12(f). Qualitatively, dislocations of type 12(a), which

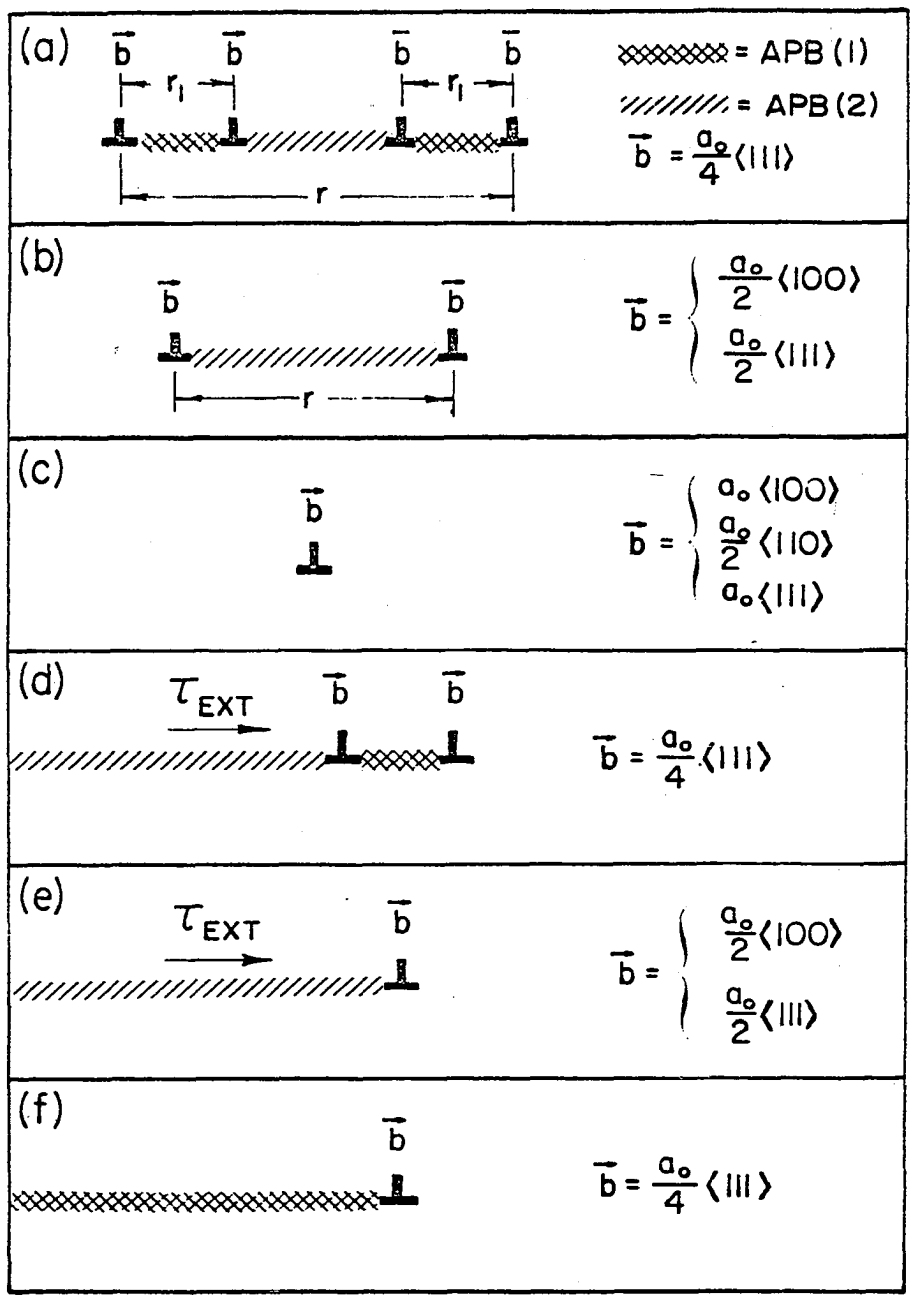

Figure 12. Possible superlattice dislocations in the DO_3 structure

is the experimentally observed dislocation type as will be discussed later, glide under the influence of small applied stresses and interact strongly to produce the first rapid linear work hardening stage. At stress levels above σ_{II} the applied stress is sufficient to overcome the energy associated with the production of APB's of type APB(2) and dislocations of type 12(d) are responsible for further deformation. Finally, at stresses above σ_V, production of APB's of type 1 is possible and dislocations of type 12(f) are free to cross slip so that in analogy with face centered cubic crystals of high stacking fault energy (63), the parabolic behavior results. Application of these arguments to the case of lower aluminum content alloys leads to the conclusion that these specimens deform at the yield by production of APB's. Therefore, a complete explanation of the deformation behavior of these alloys must include a description of the conditions required for DO3 superlattice dislocation production.

Marcinkowski and Brown (39) have shown that the energies, γ_1 and γ_2, of APB(1) and APB(2) in stoichiometric Fe_3Al are associated with nearest neighbor and next nearest neighbor atom pair violations respectively. However, this analysis is not valid for nonstoichiometric alloys. Therefore, an analy-

tical description of γ_1 and γ_2 for nonstoichiometric alloys is required for quantitative implementation of the qualitative scheme outlined above.

APB's in long range ordered structures are completely characterized by a displacement vector, $\bar{p}$, and plane normal, $\bar{n}$. Those which may be formed by APD growth or by the motion of imperfect superlattice dislocations of the types shown in Figures 12(d), 12(e) and 12(f), are characterized by displacement vectors which are whole number multiples of the interatomic distance vectors. Thus $\bar{p}_{APB(1)} = \frac{1}{4}a_o\langle 111\rangle$ and $\bar{p}_{APB(2)} = \frac{1}{2}a_o\langle 111\rangle$ or $\frac{1}{2}a_o\langle 100\rangle$. APB's for which $\bar{p}$ is not identical to an interatomic distance vector are always associated with an atomic fault, e.g. that produced by the motion of a twinning dislocation where, for the DO_3 lattice, $\bar{p}_{APB(T)} = \bar{b}_{twin} = \frac{1}{6}a_o\langle 111\rangle$. It should be noted that the production of APB's by the glide motion of the imperfect superlattice dislocations mentioned above involves the formation of equal numbers of AA and BB pairs. This condition may be described by the equality:

$$\bar{p}\cdot\bar{b} = 0 \qquad (1)$$

The energies of APB's in any structure may be calculated if $\bar{p}$ and $\bar{n}$ and the energies and probabilities of occurrence of

the various atom pair types are known. For boundaries which satisfy Equation 1, only the quasichemical energy difference factor, E, where

$$E = E_{AB} - \frac{E_{AA} + E_{BB}}{2} \qquad (2)$$

is required since production of the APB may be represented by the quasichemical equation $2AB \rightleftharpoons AA + BB$. If, as is often the case for APB's produced by atom diffusion, Equation 1 is not satisfied, unequal numbers of AA and BB pairs are formed upon destruction of AB pairs and relation 2 is applicable only when $E_{AA} = E_{BB}$. For the DO_3 superlattice the required pair probabilities may be calculated from the long range order parameters S_{NN} and S_{NNN} (10). These parameters are defined in terms of the sublattices shown in Figure 1 as:

$$S_{NN} = 2(x - {}^{I}f_{Al}^{II}) \text{ and} \qquad (3)$$

$$S_{NNN} = f_{Al}^{IV} - f_{Al}^{III} \qquad (4)$$

where ${}^{I}f_{Al}^{II}$ is the fraction of type I or II sites occupied by aluminum atoms, f_{Al}^{IV} and f_{Al}^{III} are the aluminum occupied fractions of sites of type IV and III respectively, and x is the aluminum concentration of the alloys. The three basic states of order which occur in Fe-Al alloys may be described in terms of S_{NN} and S_{NNN} as follows:

(a) maximum disorder, $S_{NN} = S_{NNN} = 0$ for all x

(b) maximum B2 order, $S_{NN} = 2x$, $S_{NNN} = 0$ for all $x \leq 0.50$

(c) maximum DO_3 order, $S_{NN} = 2x$ for all $x \leq 0.50$ (5)

$S_{NNN} = 4x$ for $0 \leq x \leq 0.25$

$S_{NNN} = 2(1-2x)$ for $.25 \leq x \leq 0.50$.

Combination of Equations 3 and 4 with the following relation:

$$2({}^{I}f_{Al}^{II} - x) + (f_{Al}^{III} - x) + (f_{Al}^{IV} - x) = 0, \quad (6)$$

which is a statement of the conservation of lattice sites, yields the following equations for the sublattice aluminum occupation probabilities:

$${}^{I}f_{Al}^{II} = \tfrac{1}{2}(2x - S_{NN}), \quad (7a)$$

$$f_{Al}^{III} = \tfrac{1}{2}(S_{NN} + 2x + S_{NNN}), \quad (7b)$$

and $$F_{Al}^{IV} = \tfrac{1}{2}(S_{NN} + 2x - S_{NNN}). \quad (7c)$$

These probabilities are sufficient for the calculation of the order and composition dependence of APB energies, γ, for APB's which satisfy Equation 1. For the energies of the specific APB's of Figure 12, i.e. γ_1 and γ_2, the following equations are obtained:

$$\gamma_1(\bar{p}=\tfrac{1}{2}a_o\langle 111\rangle, \bar{n}=\langle 110\rangle) = [4S_{NN}{}^2E_{NN}+(S_{NNN}{}^2-S_{NN}{}^2)]2\sqrt{2}/a_o{}^2 \quad (8a)$$

$$\gamma_2(\bar{p}=\bar{a}_o/2\langle 111\rangle, \bar{n}=\langle 110\rangle) = [2S_{NN}{}^2E_{NNN}]2\sqrt{2}/a_o{}^2 \quad (8b)$$

where E_{NN} and E_{NNN} are pair energies as defined in Equation 2 for first and second neighbor atom pairs, respectively. Although these relations apply to the specific case of $\bar{n} = \langle 110 \rangle$, they may be easily modified for application to other planes in the $\langle 111 \rangle$ zone by multiplying E_{NN} and E_{NNN} by the appropriate atom pair density factors first given by Flinn (42). Marcinkowski and Brown (38) have shown that this leads to an energy difference of only about 14% between the $\bar{n} = \langle 110 \rangle$ low energy orientation and the $\bar{n} = \langle 211 \rangle$ high energy orientation.

In addition, the energy of the APB produced by the motion of the twin shear dislocation, γ_T, may be written:

$$\gamma_T(\bar{p} = \frac{1}{6}a_o\langle 111\rangle,\ \bar{n} = \langle 112\rangle) = [(4S_{NN}^2 - S_{NNN}^2)E_{NN} + (2S_{NNN}^2 - 5S_{NN}^2 - 4x^2 + 4xS_{NN})E_{NNN}]2\sqrt{2}/\sqrt{3}\ a_o^2 \quad (9)$$

It should be noted that this equation is only as certain as the values of E_{NN} and E_{NNN}, which are expected to change with interatomic separation across the faulted $\{112\}$ plane. Thus, pair energies determined by measurement of γ_1 and γ_2 are not strictly applicable to this case. This same restriction applies to the case of all APB's in nonstoichiometric alloys where the presence of size induced static displacements, magnetic interactions, and compositional variations in electronic structure seriously complicate the calculation of pair

energies from basic considerations. For these reasons pair energies are most successfully obtained by less direct methods such as superdislocation spacing measurements, pseudopotential calculations, or consideration of alloy deformation characteristics. Contrary to the assumptions of the simple quasichemical theory, pair energies determined by these methods generally exhibit a composition dependence. For well ordered Fe-Al alloys, a combination of all three methods is most appropriate.

The energies of APB's in long range ordered alloys may be determined from alloy deformation characteristics only when all contributions to the flow stress can be separated from that due to APB production. In general, the stress required to move dislocations of the type shown in Figure 12 is given by:

$$\tau = \sigma/\bar{m} = \tau_{APB} + \tau_f + \tau_g + \tau_s \qquad (10)$$

where $\bar{m}$ is the average orientation factor, τ_{APB} is the stress required for APB production, τ_f is the lattice friction stress, τ_g is the grain boundary contribution to the friction stress, and τ_s is the structure dependent friction stress, i.e. the stress required to overcome the impedance to dislocation motion due to APD structure, LRO inhomogeneities, dislocation distributions, and vacancy and interstitial-dislocation inter-

actions. Although contributions to τ_s have been estimated for several simplified situations (33,43,44,46,47), detailed calculation of this factor remains a central problem in the theory of ordered alloy deformation. τ_{APB} is given simply as:

$$\tau_{APB} = \frac{\gamma_{APB}}{\bar{b}} \tag{11}$$

where $\bar{b}$ is the total Burger's vector of the dislocation under consideration. The lattice friction stress, τ_f, may for purposes of this analysis be taken equal to that for pure iron while τ_g may be neglected because of the large grain size of the specimens under consideration. For well ordered alloys of large APD size, the τ_s contribution to the yield strength is expected to be small. Furthermore, if τ_s is assumed small with respect to τ_{APB} at all strains, the stresses required to move dislocations of type 12(a), 12(d), and 12(f) are given as:

$$\tau_{12(a)} = \frac{\sigma_o}{\bar{m}} \simeq 4(\tau_f)_{Fe} + \tau_s \tag{12a}$$

$$\tau_{12(d)} = \frac{\sigma_{II}}{\bar{m}} \simeq \tau_{APB(2)} + 2(\tau_f)_{Fe} + \tau_s \simeq \frac{\sigma_o}{\bar{m}} - 2(\tau_f)_{Fe} + \tau_{APB(2)} \tag{12b}$$

$$\tau_{12(f)} = \frac{\sigma_V}{\bar{m}} \simeq \tau_{APB(1)} + (\tau_f)_{Fe} + \tau_s \simeq \tau_{APB(1)} + \frac{\sigma_o}{\bar{m}} - 3(\tau_f)_{Fe} \tag{12c}$$

where, in accord with earlier arguments, σ_{II} and σ_V are taken as the lowest stresses at which production of APB's of type APB(2) and APB(1) can occur. Application of these results to the data of Figure 9 with $\bar{m}$ taken equal to two yields the τ_{APB} values shown as circles in Figure 13. For alloys containing more than 25.9 at.% Al σ_o and σ_{II} are well defined. Determination of σ_V, however, is less unambiguous and for this reason was taken at an offset of 0.2% from the preceding linear stage. For alloys containing less than 26.6% Al, σ_o, σ_{II}, and σ_V are virtually nonexistent. As noted by other authors (28), the flow stress data for these alloys form continuous curves with no macroscopic indication of the onset of plastic flow. If, for the flow stress curves of the specimens of 25.0 and 25.9 at.% Al, the point of deviation from linearity is taken as the yield stress, and if production of APB's of type APB(2) is assumed to occur at this stress, then the approximate $\tau_{APB(2)}$ values shown in Figure 13 may be obtained by subtracting $2(\tau_f)_{Fe}$ from these stress levels.

The solid lines in Figure 13 show the composition dependence of $\tau_{APB(1)}$, $\tau_{APB(2)}$, and $\tau_{APB(T)}$ as calculated from Equations 8a, 8b, and 9. For these calculations maximum DO_3 type LRO was assumed and a_o values were taken from the work of

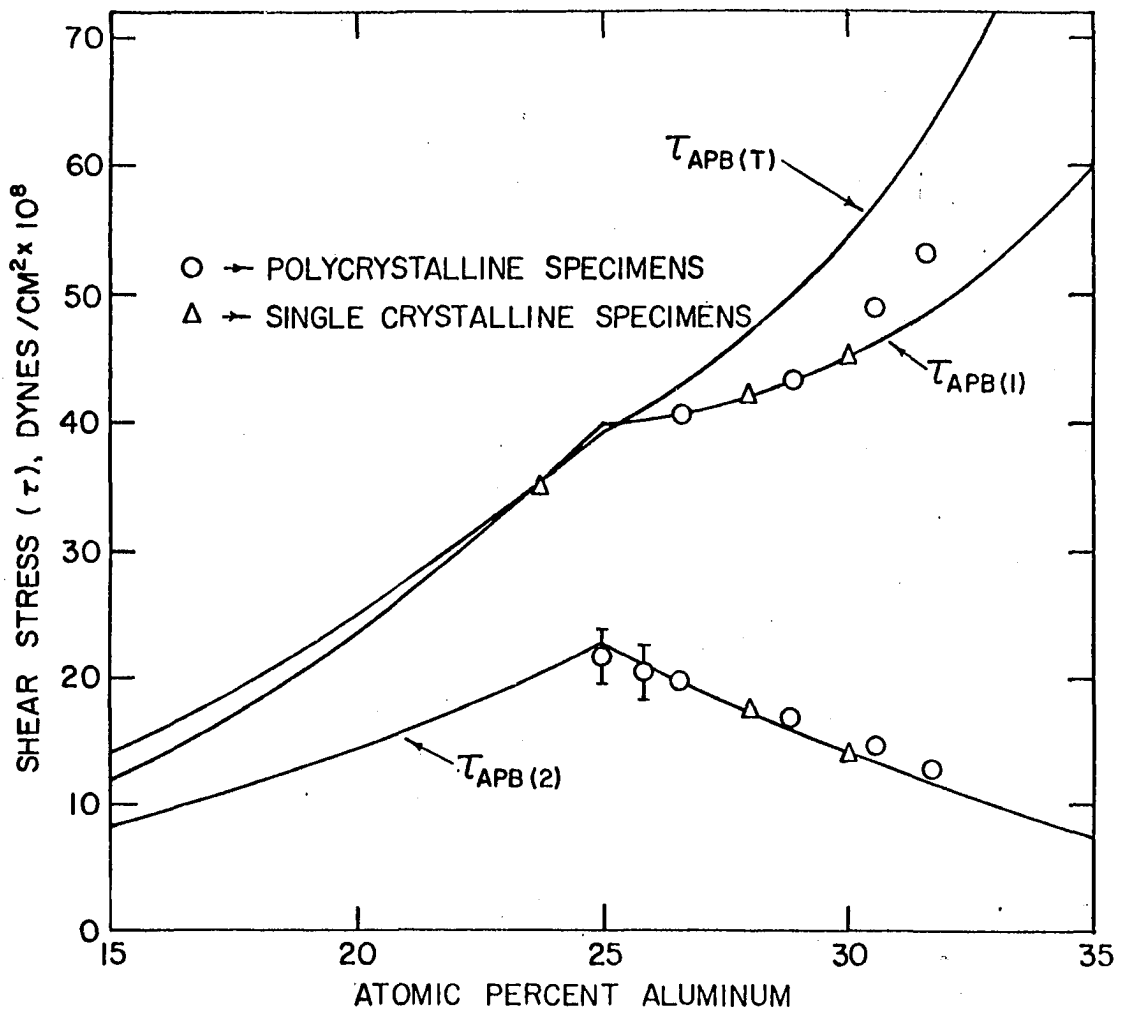

Figure 13. Calculated and experimental values of the shear stress required for APB production

Taylor and Jones (3), while E_{NNN} values were calculated from Morse, atom pair potential functions obtained in a previous study of the elastic constants of these alloys (64). E_{NN} values, however, were obtained by subtracting 7×10^{-14} erg from values as calculated from the Morse potentials. This adjustment of the Morse parameter E_{NN} values was performed in order to obtain reasonable agreement between the calculated $\tau_{APB}(1)$ values and those obtained from the curves of Figure 9, and presumably was required because of the arbitrariness of the Morse function.

Because the two linear stage behavior shown in Figure 9 may be attributed to the production of DO_3 type superlattice dislocations at the yield stress, the absence of this behavior in the lower aluminum content alloys leads to the conclusion that nucleation of these superlattice dislocations is difficult at room temperature. Inspection of Figure 5 however, shows that these alloys exhibit a composition dependent decrease in yield strength with increasing temperature which likewise may be attributed to the production of DO_3 superlattice dislocations. In addition, the partial destruction of DO_3 type LRO by quenching serves to eliminate the first linear stage. Thus, the nucleation of DO_3 type superlattice dislocations in quantities sufficient for significant plastic flow,

is sensitively dependent upon temperature, alloy composition, and APB energy. Although this behavior has been discussed by Marcinkowski and Leamy (65) and will be examined in greater detail in a subsequent section, the flow stress curves of the quenched alloys may be analysed simply on the basis that heat treatments (b) and (c) produced DO_3 type LRO of insufficient strength for nucleation of superlattice dislocations.

Although several authors have reported that water quenching treatments eliminate macroscopic evidence for DO_3 type LRO in Fe-Al alloys, Lütjering and Warlimont (14) have shown that water quenching of 0.6 mm thick alloy plates does not suppress the nucleation of DO_3 LRO. Thus, heat treatments (b) and (c) most probably did not destroy the DO_3 LRO in the compression specimens because of their low surface to volume ratio. Reference to the diagram of Figure 2 shows that, during slow cooling, APD's of B2 type form first and, at lower temperatures, APD's of DO_3 type LRO nucleate within them. In fact, Marcinkowski and Fisher (56) have shown that heat treatments similar to (c) produce very large B2 APD's within which much smaller DO_3 type APD's form. Heat treatment (b), on the other hand, is expected to result in the formation of B2 and DO_3 APD's of more nearly equal size.

The existence of these APD's can have a large effect upon

the yield stresses of ordered alloys, as was first pointed out by Cottrell (43). If, for heat treatment (c), the B2 APD size is assumed to be large enough to be neglected, only the interaction between dislocations and APB's of the type $\bar{p} = \frac{1}{2}a_o\langle 111\rangle$ need be considered. Figure 13(a) shows that passage of a DO_3 superlattice dislocation through a DO_3 type APB results in the formation of an APB ledge of width equal to the total Burger's vector of the dislocation. A quantitative estimate of the stress required for this process may be obtained by consideration of a DO_3 dislocation of unit length which travels one unit distance along a slip plane. If the APD size is given by d then the intersection incidence is given roughly by 1/d so that the total APB area produced is equal to b/d. Thus, in analogy with Equation 11, the stress required for production of this APB area is given by:

$$\tau_{APD(a)} = \frac{\gamma_2}{\bar{b}} \cdot \frac{\bar{b}/d_{DO_3}}{1} \cdot (1-f) = \frac{\gamma_2}{d_{DO_3}} (1-f) \qquad (13)$$

where f is the area fraction of the slip plane which is occupied by APB, and is an important correction factor for the case of small APD's. As a first approximation f is usually taken equal to the volume fraction of APB (33), $1-(1-\bar{p}/d)^3$, where $\bar{p}$, the finite width assigned to the APB is assumed equal

to its displacement vector length. Thus, τ_{APD} must be included in the τ_s term of Equation 12a and may represent a significant contribution to the yield strength of ordered alloys. Figure 14(b) shows that passage of dislocations of type 12(d) or 12(e) results in the production of type 2 APB's on the slip plane at all locations except those described by Equation 13 so that a negative contribution of $(\gamma_{APB(2)}/d_{DO_3})$ (1-f) must be included in the τ_s term of Equation 12b. In addition, the $\tau_{APB(2)}$ term of Equation 12b must be modified to account for the lack of complete DO_3 type LRO associated with the small APD size. This modification may be accomplished by adjustment of S_{NNN} and recalculation of γ_2 or it may be accomplished in a more approximate way by multiplying $\tau_{APB(2)}$ by the factor (1-f). Finally, Figure 14(c) shows that the presence of DO_3 APD's has no effect upon the motion of ordinary $\frac{1}{4}a_o\langle 111\rangle$ dislocations. Although quantitative analysis of the data of Figure 11 is complicated by the lack of domain size values and knowledge of the additional contributions to τ_s produced by quenching, the above considerations show that, if deformation at the yield is accomodated by motion of dislocations of type 12(d), the composition dependence of the yield and σ_y stresses of these alloys should be

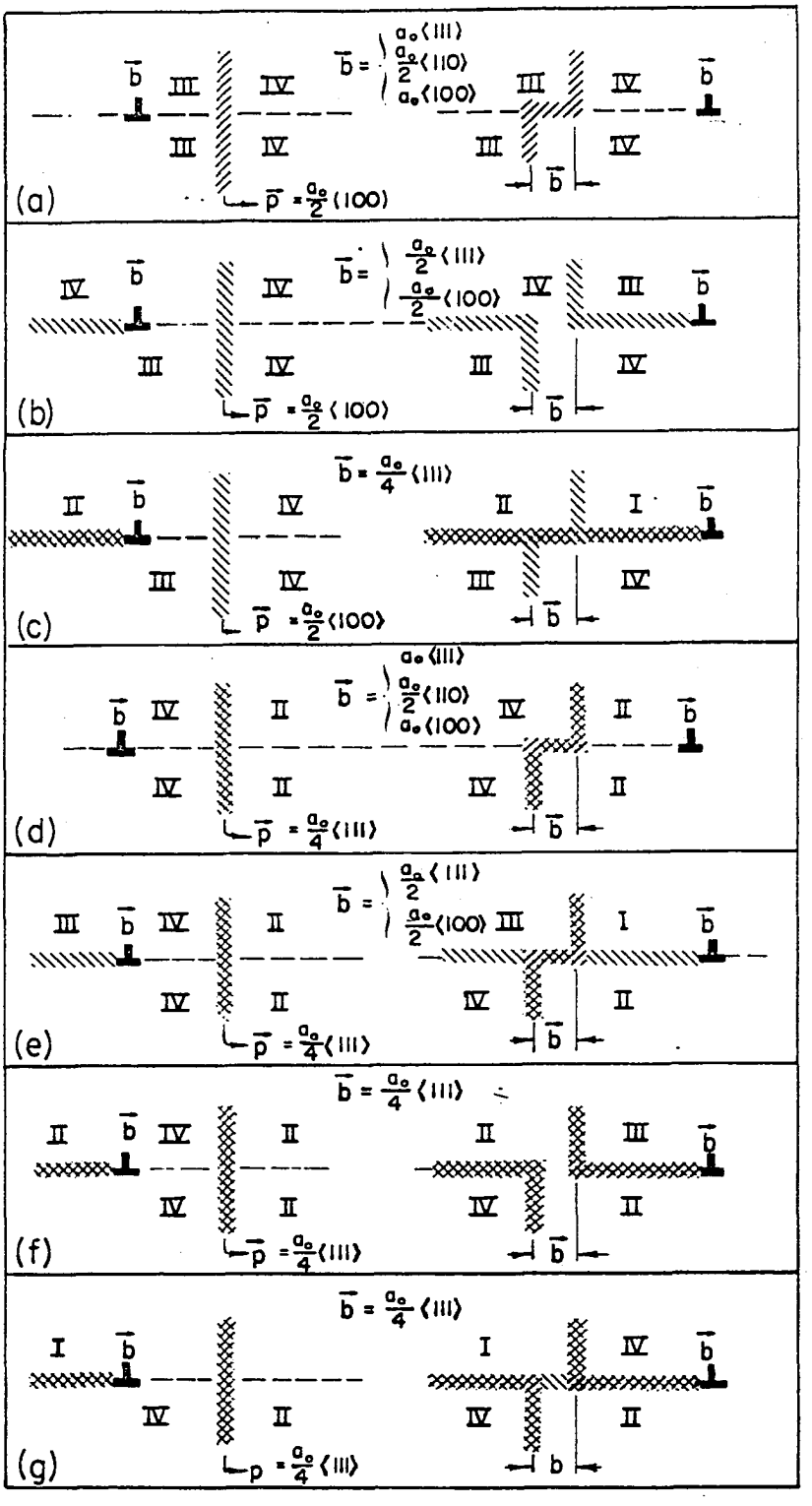

Figure 14. Schematic illustration of dislocation-APB interaction processes in DO_3 superlattice structures

similar to that of $\tau_{APB(2)}$ and $\tau_{APB(1)}$ respectively. That this is the case for the high Al content alloys may be seen by reference to Figure 15 where these values have been plotted as crosses.

If, as a first approximation, the APD size of both B2 and DO_3 type domains is assumed to be equal in alloys heat treated according to scheme (b), it may be shown that only one-third of all thermal APB's are of type $\vec{p} = \frac{1}{2}a_o\langle 100\rangle$ (56). Thus, the interaction of dislocations with $\vec{p} = \frac{1}{2}a_o\langle 111\rangle$ APB's must be considered. Figures 14(d) and 14(e) show that a contribution to τ_s,

$$\tau_{APD(1)} = \frac{\gamma_1}{d}(1-f) \qquad (14)$$

is produced by the existence of B2 type APD's for dislocations of type 12(a→c) as well as for those of type 12(d→e). Similarly, Figures 14(f) and 14(g) show that passage of ordinary dislocations through $\vec{p} = \frac{1}{2}a_o\langle 111\rangle$ boundaries results in the formation of an APB ledge of type APB(2) at half of the intersections. Thus the τ_s contribution for this case is given by

$$\tau_{APD(1)} = \frac{\gamma_2}{2d}(1-f). \qquad (15)$$

Therefore, the τ_s contribution due to the existence of B2 and DO_3 APD's of nearly equal size is given by:

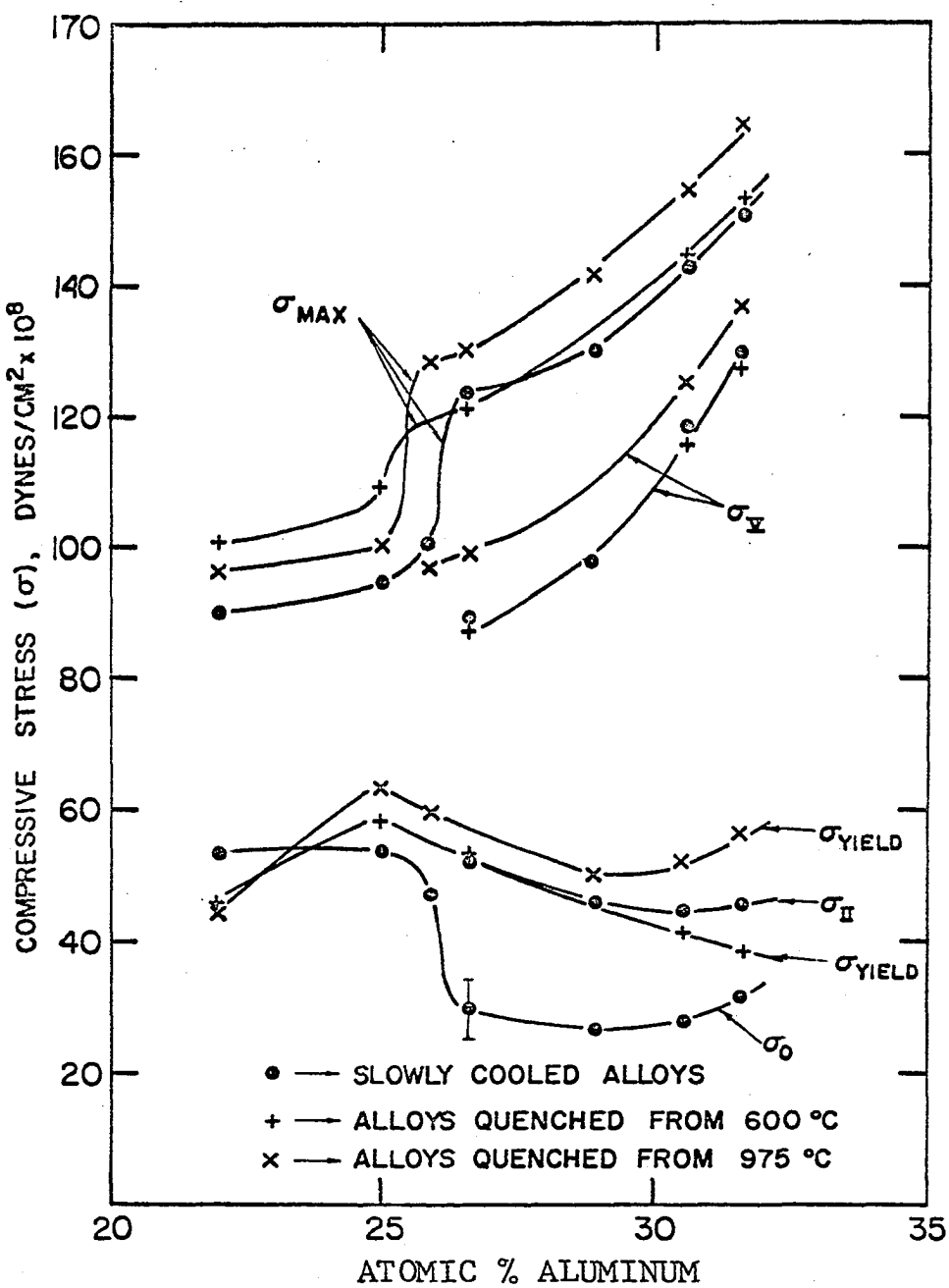

Figure 15. Stress levels for the polycrystalline Fe-Al flow stress curves shown in Figures 9, 10, and 11

$$\tau_{APD} = \frac{\gamma_2 + 2\gamma_1}{3d}(1-f) \tag{16a}$$

$$\tau_{APD} = \frac{2\gamma_1 - \gamma_2}{3d} \tag{16b}$$

$$\tau_{APD} = \frac{\gamma_2}{2d}(1-f) \tag{16c}$$

for the cases of dislocations of type 12(a→c), 12(d→e), and 12(f) respectively. Inspection of Equation 16b shows that the yield and σ_V stresses for alloys given heat treatment (b) should be larger than those for alloys heat treated according to scheme (c). Furthermore, since γ_1 increases while γ_2 decreases with increasing Al content, the difference between the yield stresses should increase while the difference between the σ_V values should decrease with increasing aluminum concentration. This behavior is also shown in Figure 15 where the quantities σ_o, σ_{II}, σ_V, and σ_{MAX}, the maximum flow stress, are plotted for the curves of Figures 9, 10, and 11.

Although explicit treatment of the slowly cooled, two phase alloy of 22 at.% Al has thus far been omitted, it may be shown that the experimental value is consistent with the production of APB's of type 1 within the ordered particles which intersect the slip plane. Since Lütjering and Warlimont (14,15) have shown that the area fraction of the slip plane

occupied by the ordered particles is nearly ½, the τ_{APB} term in Equation 12c may be computed on the basis of an effective γ value which is roughly half that for Fe_3Al. If τ_s is once again assumed small compared to $\tau_{APB(1)}$, the results of this calculation show that the yield stress is sufficient for production of these APB's. Both of the quenched 22 at.% Al specimens, on the other hand, deform by twinning at the yield stress. This behavior is expected on the basis of the theoretical analysis of Marcinkowski and Fisher (56). These authors have shown that because twinning dislocations produce APB's, the presence of LRO does inhibit twinning as first predicted by Laves (66). The stresses required for twinning in Fe_3Al (56) however, are lower for the case of B2 type LRO than for DO_3 type LRO if $E_{NNN} > E_{NN}/2$. Figure 16 shows that this conclusion is valid for a range of nonstoichiometric alloys as well. Although Equation 10 may be applied to the case of twinning, the τ_f, τ_g, τ_{APD}, and τ_s factors are difficult to evaluate. This fact not withstanding, the composition dependence of $\tau_{APB(T)}$ shown in Figure 16 does indicate that twinning should be difficult in alloys of high aluminum content. This expectation is experimentally verified as Figures 9, 10, and 11 show. These figures also show that for alloys which do

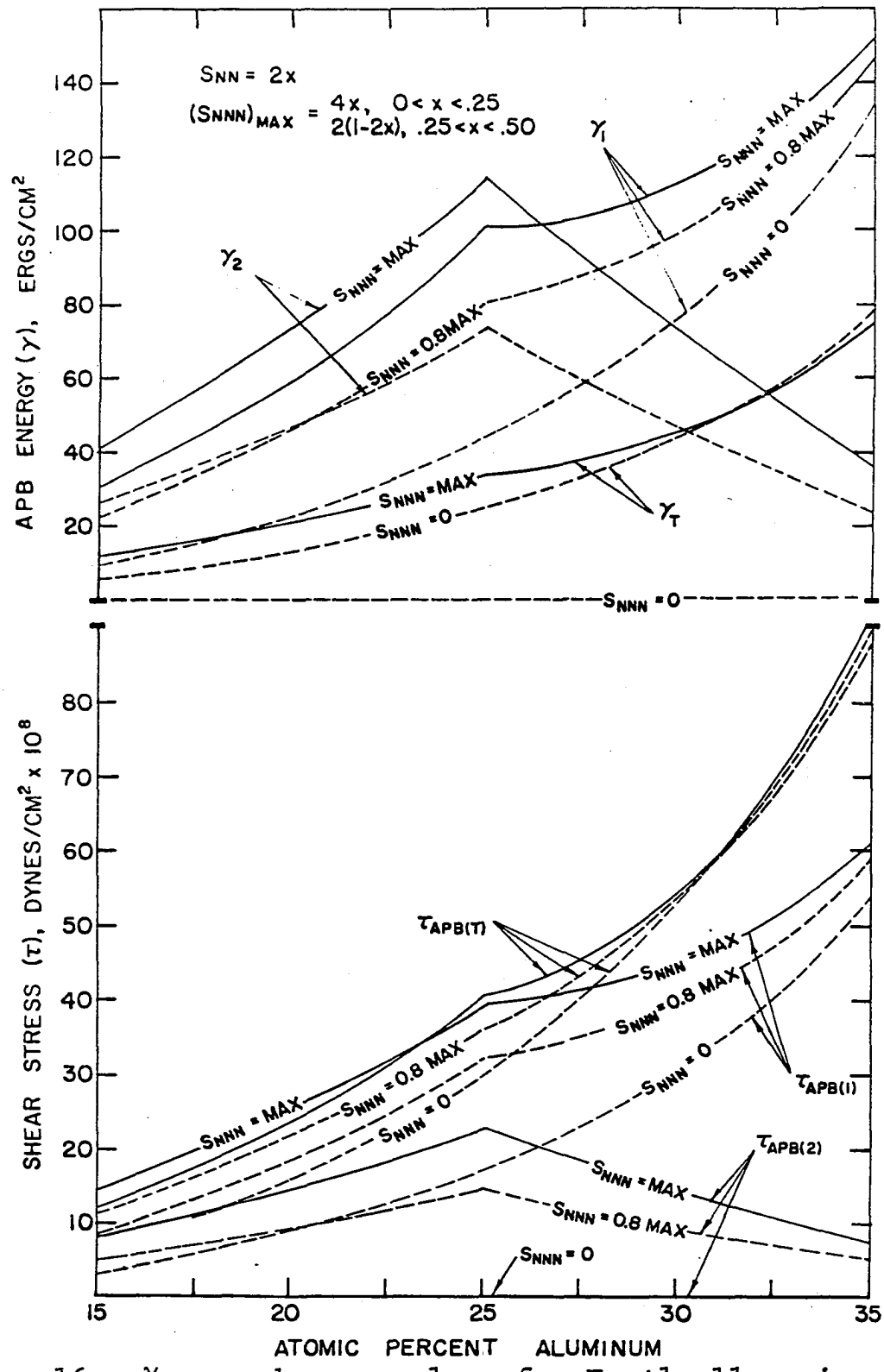

Figure 16. γ_{APB} and τ_{APB} values for Fe-Al alloys in various states of order

exhibit twinning, the flow stress at high strains is effectively determined by the low work hardening rate twinning deformation mode. As Figure 15 shows, the high aluminum content alloys work harden to a reasonably uniform extent in the parabolic stage so that σ_{MAX} assumes a concentration dependence similar to that of $\tau_{APB(1)}$. Alloys which twin, on the other hand, deform only slightly in the region of APB(1) production prior to twinning and thus exhibit much decreased values of σ_{MAX}. Although here again the lack of extensive experimental information obviates detailed analysis, the effect of APB's upon twinning may presumably be treated in a manner similar to that described previously for the case of slip dislocations.

As noted in the preceding remarks, twinning in the low aluminum content alloys occurs at relatively low strains. This behavior may be responsible for the low tensile ductility of these alloys since twinning is very often observed in the grains adjoining the fracture surface of alloys tested in tension. An example of this behavior in a 25 at.% Al tensile specimen is shown in Figure 17(a). Alloys which deform extensively in compression by APB(1) production, however, owe their low tensile ductility to the ease with which intragranular

Figure 17. Light micrographs of fractured Fe-Al alloy tensile specimens of (a): 25.0 at.% Al and (b): 30.6 at.% Al


(a)
0 05 CM

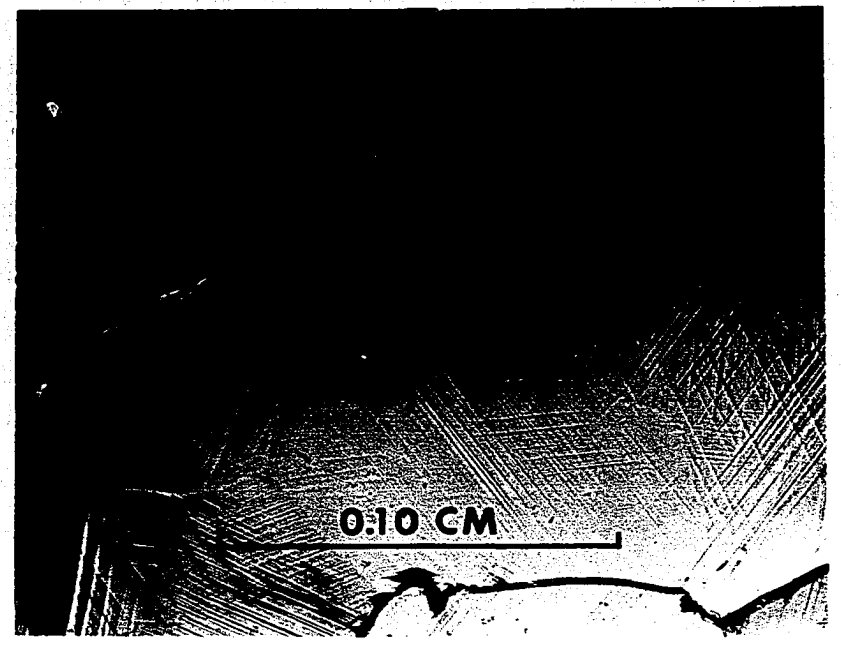
0.10 CM

crack propagation occurs. Examination of fractured tensile specimens of these alloys reveals extensive intragranular cracking as shown in Figure 17(b). In fact, Marcinkowski (67) has recently shown that the disorder associated with grain boundaries in alloys of high APB energy may provide a significant reduction in the energy required for crack formation as compared to formation within the well ordered grains.

In order to examine the temperature dependence of the stress levels which characterize the two linear stage behavior, a series of compressive flow stress curves were obtained at various temperatures from specimens of 26.6 at.% Al. These curves, and the temperature dependence of the stress levels, and work hardening rates are plotted in Figure 18. First, it should be noted that the two linear stage behavior, which is somewhat ill defined for the room temperature curve, becomes more well defined at higher temperatures but disappears at lower temperatures. Thus, below room temperature the nucleation of perfect DO_3 superlattice dislocations is difficult so that macroscopic deformation proceeds only at high stress levels by the motion of imperfect superlattice dislocations with consequent production of APB's. At high temperatures, however, DO_3 superlattice dislocation nucleation is possible and deformation proceeds via the three stage process described

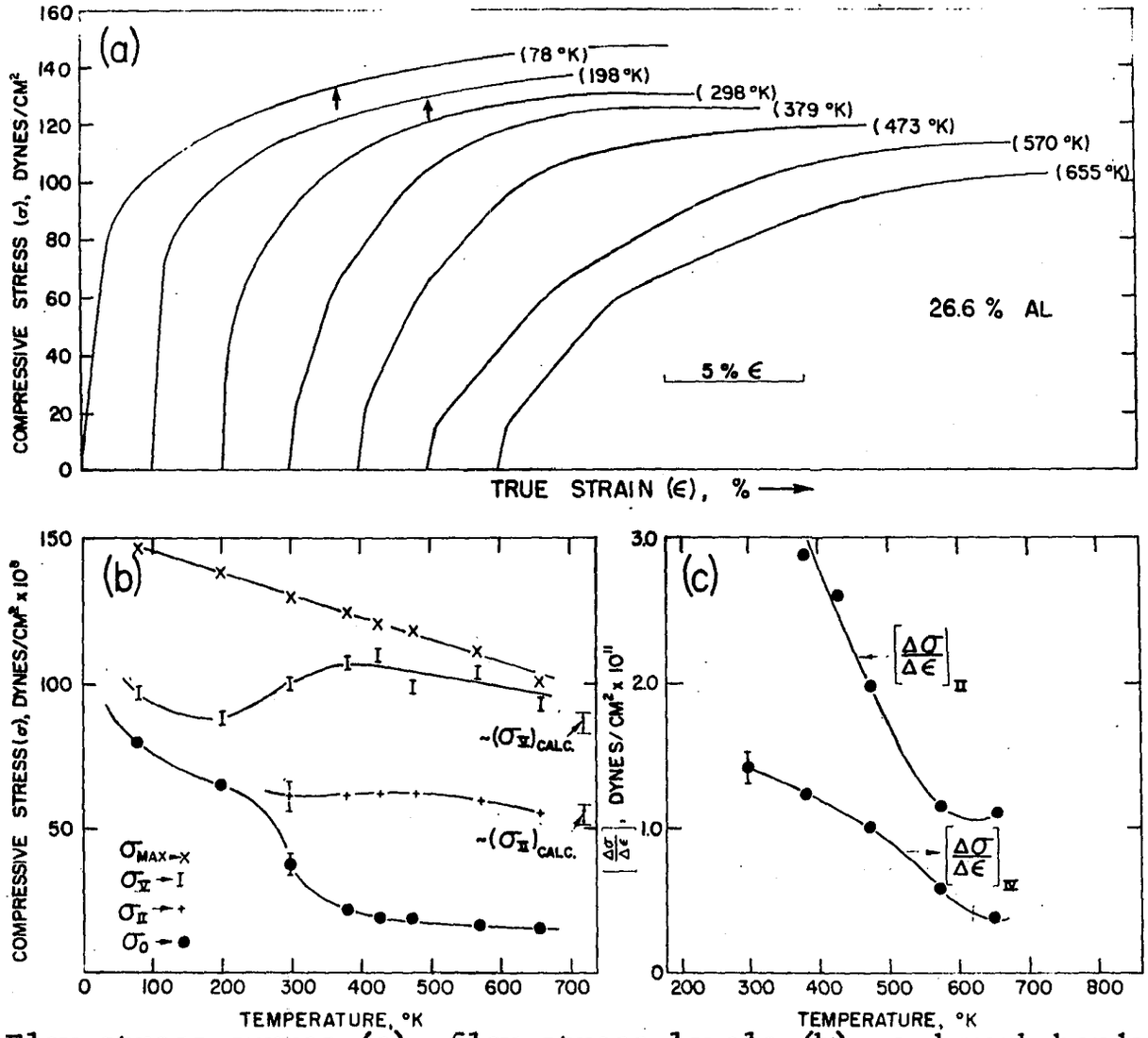

Figure 18. Flow stress curves (a), flow stress levels (b), and work hardening rates (c), for polycrystalline specimens of 26.6 at.% Al

previously. This change in deformation behavior is associated with the precipitous decrease in yield stress shown in Figure 18(b). The stress level plots of Figure 18(b) also show that the experimental σ_V and σ_{II} stress levels are in only approximate agreement with those calculated from Equation 12. This disagreement, however, is not unexpected because the temperature dependence of τ_s and τ_f were not included in the simplified τ_{II} and τ_V estimations given earlier. The 198°K flow stress curve, it may be noted, contains no well defined linear stage although the σ_o value for this curve is commensurate with production of type 2 APB's. This curve does, however, exhibit rapid nonlinear work hardening following the yield. Since a linear deformation stage is commonly attributed to the interaction of large numbers of dislocations which do not cross slip easily, i.e. extended dislocations, this behavior suggests that the quantity of type 12(d) dislocations nucleated at the yield stress is insufficient for the generation of a well defined linear stage. Furthermore, since σ_o is increased by the normal body centered cubic (b.c.c.) low temperature τ_f contribution, the external stress need be increased only slightly for production of type 1 APB's near regions of high stress concentration within the specimen. This same reasoning applies equally well to the 77°K curve

which exhibits a yield stress level very nearly sufficient for production of type 1 APB's. Similarly, for the room temperature curve, detectable plastic flow occurs at low stresses by the motion of type 12(a) dislocations which are nucleated in insufficient numbers for the production of a well defined linear stage. Finally, at higher temperatures, superlattice dislocations are produced and interact in large numbers so that all three stages are easily detected. These interactions result in the formation of a dislocation substructure which contributes to τ_s in Equations 12b and 12c so that σ_{II} and σ_V increase slightly with increasing temperature. At still higher temperatures the temperature dependent decrease in S_{NN} and the annihilation of substructure by climb effect a decrease in these quantities. In addition, σ_{MAX} shows a linear temperature dependence which presumably may also be attributed to thermally assisted annihilation or relaxation of obstacles to dislocation motion.

As might be expected, the strong temperature dependence of dislocation nucleation produces a marked temperature dependence in the work hardening behavior of this alloy. Although a value of $[\Delta\sigma/\Delta\epsilon]_{II}$, the work hardening rate of the first linear stage at 298°K, is not shown in Figure 19(c); an extremely high hardening rate, on the order of $4.0 \pm 0.2 \times 10^{11}$

Figure 19. Work hardening rates for polycrystalline alloys The data of Figures (a) and (b) is taken from reference (31)

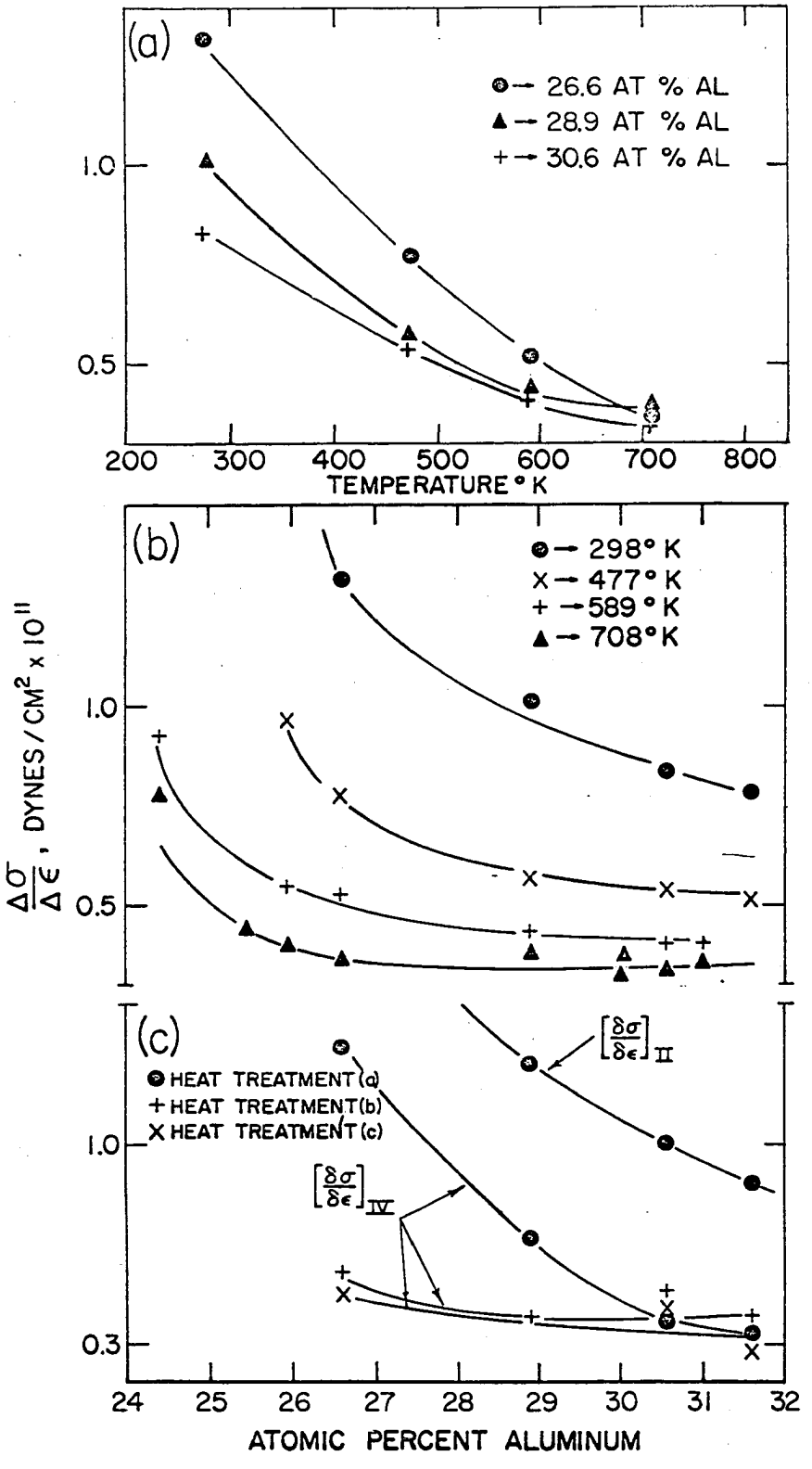
(a)
26.6 AT % AL
28.9 AT % AL
30.6 AT % AL
1.0
0.5
200
300
400
500
600
700
800
TEMPERATURE ° K
(b)
298° K
477° K
589 ° K
708° K
$\frac{\Delta\sigma}{\Delta\epsilon}$, DYNES / CM^2 x 10^{11}
1.0
0.5
(c)
HEAT TREATMENT (a)
HEAT TREATMENT (b)
HEAT TREATMENT (c)
$\left[\frac{\delta\sigma}{\delta\epsilon}\right]_{II}$
$\left[\frac{\delta\sigma}{\delta\epsilon}\right]_{IV}$
1.0
0.3
24
25
26
27
28
29
30
31
32
ATOMIC PERCENT ALUMINUM

dynes/cm^2, may be obtained from the poorly defined first linear stage of the 298^{o}K curve. Thus, at this temperature where nucleation is difficult, DO_3 type superlattice dislocations are not available in large numbers for accomodation of the externally applied strain so that a high work hardening rate results. As Figure 18(c) shows, the hardening rate of the first linear stage as well as that of the second linear stage, $[\Delta\sigma/\Delta\epsilon]_{IV}$ decrease in a nearly linear manner with increasing temperature in the approximate range from 288^o to 550^{o}K. At higher temperatures the rates of decrease are smaller so that both work hardening rates must approach zero quite rapidly at temperatures near $T_C(DO_3)$ where, as Figure 6 shows, no linear hardening is observed. That this behavior is general may be seen by inspection of Figure 19(a) where hardening rates have been plotted for the tensile curves of Figure 6. Figure 19(b) is a composition plot of the hardening rate data of reference (31) while Figure 19(c) is a similar plot of the work hardening rate values obtained in this investigation. Comparison of these figures shows that data obtained in compression and in tension are comparable even though no investigators detected the two linear stage behavior in tension experiments.

Although the temperature and composition dependence of these hardening rates will be discussed in greater detail in connection with a description of the single crystal experiments, it should be noted that the absence of linear work hardening behavior at temperatures near $T_c(DO_3)$ implies, according to earlier arguments, that paired superlattice dislocations are not responsible for deformation. In fact, Schmatz and Bush (35) have reported that at these temperatures, APB's of type 1 are produced by the motion of ordinary $\frac{1}{2}a_o$ <111> dislocations as was first suggested by Stoloff and Davies (27). In addition, these authors have attributed the yield effect in Fe-Al alloys to a strong stress dependence of the $\frac{1}{2}a_o$<111> dislocation velocity and production rate. The lower yield stress at these temperatures may, therefore, be attributed to the production of type 1 APB's as is described by Equation 12c. Because high temperature relaxation effects complicate this situation, a detailed analysis is unwarranted. The lower yield stress data of Kayser (29), however, does show quite reasonable agreement with $\tau_{APB(1)}$ as calculated from Equation 12c with $S_{NNN} = 0$ and $S_{NN} = 0.8(S_{NN})_{MAX}$. In this connection it should be noted that when APB production accompanies deformation, the propensity for intragranular

crack formation and the inability of dislocations to accommodate stress concentrations by cross slip are decreased. Therefore, a considerable increase in alloy ductility is expected and as Figure 4 shows, is experimentally realized.

Because several authors (68,69) have reported that the presence of LRO effects a pronounced change in the slip markings induced by deformation, the effect of deformation upon the surface appearance of several Fe-Al alloys was studied metallographically. Although the reliability of surface observations with respect to prediction of detailed internal deformation processes is in considerable doubt, the correlation of surface structure with observations made by the more powerful techniques of TEM has met with at least qualitative success. In fact, Marcinkowski and Chessin (62) have shown that the linear hardening behavior of ordered FeCo is accompanied by the formation of linear slip traces while the parabolic flow stress behavior of the disordered alloy is accompanied by the production of wavy slip traces. These same authors correlated this surface appearance with the presence of perfect and imperfect superlattice dislocations, respectively.

Figure 20 is a series of micrographs obtained from the

Figure 20. Light micrographs of slip lines produced by deformation of Fe_3Al to the following strains:

(a) 0.75% (b) 1.0%

(c) 1.25% (d) 1.50%

(e) 2.0% (f) 2.25%

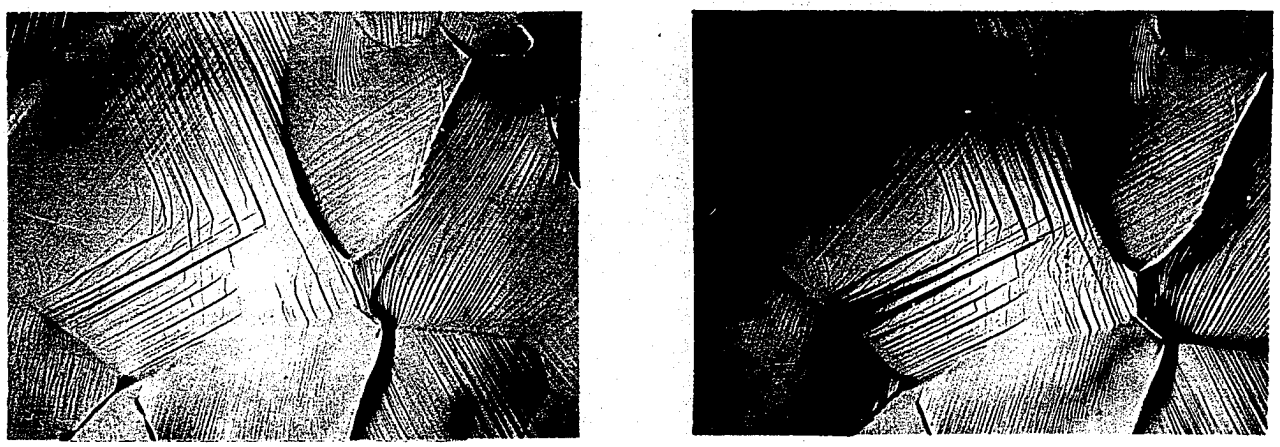

0.05 CM

0.05 CM

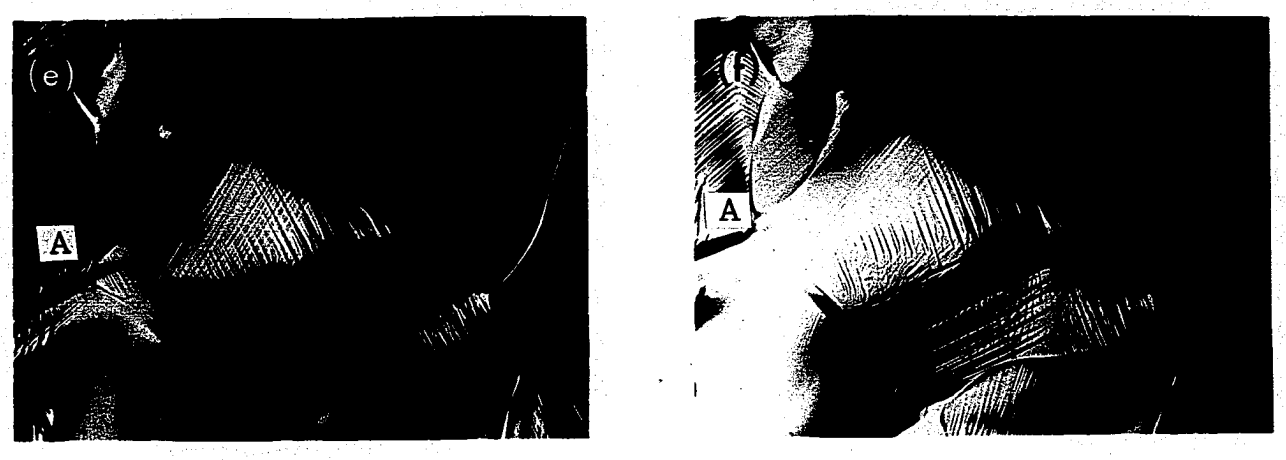

surface of a 25 at.% Al tensile specimen which was unloaded for examination at 0.25% strain intervals. Despite the unloading procedure, the course of deformation in this specimen, which was heat treated according to scheme (a), was quite similar to that shown in Figure 9. Figures 20(a) through 20(d) show that the early stages of deformation in this alloy are characterized by the formation of several sets of slip lines within each grain which persist over the strain interval of Figure 20. These lines increase in height only very slightly after formation even though distortion of the individual grains increases regularly with strain. Therefore, although the motion of many dislocations comprises the additional distortion, the fraction of these dislocations which escape from the specimen surface is decreased. At greater strain levels the appearance of new slip lines may be observed as shown in Figures 20(e) and 20(f) near "A". These new lines are best described as wavy and are much more intense, i.e. they are of greater height than those formed previously. The wavyness of this second type of slip structure may be taken as evidence that it is produced by the rampant cross slip of individual $\frac{1}{2}a_o\langle 111\rangle$ dislocations. Figure 21 is a series of micrographs obtained from a similar specimen which was deformed

Figure 21. Light micrographs of slip lines produced by deformation of Fe_3Al to the following strains:

(a) 1.0% (b) 2.0%

(c) 5.0% (d) 10.0%

(e) 15.0% (f) 20.0%

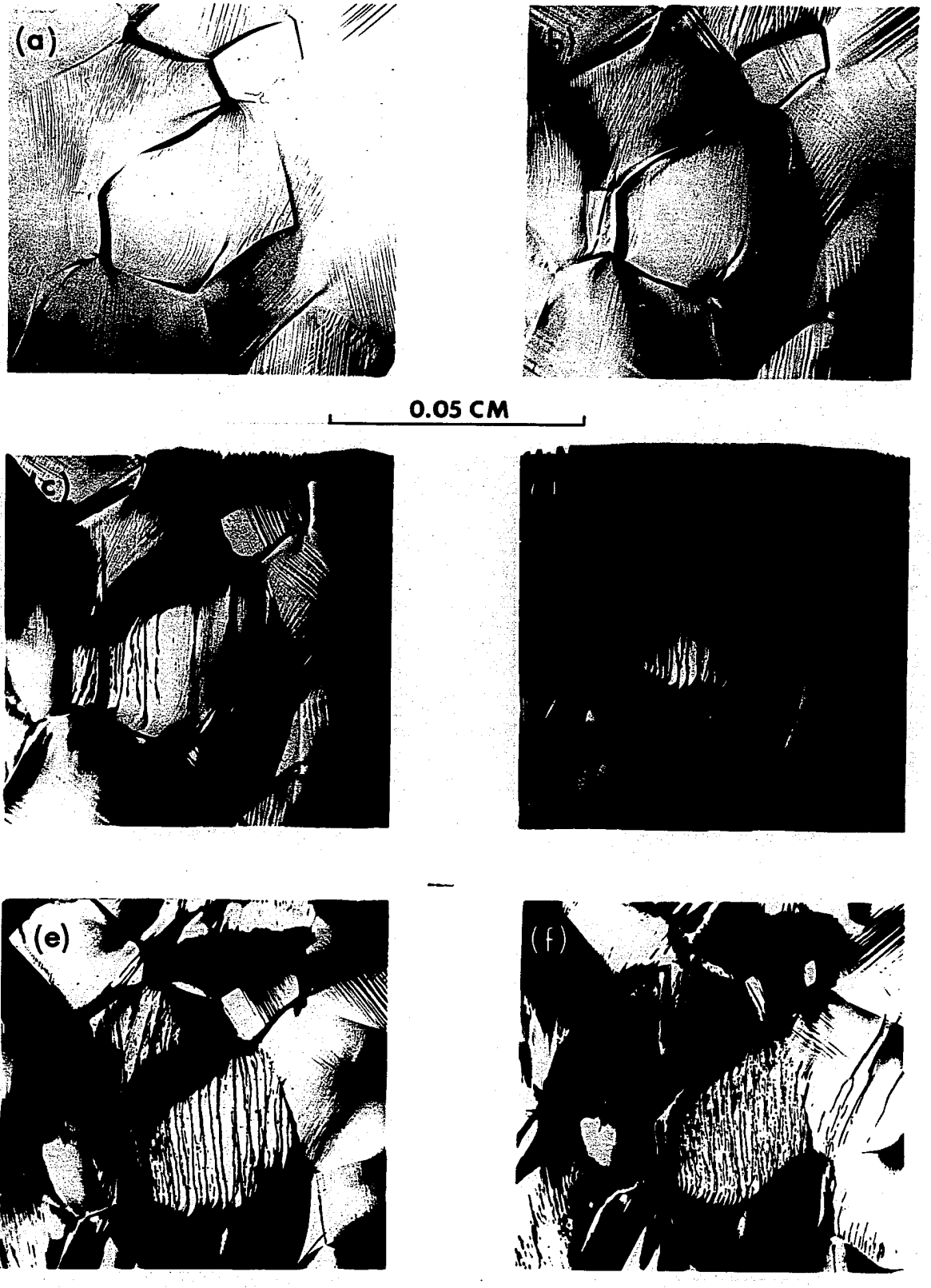
(a)
0.05 CM
(e)
(f)

in compression to higher strains. The micrographs of this figure show that in contrast to the slip structure formed at low strains, both the number and the height of the wavy slip lines increases as deformation proceeds. Thus, although some surface structure suggestive of cross slip appears in the micrographs of Figure 20, the low strain slip pattern may be attributed to the predominant motion and escape from the surface of dislocations of type 12(d).

The effect of deformation by motion of type 12(a) dislocations is most strikingly illustrated by the micrographs of Figure 22. These micrographs were obtained as described above from the surface of a 30.6 at.% Al compression specimen which was also heat treated according to scheme (a).

Figures 22(a) through 22(f) show that, similar to the case for Fe_3Al, the slip line pattern established at low strains persists until the onset of wavy slip. In this case, however, the slip lines are straight and well defined. In addition, these figures show that no gross changes in the slip line pattern accompany the transition from the first to the second linear stage. Figure 23 is a higher magnification micrograph which shows a typical complex polycrystalline slip pattern in more detail. The upper grain in this figure con-

Figure 22. Light micrographs of slip lines produced by compressive deformation of a 30.6 at.% Al alloy to the following strains:

(a) 2.0% (b) 5.0%

(c) 10.0% (d) 15.0%

(e) 20.0% (f) 30.0%

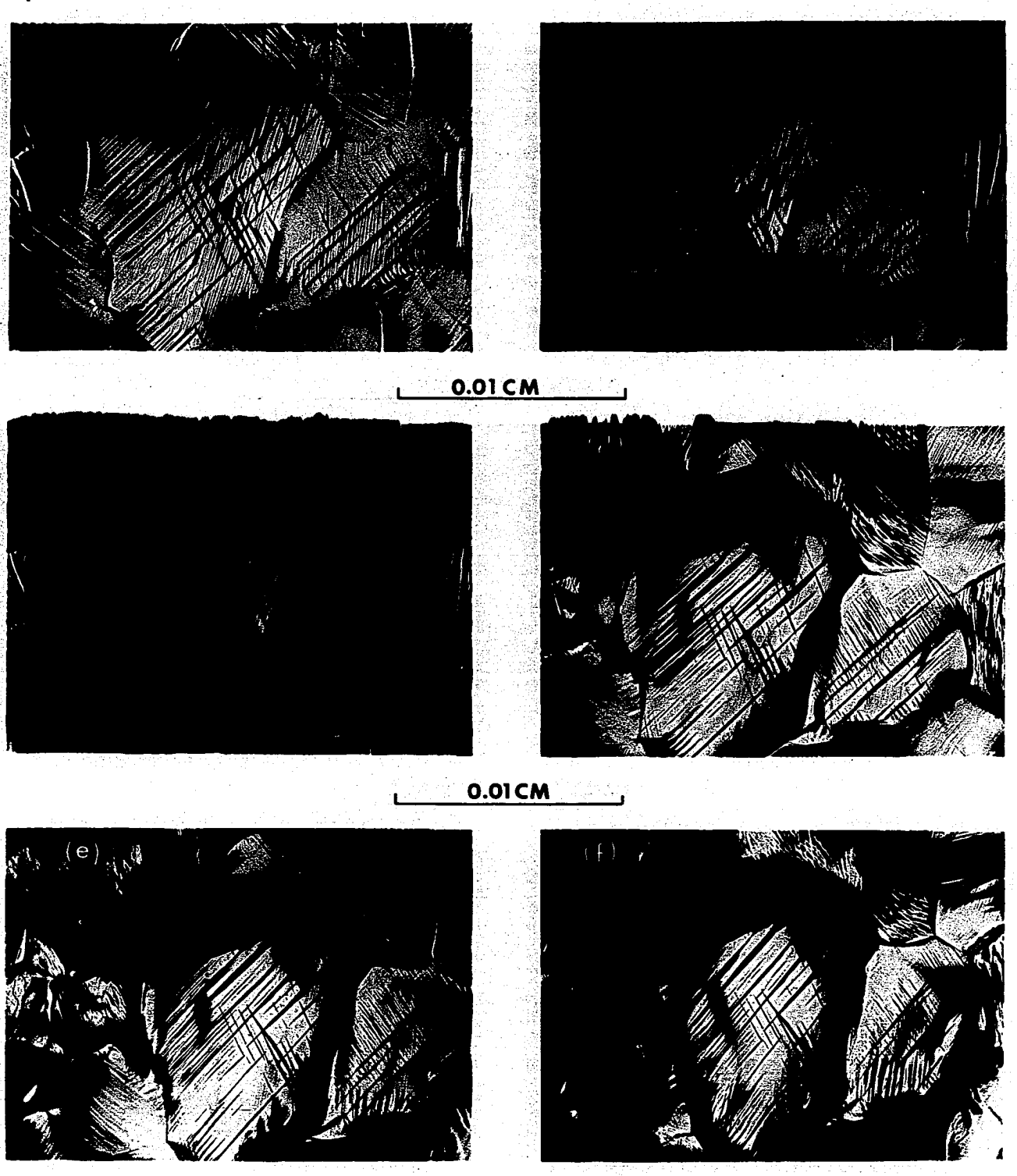
0.01 CM
0.01 CM
(e)
(f)

Figure 23. Typical complex polycrystalline slip line pattern produced by compressive deformation of a 30.6 at.% Al alloy specimen to 10.0% strain

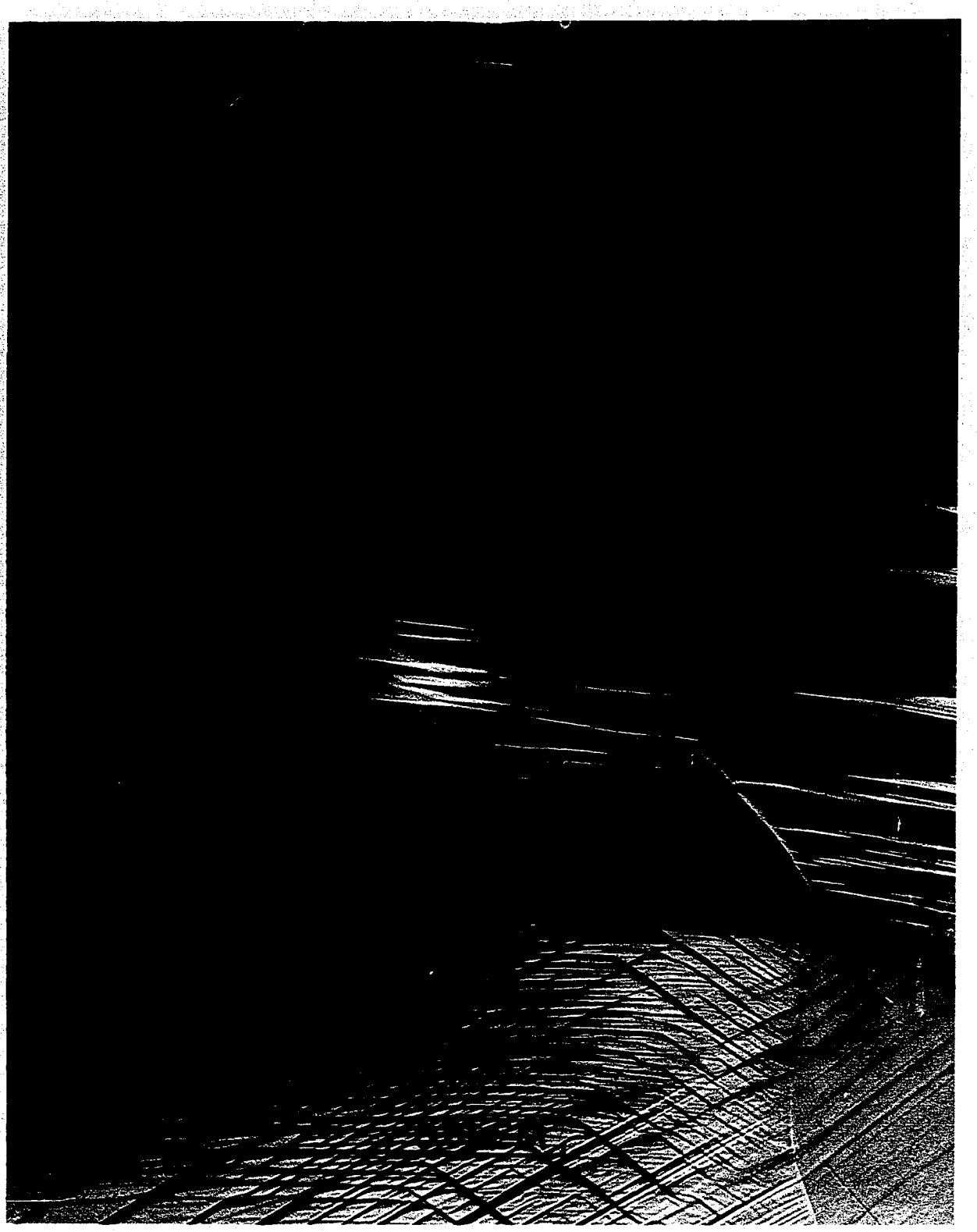

tains many wide slip bands within which individual striations may readily be observed. The wide slip band adjoining the grain boundary in the upper left of this figure shows that the high stress concentration at the boundary was accommodated by nucleation of a large number of dislocations, presumably at the boundary, while the bands in the center of the grain show that the shape change of the grain was accomplished by nucleation and motion of dislocation in highly localized regions. In many instances more widely spaced cross slip traces appear at the tips of these bands. These traces indicate that the stress concentration near the band tip is sufficient to produce cross-slip or alternatively, to activate potential dislocation sources on nearby slip planes. Therefore, since the deformation mode is determined by the magnitude of the shear stress on the particular slip plane, all three dislocation types mentioned previously may be mobile in polycrystals where regions of high stress concentration occur due to the complex stress system within individual grains.

Single Crystalline Specimen Deformation

Because many of the complications inherent in the treatment of polycrystalline specimen deformation may be eliminated by the study of single crystal deformation, a number of single

crystalline specimens were deformed at various temperatures during the course of this study. While crystals of several compression axis orientations were tested in this study, the majority were oriented for maximum shear stress on the $(\bar{1}01)$ plane as shown in Figure 24.

The results of a large number of experiments with crystals so oriented are presented schematically in Figure 25. This figure shows that the two linear stage hardening behavior observed in polycrystals is quite strikingly confirmed by single crystal experiments. In fact, the use of single crystalline specimens permits the observation of altogether five distinct deformation stages in alloys of high aluminum content. It should be noted that the first four of these are linear. The notation of Figure 25 is simply an extension of that commonly employed for description of f.c.c. flow stress curves. In this connection it may be noted that stages I and III are reminiscent of the so called easy glide stage of f.c.c. crystals. By analogy therefore, the curve of Figure 25 may be regarded as the result of the motion of three different dislocation types, i.e. stages I and II, III and IV, and stage V may be associated with motion of dislocation of type 12(a), 12(d) and 12(c) respectively. For these curves, the onset of

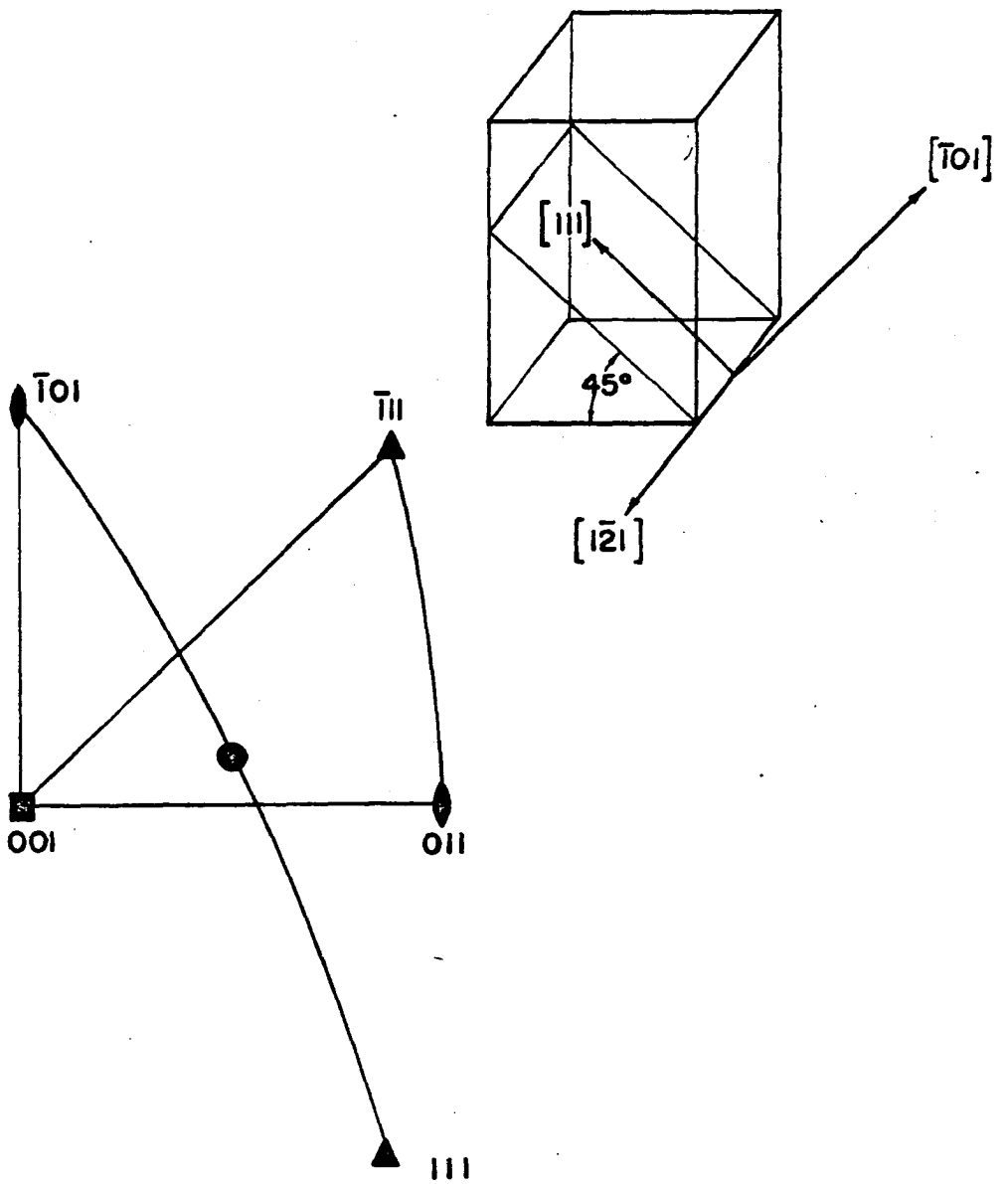

Figure 24. Stereographic and perspective illustrations of the single crystalline compression specimen geometry employed in this study

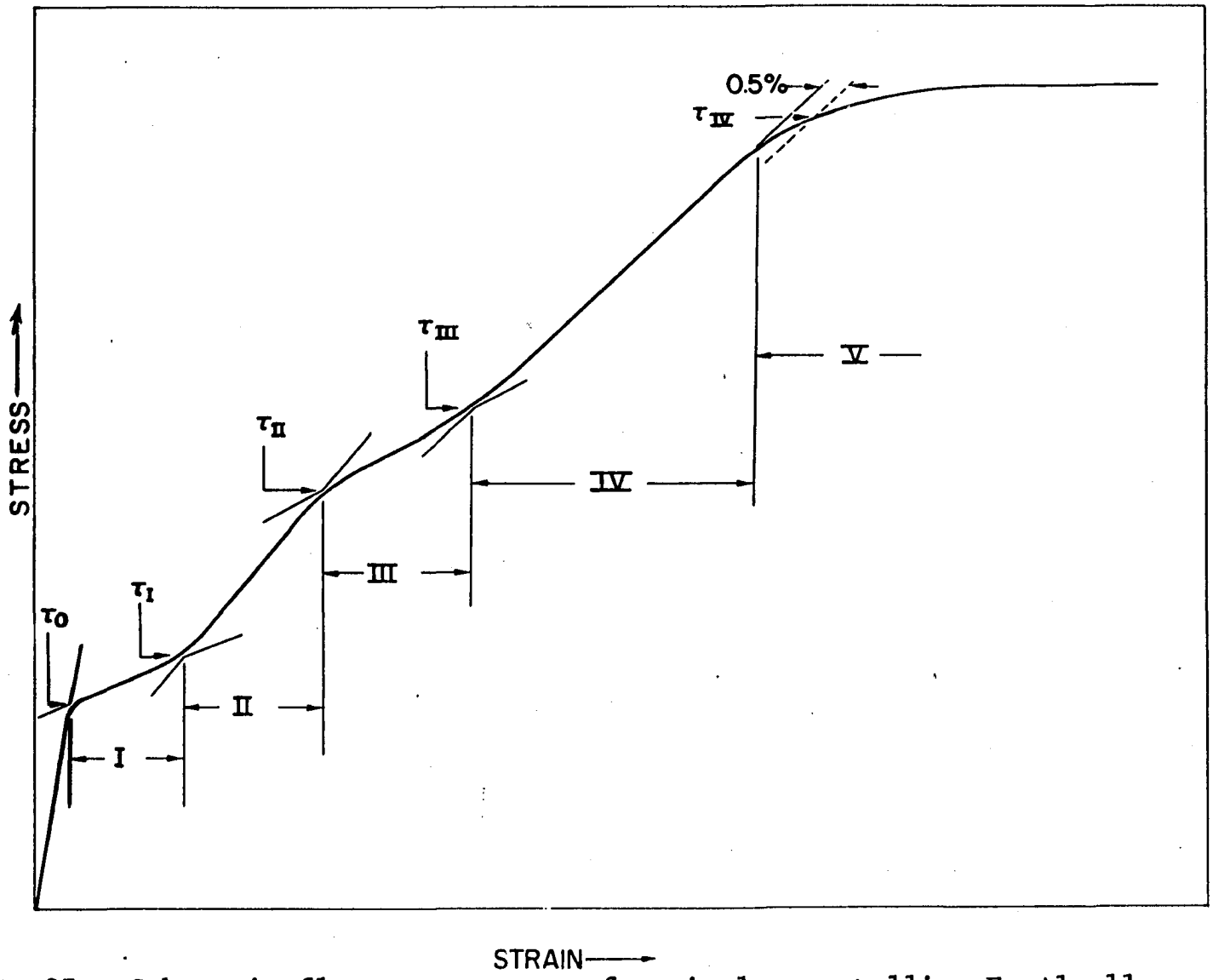

Figure 25. Schematic flow stress curve for single crystalline Fe-Al alloys

stage V was taken at an 0.5% offset from stage IV.

Application of the general arguments of Equations 12 to curves of this type yields the τ_{APB} values shown as triangles in Figure 13, which are in good agreement with the calculated values.

Figure 26 is a plot of the shear stress-strain data obtained from a series of experiments with 30 at.% Al crystals. The curve denoted by ($298^{o}K$, $1373^{o}K$,Q), which exhibits only deformation stages IV and V, was obtained at room temperature from a specimen which had been water quenched from $1100^{o}C$. Here, as in the case of polycrystals, the partial destruction of DO_3 type LRO serves to eliminate the deformation stages produced by motion of DO_3 type dislocations. These stages, however are conspicuously present in the curve obtained at $298^{o}K$ from a slowly cooled specimen. Comparison of these curves shows that the quenching treatment also effects an increase in the yield stress and a decrease in θ_{IV}, the work hardening rate of stage IV, in general agreement with the polycrystalline results described previously. The marked effect of temperature upon the deformation behavior of these alloys is also illustrated by these curves. For this composition the low temperature nucleation of DO_3 type dislocations

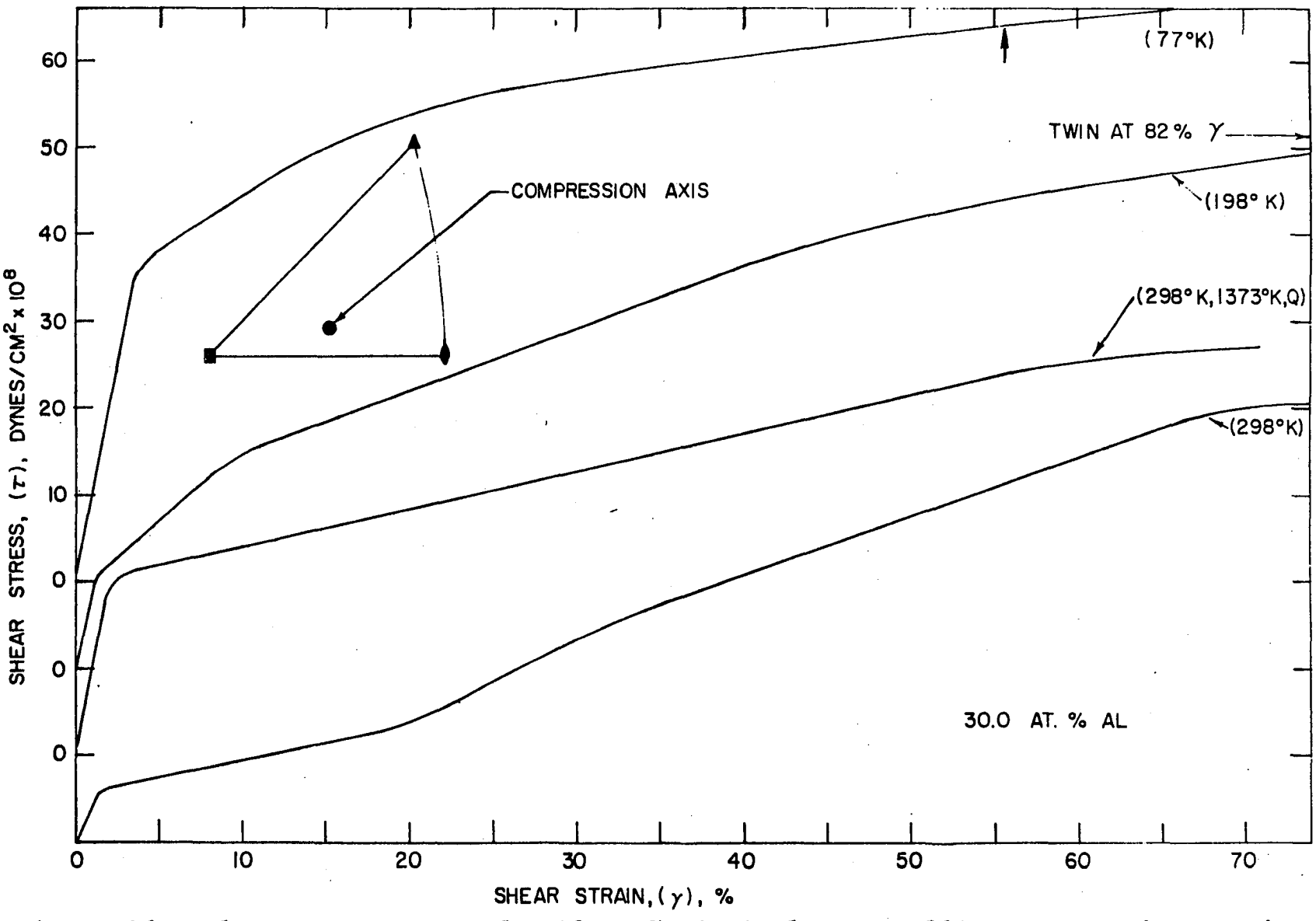

Figure 26. Flow stress curves for 30 at.% Al single crystalline compression specimens. Large arrows mark position of first twin burst

is difficult so that the 77°K curve exhibits only stages IV and V while the 198°K and 298°K curves show that DO_3 dislocation nucleation occurs at the yield. In addition, the 77°K and 198°K curves exhibit twinning at $\{112\}$ resolved stresses approximately 12×10^8 dynes/cm^2 above $\tau_{APB(T)}$ for this alloy. This behavior is not unexpected since, as Marcinkowski and Fisher (56) have pointed out, the critical resolved shear stress for twinning in b.c.c. structures is far less temperature dependent than is that for slip. Thus, since these alloys exhibit appreciable work hardening in stage V at low temperatures, the stress required for twinning is attained. Here again, the unknown effect of dislocation produced APB's and dislocation substructure complicate the quantitative analysis of this phenomenon. The curves of this figure also show that stages I and III are not always present and suggest that formation of stage I is favored by higher temperatures.

The results of a more extensive investigation of the effect of temperature upon the deformation of a 28.0 at.% Al alloy are summarized in Figures 27 and 28. The flow stress curves of Figure 27 show that for this alloy composition, deformation at 77°K is not accompanied by the formation of distinct linear hardening stages. At 142°K, however, three

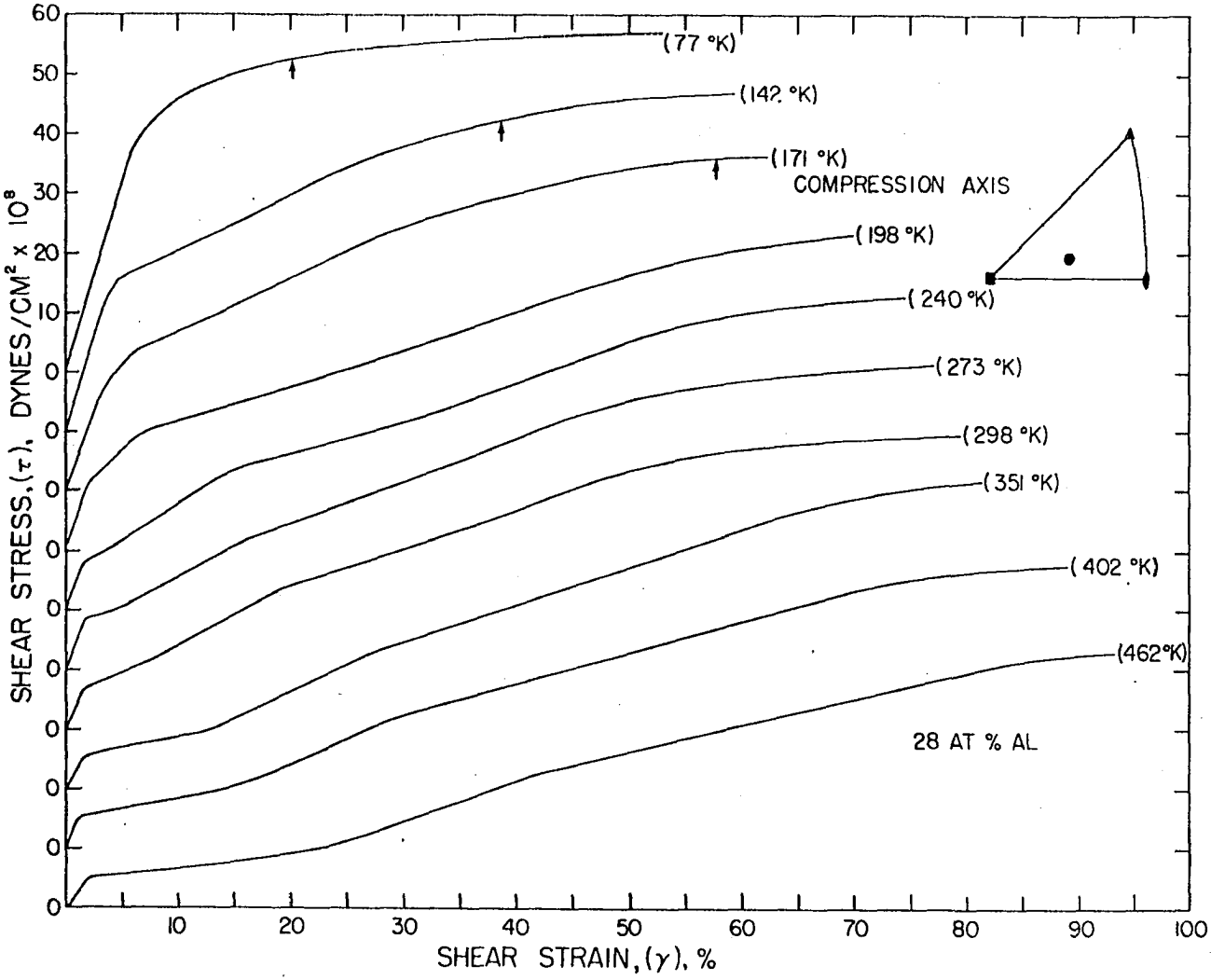

Figure 27. Flow stress curves obtained from single crystalline compression specimens of 28.0 at.% Al

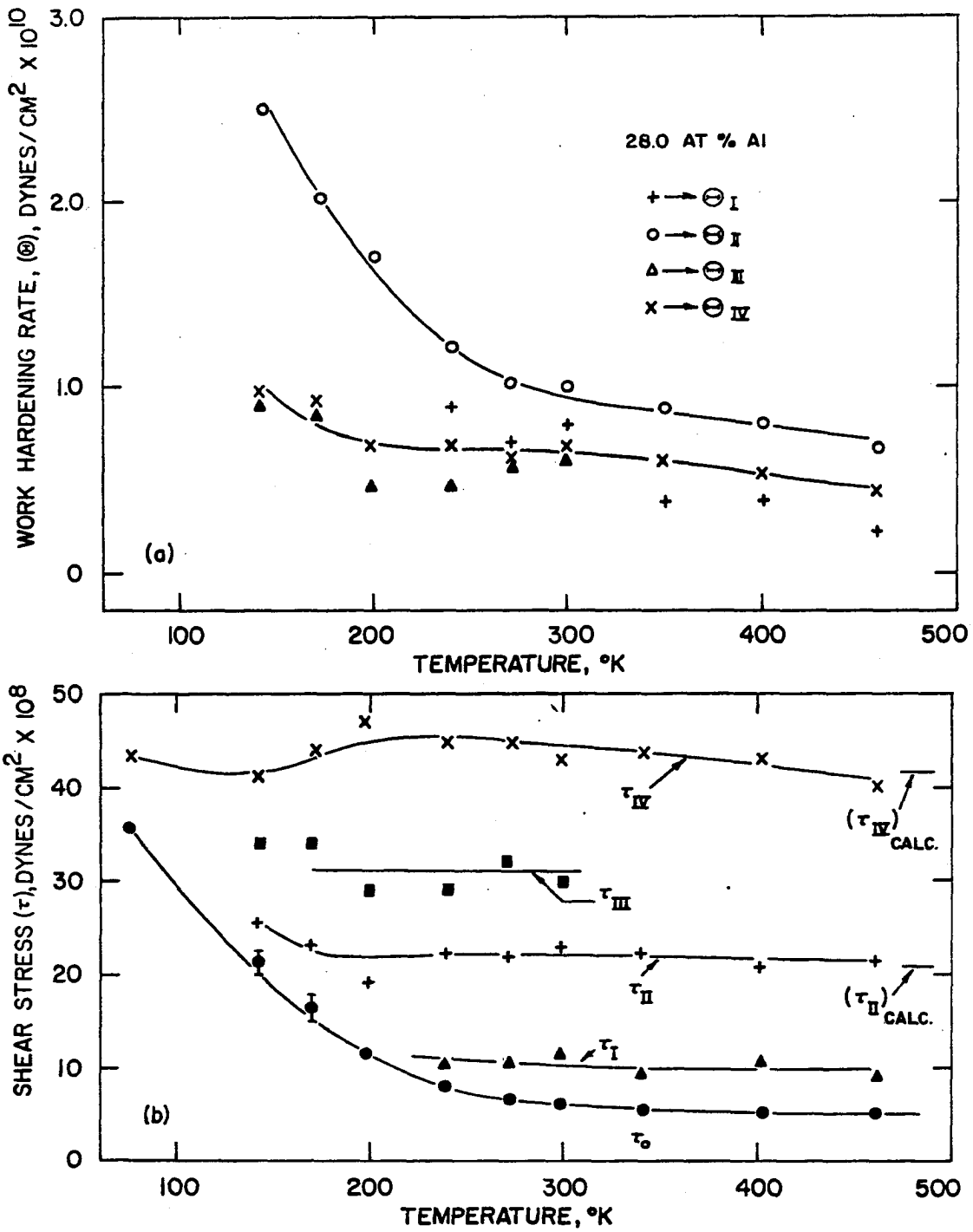

Figure 28. Work hardening rates (a), and flow stress levels (b) for the flow stress curves of Figure 27

linear stages including a short stage II of very high work hardening rate may be detected. Since the elastic regions of the flow stress curves were not determined with accuracy in these experiments they have been drawn at arbitrary slopes in all figures so that the shape of the yield points could be illustrated. On the Instron strip chart record however, the slope of the first linear stage of deformation produced at low temperatures is often very near that of the elastic portion of the curve. Therefore this first stage is detected only by very careful inspection. Figure 27 also shows that while the majority of the curves possess all four linear stages, the presence of stages I and III is favored by high and low test temperatures respectively. If these stages are regarded as evidence for the relatively unobstructed motion of DO_3 and B2 type dislocations, then the disappearance of stage III at higher temperatures is not surprising because stage II terminates at rather high strains so that such unobstructed motion is not possible. The presence of stage I, on the other hand, may be taken as evidence that sufficient thermal energy is available for nucleation of DO_3 dislocations in large numbers. Thus, when the second stage is preceded by stage I its hardening rate may be attributed to the obstruction of dislocation

motion alone. At lower temperatures however, formation of stage I is not observed and the stage II hardening rate, θ_{II}, is increased as shown in Figure 28(a). This behavior is also observed to a lesser extent for θ_{IV} while values of θ_I and θ_{III} show no distinct temperature dependence. Although no clearly defined drop in yield stress with increasing temperature occurs for the 28.0 at.% Al alloy, the curves of Figure 28(b) are similar in many respects to those of Figure 18(b). This figure shows that τ_{II} and τ_{IV} are in reasonable agreement with calculated values and that only τ_{IV} exhibits a discernable temperature dependence. The twinning stresses for these specimens are not plotted in Figure 28(b), however, inspection of Figure 27 shows that twinning occurs only at low temperatures and at stresses sufficient for production of APB's of type APB(T).

Figure 5 indicates that the aluminum rich two phase alloys also exhibit a yield stress decrease at high temperatures. This behavior is also observed in compression for single crystalline specimens of 23.8 at.% Al, as is shown in Figure 29. For this alloy composition twinning occurs at stresses only slightly greater than those required for production of APB's of type 1, in accord with the prediction of

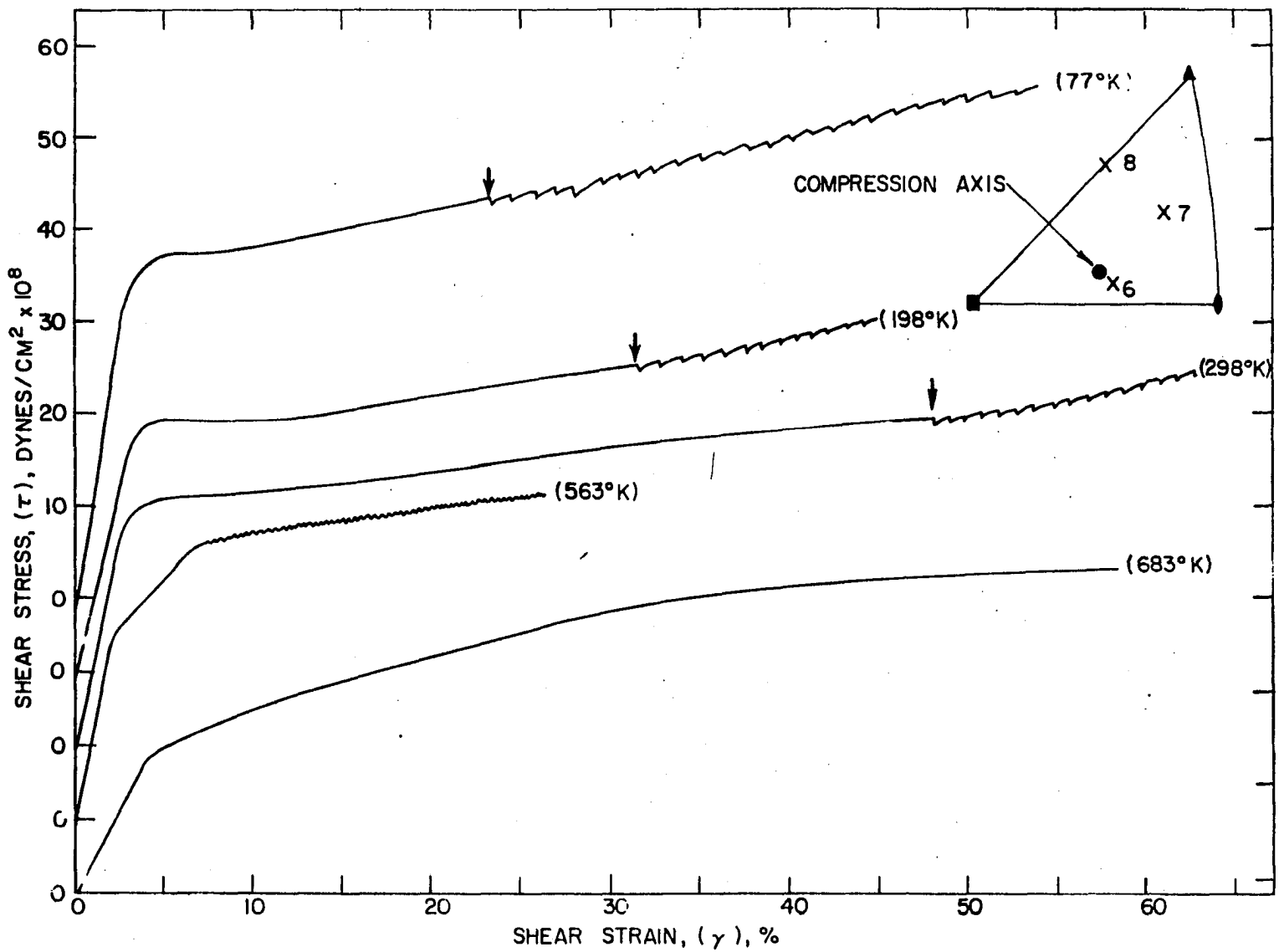

Figure 29. Compressive flow stress curves for 23.8 at.% Al single crystalline compression specimens. Arrows mark positions of first twin burst

Figure 13, and the load drops associated with each twin burst are larger than those which occur in alloys of higher aluminum content. At 563°K however, this alloy yields at a reduced stress level and work hardens in a single linear stage which, as will be shown later, is of type II. This stage is followed by a stage V in which the flow stress curve exhibits striations characteristic of dynamic strain aging. This particular flow stress curve is unusual in that it is the only case for which stage II is not followed by stage IV and where the dynamic strain aging effect occurs. Finally, at 683°K, the flow stress curve of this alloy exhibits stages II, IV, and V.

The results from 298°K tests of three additional specimens of this alloy, which were oriented as shown by the crosses in Figure 29, are not plotted in the figure because their flow stress curves are very nearly identical to that shown for the 298°K specimen. This result indicates that the orientation dependence of stage V deformation is quite small, at least for the orientations studied. Figure 8, which is a composite of photographs of specimen seven, shows that the wavy character of the slip lines produced in this deformation stage precludes the unambiguous determination of a single slip plane even though the macroscopic shape change is clearly consistent with

a single shear of the type $[111](\bar{3}21)$. Specimen six behaved in a similar manner with shape change of the type $[111](\bar{1}01)$ while specimen eight, which was oriented with its compression axis in the $[\bar{1}12]$ direction, underwent a shape change consistent with equal strain in each of two simple shear deformation modes: $[\bar{1}\bar{1}1](\bar{1}32)$ and $[111](\bar{3}12)$. Simultaneous operation of these two slip systems is in accord with the critical resolved shear stress criterion of Schmid (60) since each has a Schmid factor of 0.417. Thus, the hardening rate in this stage is little affected by the presence of double slip.

The linear hardening stages of deformation in these alloys however, are appreciably altered by the presence of double slip. Figure 30 shows the 198°K flow stress curves of two 28 at.% Al crystals; one oriented as shown in Figure 23 for single slip, the other oriented along <112> for symmetric double slip. It is apparent from this figure that both θ_{II} and θ_{IV} are increased by the action of two slip systems while that of stage V is scarcely altered. Although this behavior will be discussed in more detail in a subsequent section, it is apparent that the process of intersection of two superlattice dislocations of type 12(a) or $\bar{1}\bar{2}$(d) is difficult, a fact which is readily inferred from metallographic inspection

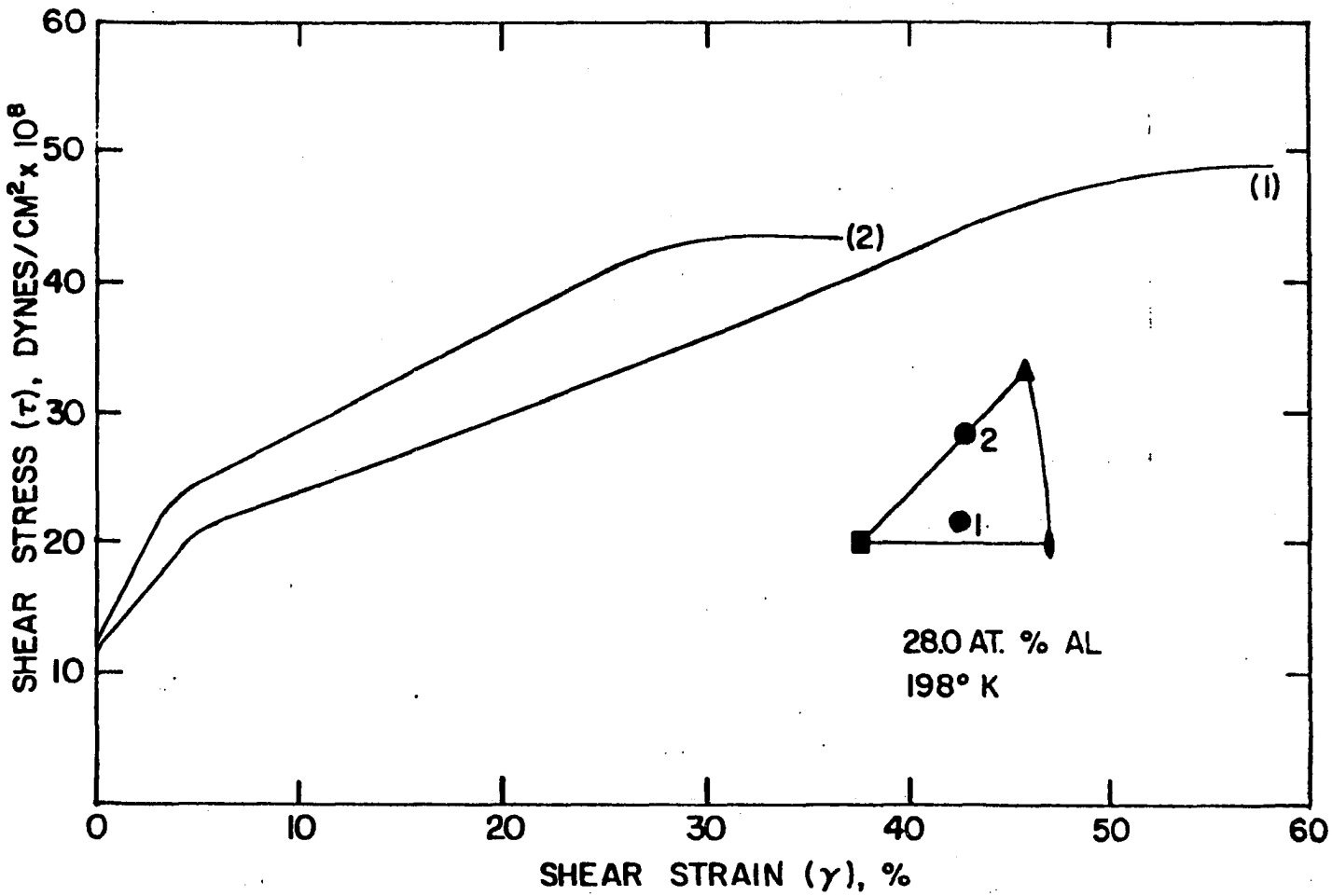

Figure 30. 198°K flow stress curves for 28.0 at.% Al specimens oriented as shown

of deformed specimens.

A selection of representative photomicrographs taken of deformed single crystalline specimens is presented in Figure 31. Micrograph 31(a) shows that deformation of single slip oriented crystals results in the formation of wide slip bands on the edge emergent crystal face, and that these bands are skewed with respect to the slip plane trace although the individual striations within the bands are parallel to this trace. Further deformation of such crystals results in the formation of additional bands and occasional cross slip traces as shown in micrograph 31(b) and 31(c) while deformation well into stage V produces the familiar wavy slip traces superimposed upon the previously formed slip bands as illustrated by micrograph 31(d). Single slip oriented crystals which deform via stage V at the yield, on the other hand, exhibit slip lines as shown in Figure 8 while similar crystals oriented for double slip exhibit the surface structure shown in Figure 31(c). Finally, crystals which deform via double slip during the linear stages of deformation appear as shown in Figure 31(f). This particular micrograph was obtained from the double slip oriented crystal of Figure 30 and shows that although this crystal was oriented for maximum resolved shear stress on $\{312\}$ planes, slip actually occurred on $\{110\}$ type

Figure 31. Optical micrographs of deformed single crystalline compression specimens

(a) 28.0 at.% Al specimen deformed ~10% γ at 298°K
(b) 28.0 at.% Al specimen deformed ~18% γ at 298°K
(c) 30.0 at.% Al specimen deformed ~16% γ at 198°K
(d) 28.0 at.% Al specimen deformed ~60% γ at 142°K
(e) 23.8 at.% Al specimen deformed ~26% γ at 298°K
(f) 28.0 at.% Al specimen deformed ~38% γ at 198°K


(a)

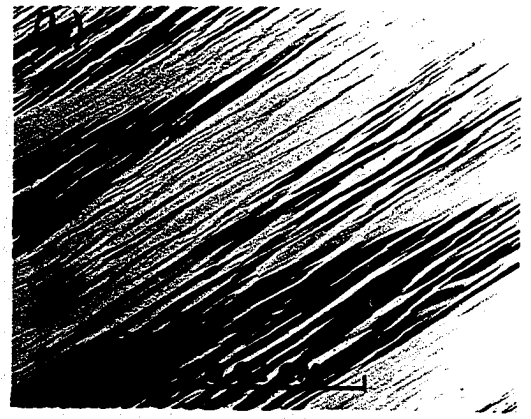

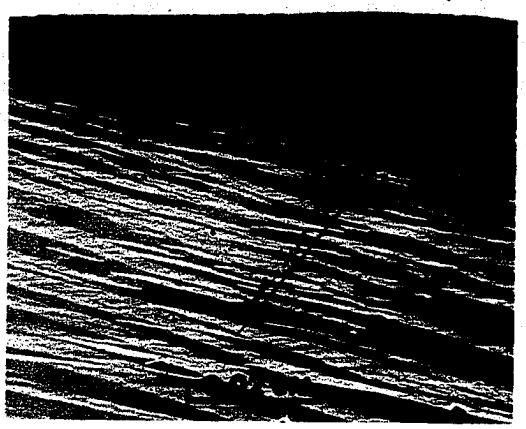

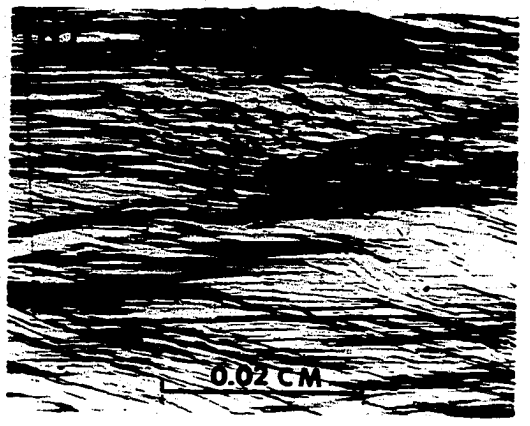
0.02 CM


(e)

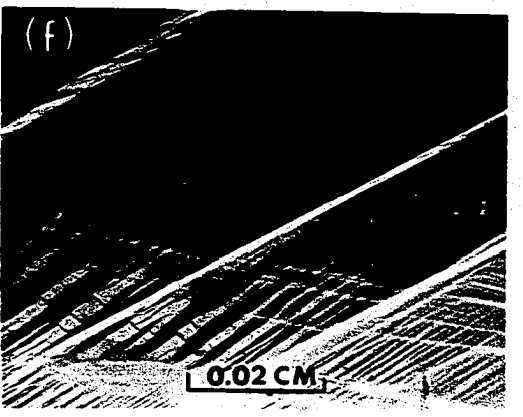
(f)
(ī01)
(011)
0.02 CM

planes. It is thus evident that motion of superlattice dislocations occurs predominantly on $\{110\}$ planes regardless of crystal orientation. This figure also shows that although slip traces of both systems are present, they very rarely intersect but rather form mutually contiguous bands of deformation. This observation leads to the conclusion that APB coupled superlattice dislocations are effectively immobilized by mutual intersection while ordinary dislocations are free to intersect and remain mobile as the slip pattern of Figure 31(c) suggests.

Although these experiments yield a reasonably complete macroscopic view of the deformation processes in iron rich iron-aluminum alloys, a more complete understanding of these processes may only be obtained by more direct methods of observation. For this reason a TEM investigation of deformed specimens was performed in conjunction with the experiments outlined above.

Transmission Electron Microscopical Observations

As Marcinkowski and Brown (38,39) have very dramatically demonstrated, the techniques of transmission electron microscopy are ideally suited for the investigation of defects in long range ordered Fe-Al alloys. Briefly, the structure

factor of such alloys may be written:

$$F_f = 16[(1-x)f_{Fe} + xf_{Al}] \quad \text{for } h+k+l = 2(2n), \tag{17a}$$

$$F_{S_{B2}} = 8S_{NN}(f_{Fe} - f_{Al}) \quad \text{for } h+k+l = 2(2n+1), \tag{17b}$$

$$F_{S_{DO_3}} = 4S_{NNN}(f_{Fe} - f_{Al}) \quad \text{for } h+k+l = 2n+1 \tag{17c}$$

where f_{Al} and f_{Fe} are the atomic scattering factors of Al and Fe respectively, n is an integer, and only unmixed indices are allowed. This formulation shows that the intensities of the superlattice reflections, S_{B2} and S_{DO_3}, depend not only upon the square of the difference between the atomic scattering factors but also upon the squares of S_{NN} and S_{NNN}, respectively. S_{DO_3} reflections, therefore, exist only when DO_3 type LRO is present in the specimen while reflections of the type S_{B2} exist whenever S_{NN} is finite.

In transmission electron microscopical images, contrast at deviations from lattice periodicity arises through a phase contrast mechanism (70). The phase angle, α, is given by:

$$\alpha = 2\pi \bar{g}\cdot\bar{R}, \tag{18}$$

where $\bar{g}$ is the reciprocal lattice vector associated with the particular diffracted beam and $\bar{R}$ is a vector which describes the deviation from periodicity. Deviations in atomic arrangement produced by defects such as dislocations effect a phase shift in all diffracted beams except when $\bar{g}\cdot\bar{R} = 0$. For APB's,

$\bar{R} = \bar{p}$ so that if $\bar{p}$ is exactly an interatomic vector then APB's of type 1 produce phase shifts of $\pm\pi$ and $\pm\pi/2$ in S_{B2} and S_{DO_3} reflections respectively while APB's of type 2 produce phase shifts of $\pm\ \pi$ in S_{DO_3} reflections. Since Marcinkowski and Brown have shown that $\bar{g}\cdot\bar{p} \neq 0$ for superlattice reflections in the DO_3 structure, dark field microscopy with these reflections provides an especially useful method for determination of APB types and configurations in iron-aluminum alloys.

The utility of this technique is illustrated by Figure 32 which is a 111 dark field micrograph obtained from an undeformed $(\bar{1}01)$ section of a 23.8 at.% Al compression specimen. This micrograph shows that the specimen consists of two phases, a light contrast DO_3 phase within which the S_{DO_3} reflection is excited and a dark contrast phase. Since S_{B2} type dark field images of this same specimen area are identical to that of Figure 32, the dark areas contain neither DO_3 nor B2 type LRO.

All alloy specimens of greater aluminum concentration which were examined in this study were observed to possess a homogeneous DO_3 structure similar to that shown in Figure 33. This micrograph was obtained from the slip plane of a 28.0 at.% Al compression specimen which had been deformed 0.8% in

Figure 32. The microstructure of a 23.8 at.% Al, two phase (DO_3 + α) alloy. This micrograph is a $\bar{1}\bar{1}\bar{1}$ dark field image of an undeformed ($\bar{1}01$) oriented foil

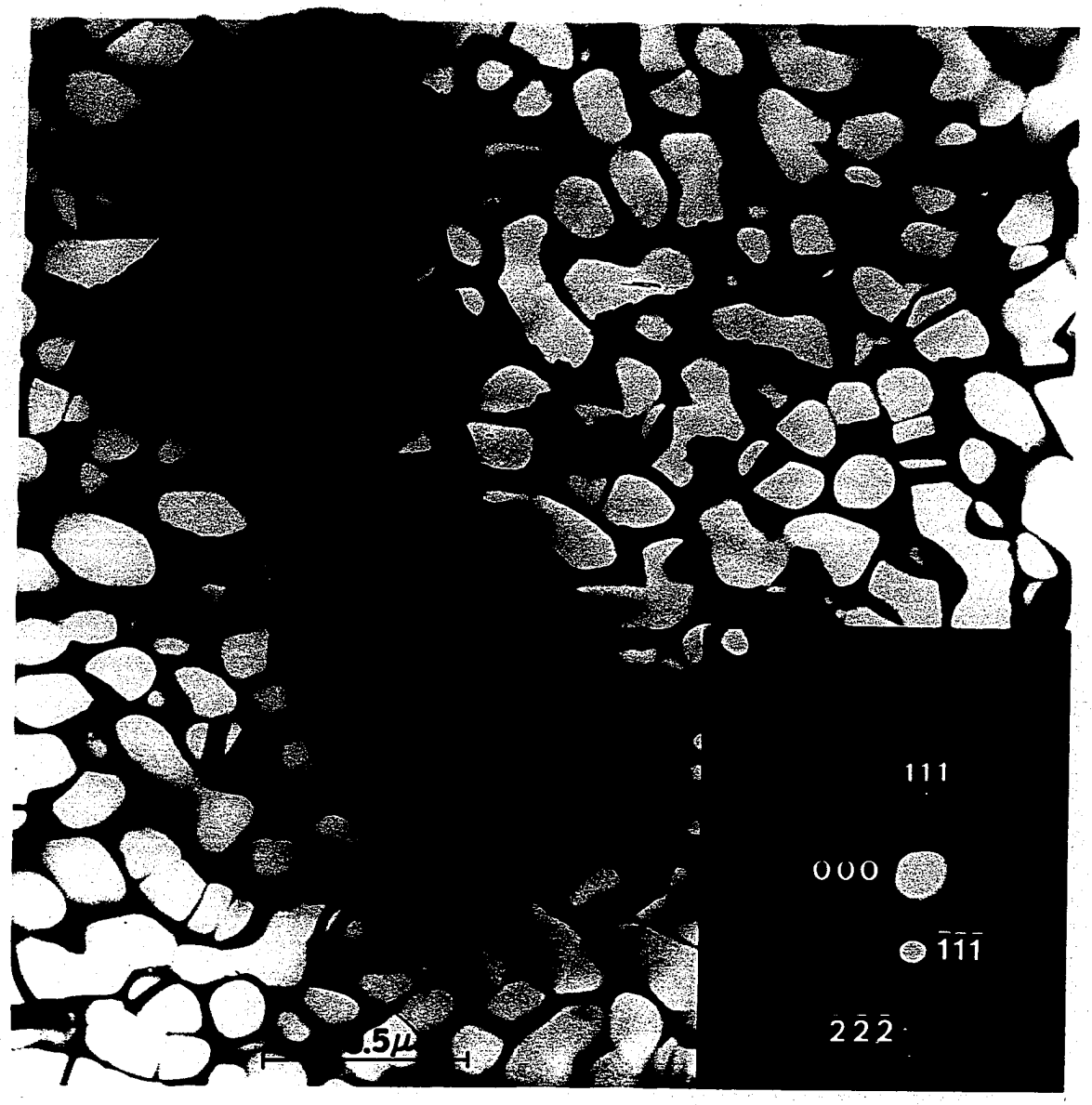
.5μ
111
000
$\bar{1}\bar{1}\bar{1}$
$2\bar{2}\bar{2}$

Figure 33. Light field micrograph of a $(\bar{1}01)$ section of a 28.0 at.% Al crystal. This crystal was strained 0.8% at 298°K prior to examination

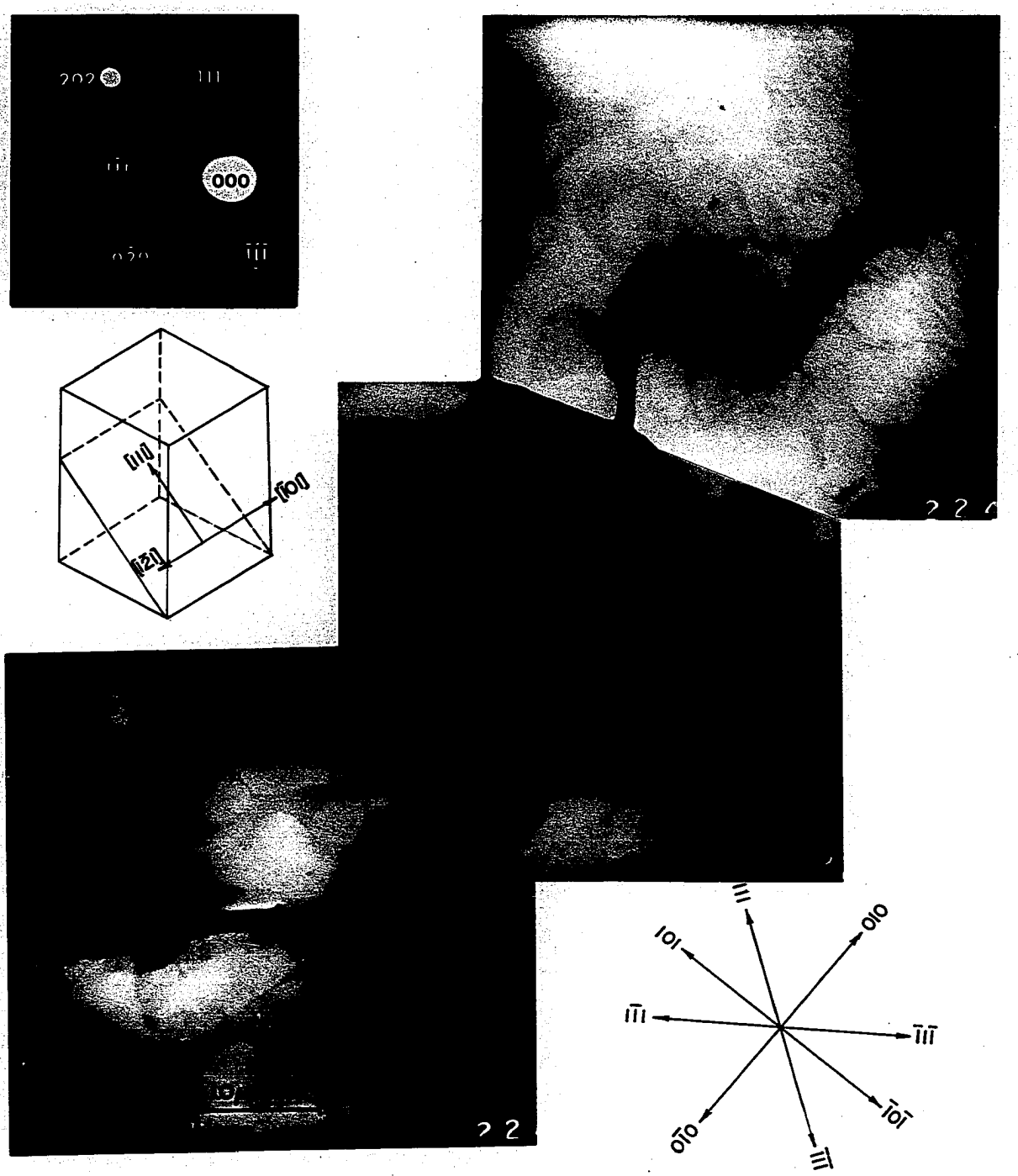
000
[010]
[101]
[12$\bar{1}$]
111
$\bar{1}$11
1$\bar{1}$1
$\bar{1}$$\bar{1}$1
101
010
$\bar{1}$01
0$\bar{1}$0
$\bar{1}$$\bar{1}$$\bar{1}$

stage I at 298°K. The homogeneity of the DO_3 structure in this specimen is evidenced by the presence of the thermally produced APD's of type 2, which are revealed in this light field micrograph through the phase angle shifts of the <111> reflections which contribute to the image. The absence of type 1 APD's in the micrograph is a result of the large B2 domain size produced by the very slow cooling rate heat treatment (38).

The rather striking dislocation configuration of Figure 33 is worthy of detailed analysis. The presence of the rather long dislocation segments in this $(\bar{1}01)$ foil indicates that $(\bar{1}01)$ is the slip plane, in accord with macroscopic slip line observations. Furthermore, it is evident that the Burger's vector of these dislocations is parallel to [111] because the dislocation segments parallel to this direction have, in several instances, cross slipped out of the foil. The absence of dislocation produced APB's on the cross slip planes indicates that these dislocations must be of type 12(a) or 12(b). Thus, since the remaining segments of dislocation appear as two dark lines, each line may represent either two dislocations of type $\frac{1}{4}a_o[111]$ or one dislocation of type $\frac{1}{2}a_o[111]$. A series of detailed image profile calculations for disloca-

tion configurations of both types, which is given in Appendix A of this thesis, shows that TEM contrast effects produced by both types are quite similar if the two $\frac{1}{2}a_o[111]$ dislocations are closely spaced. For this reason, consideration of the energetically favored dislocation types and their spacing is required for further analysis of this micrograph.

Because the Fe-Al alloys of interest exhibit marked elastic anisotropy it is necessary to account for this property through the use of the general anisotropic elasticity theory formulation (71) for the dislocation energies. The energy of an infinite, straight dislocation in an anisotropic media is given by:

$$E = \frac{Kb^2}{4\pi} \ln \frac{R}{\epsilon} \tag{19}$$

where K is the appropirate anisotropic energy factor and R and ϵ are the usual outer and inner cut off radii. For dislocations of type 12(a) and 12(b) the formulation of Equation 19 must be modified to include the interaction and APB energy terms thus:

$$E_{12(a)} = \frac{Kb^2}{2\pi}\left[2 \ln \frac{R}{\epsilon} + 2 \ln \frac{R}{r_1} + 2 \ln \frac{R}{r-r_1} + \ln \frac{R}{r_1} + \ln \frac{R}{r-2r_1} - 6\right] + 2\gamma_1 r_1 + (r-2r_1)\gamma_2 \tag{20a}$$

$$E_{12(b)} = \frac{Kb^2}{2\pi}\left[\ln\frac{R}{\epsilon} + \ln\frac{R}{r} - 1\right] + \gamma_2 r \qquad (20b)$$

where for Equation 20b, r is given simply by $Kb^2/2\pi\gamma_2$ while Equation 20a may be solved only by numerical or graphical techniques. In the general case K must be calculated numerically. However, simple analytical forms have been given for pure edge and pure screw dislocations (72,73) of several common slip system-Burger's vector combinations. Calculation of dislocation energies, mobilities (70) and widths (70) based on these formulations for the perfect dislocation types of Figure 12 at 2.5 at.% Al composition intervals produces numerical results far to extensive for tabular presentation. For this reason description of the calculations is included as Appendix B of this work. Reference to this Appendix shows that both edge and screw dislocations of type 12(a) are of lower energy than those of type 12(b). Furthermore, if any strain field associated with the type 1 APB's is assumed to contribute negligibly to the Peierls stress of type 12(a) dislocations, then they possess the more favorable mobilities. The equilibrium spacings of type 12(a) dislocations as calculated by the methods of Appendix B are displayed in Figure 34. Inspection of this figure shows that r_1 is rather insensitive

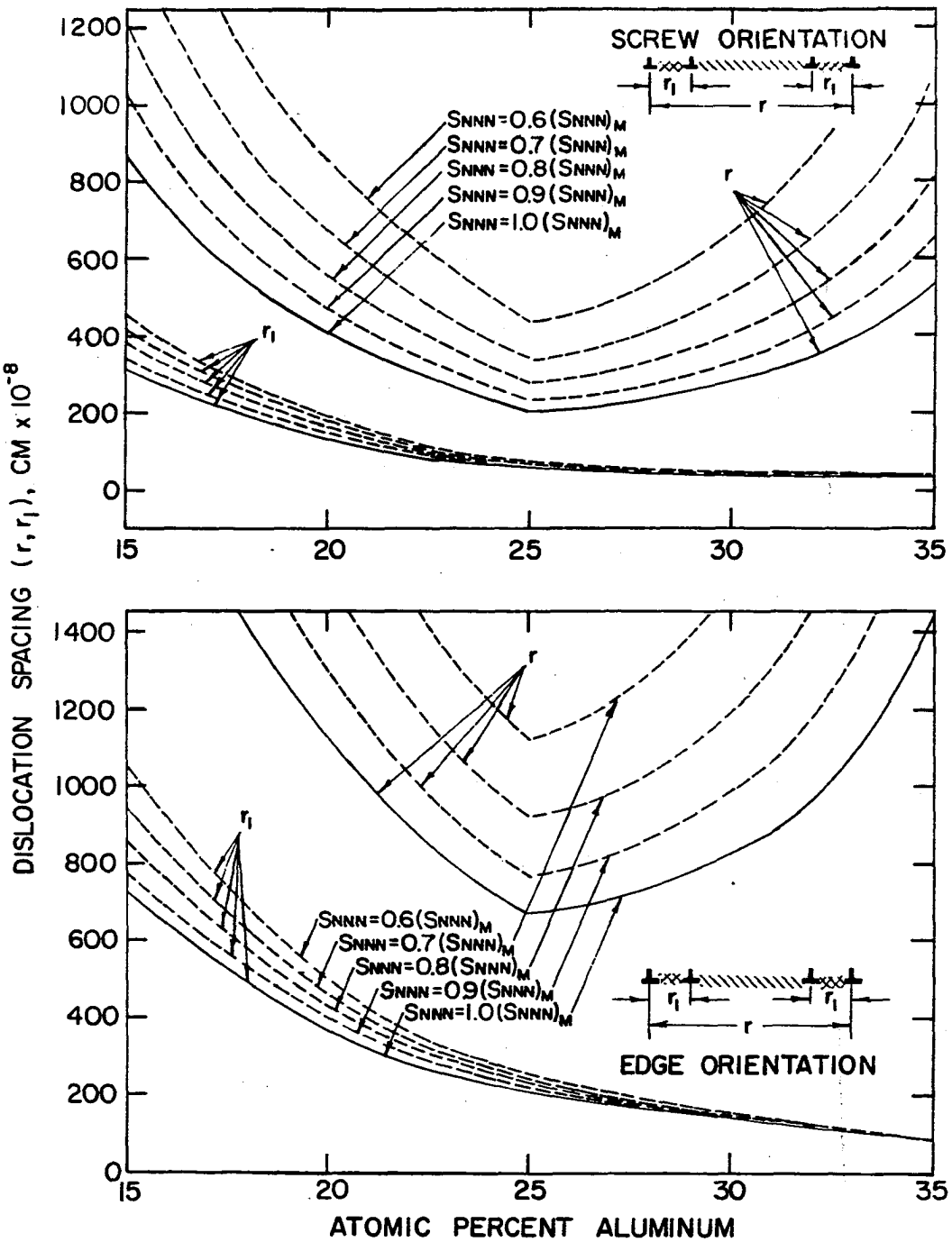

Figure 34. The composition dependence of type 12(a) dislocation spacings in Fe-Al alloys of various degrees of order

to variations in order and composition within the composition range of interest. Furthermore, the calculations of Appendix A show that these r_1 values are below the TEM resolution limit for dislocations. Thus, because the r values of both are similar, TEM observations are insufficient to distinguish between equilibrium configurations of type 12(a) and 12(b). In addition, both calculated r values are in reasonable agreement with those obtained from micrographs such as that shown in Figure 33.

It should be noted that the energy calculations of Appendix B are limited by their restriction to edge and screw orientations and that a complete solution for all orientations would permit calculation of the equilibrium shape of a complete dislocation loop (74). Results of such calculations (74,75) show that there exists an angular range of <111> dislocation instability for crystals of high elastic anisotropy. That is, an inverse Wulff (76) plot of the dislocation energies contains cusps so that the final equilibrium form of the loop will contain kinks made of straight line segments oriented parallel to the instability range limits (77). The existence of such kinks is quite strikingly evident in Figure 33 where the instability range is from 106° to 155° measured from [111] in the direction away from [010] (75).

Finally, it should be noted that the DO_3 superlattice dislocation segments which have not cross slipped from the foil appear to be coupled even though the pronounced line contrast asymmetry indicates that they are of like sign. This asymmetry, which is discussed in Appendix A, arises from the superposed contribution of parallel, like signed dislocation strain fields to $\bar{R}$. The apparent coupling of Figure 33 therefore, must be the result of large friction stresses which oppose the mutual repulsion of the like signed dislocations. In fact, Marcinkowski and Lakso (49) have shown that the repulsive force versus distance curves for like signed superlattice dislocation arrays contain pronounced minima which may represent positions of metastable equilibrium in the presence of finite frictional forces.

In addition to the apparent coupling of like signed dislocations, the formation of superlattice dislocation dipoles is also a predominant feature of stage I deformation. A typical stage I dislocation arrangement is shown in Figure 35 where the dipoles are readily identified by their symmetric image contrast. This micrograph also contains the usual like signed arrays and a rather unusual vertical array. Both Figures 33 and 35 contain evidence for the operation of only

Figure 35. Light field micrograph of dislocation arrays produced during stage I deformation of a 28.0 at.% Al alloy. This micrograph was obtained from the same specimen as that of Figure 32 and is oriented with [111] 20 counterclockwise degrees from the vertical. 20500X


22

one slip system. In summary, stage I deformation is characterized by motion of DO_3 superlattice dislocations on a single system and the formation of dipoles and like signed arrays.

A dislocation arrangement typical of that formed during stage II deformation is shown in Figure 36. This micrograph shows that the dislocations are predominantly screw oriented and that the screw to edge length ratio is large. This orientation preference is common to many materials of high elastic anisotropy (74) and is at least partially accounted for by the energy difference between the two orientations. Reference to Appendix B shows that the edge segment energy per unit length is nearly four times that for the screw orientation and that the edge dislocation mobility factor is more favorable by a factor of nearly twelve. Thus the motion of short edge segments and consequent formation of additional screw length is energetically more feasible than the converse process. This energy relationship is also evidenced in Figure 36 by the presence of narrow screw arrays which exhibit the symmetric image contrast characteristic of dipole configurations. These dipoles may be formed by the motion of pinned edge segments or alternatively, by the partial annihilation of unlike screw segments of adjoining slip loops.

Figure 36. Light field micrograph of the primary slip plane of a 28.0 at.% Al compression specimen which was strained to 25% γ at 298^{o}K


B
111
10̄1
01̄0
1̄11
1̄01
01̄0
1̄1̄1
000
202

In addition to these screw dipoles, a large number of edge dipoles may be observed in this figure. These dipoles exhibit two distinct types of image contrast as illustrated by the configurations immediately above and below "A" in this figure. The calculations of Appendix A suggest that the narrow image dipoles consist of overlapping dislocation arrays while the wide dipole images are formed by nonoverlapping arrays. This distinction is illustrated more clearly by the wide dipole images near "B". The presence of these dipoles is complimented by the presence of an approximately equal number of like signed arrays as identified by their asymmetric images. The near edge arrays of this type contain the kinks described previously for the case of Figure 33 and exhibit larger than equilibrium spacings. In fact, the individual $\frac{1}{4}a_o[111]$ dislocations which comprise the predicted type 12(a) superlattice dislocation are quite clearly resolved in the configuration located below "A" in this micrograph. In accord with the deformation scheme outlined previously, dark field observations of this and similar foils reveal no dislocation produced APB's; and tilting experiments fail to reveal dislocations in other than the primary slip system. This absence of dislocations on all but the primary system and the straightness of macroscopic slip lines indicates that cross slip,

other than that produced by the occasional annihilation of unlike screw segments, is not a predominant feature of stage II hardening. This is evidenced by the straightness of the screw segments in Figure 36 and by observations of similarly straight dislocations in foils oriented to contain only the [111] direction of the primary plane. In summary, stage II hardening in crystals oriented for single slip is produced by the interaction of type 12(a) dislocations on the primary system.

Examination of the dislocation substructure produced in stage IV is best accomplished when the deformation is uncomplicated by the presence of stages I and II. For this reason a crystal of 30.0 at.% Al was strained 10.0% at 77°K and examined by TEM. Figure 37 shows a typical dislocation configuration on the primary slip plane of this crystal. Although this micrograph is similar to that of Figure 36, the absence of large numbers of dipoles and a different type of image contrast may be noted. Even though the contrast in Figure 37 was produced by a higher order reflection, the images of the type 12(d) dislocations are somewhat sharper than those of the type 12(a) dislocations in Figure 36. The difference in contrast is better illustrated by Figure 38(a) which was obtained

Figure 37. Light field micrograph of the primary slip plane of a 30.0 at.% Al crystal which was strained to 10.0% γ at 77^{o}K

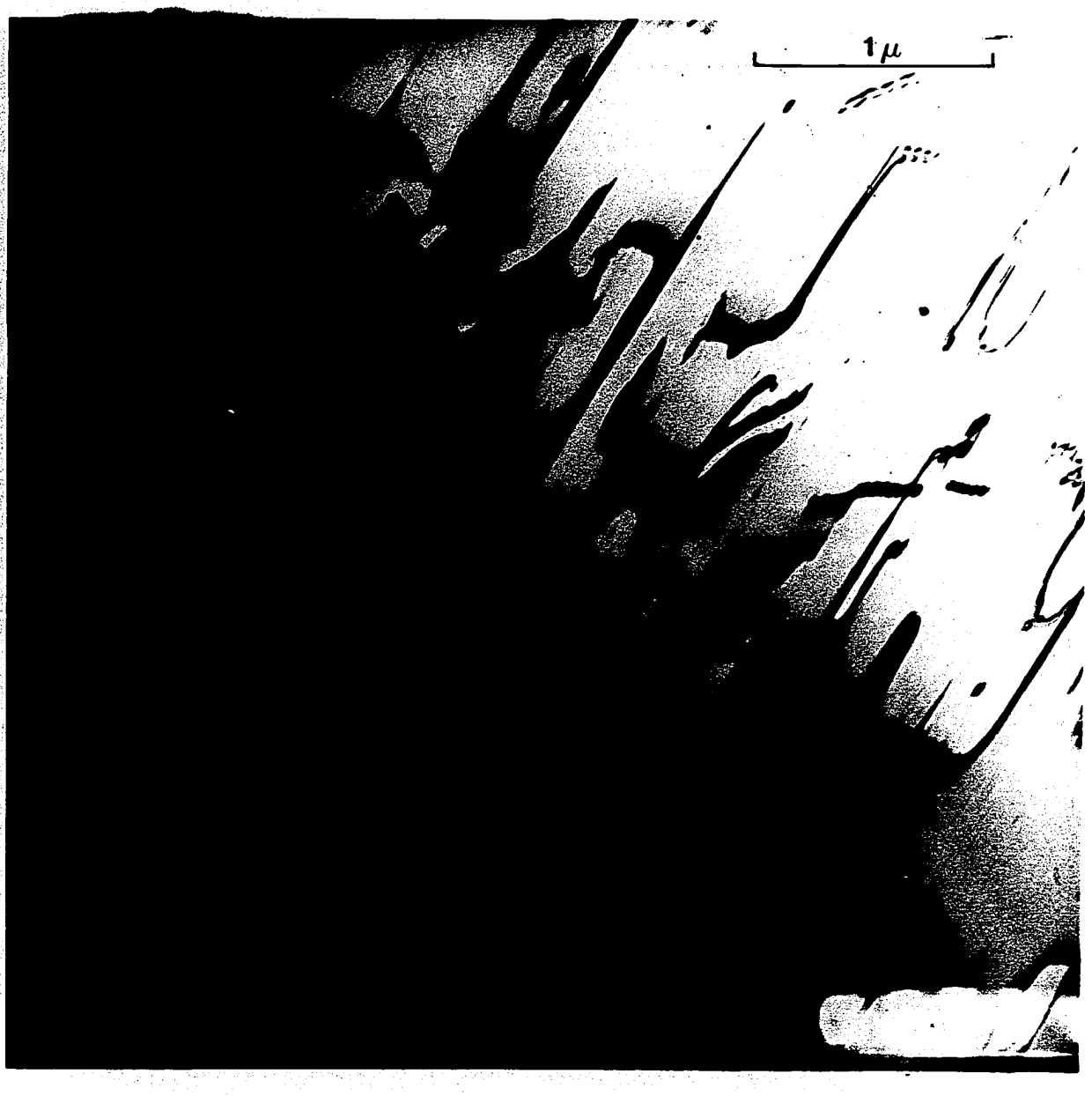
1μ

Figure 38. Transmission electron microscopical observations of a 30 at.% Al compression specimen which was deformed in stage IV at 77°K

(a) Light field micrograph of type 12(d) dislocations

(b) 111 dark field image obtained from the same specimen described for (a)

(c) 222 dark field image of the same area shown in (b)

(d) 111 dark field image obtained from the specimen described for (a)

222 DARK FIELD

111 DARK FIELD

from a near $(\bar{1}\bar{1}1)$ oriented foil of the same crystal. Here, the contrast was produced by a 202 reflection and shows that the $\frac{1}{2}a_o\langle 111\rangle$ dislocations produce sharp, narrow images when separated at large distances. The spacings of the dislocations in Figure 37; 130Å for the screw segments and 370Å for the edge segments, compare well with calculated values of 120Å and 357Å, which were obtained by setting $r = Kb^2/2\pi(\gamma_1-\gamma_2)$. Further evidence that these are dislocations of type 12(d) is given in Figures 38(b) and 38(c). Figure 38(c) is a 111 dark field image of this same specimen which clearly shows the type 2 APB's produced by motion of the type 12(d) dislocations. Figure 38(b) is a 222 dark field micrograph of the same area which, as expected for APB's of this type, shows no APB contrast. Finally, the straightness of the dislocation produced APB's in Figure 38(d) may be taken as evidence for the relative infrequency of cross slip in stage IV deformation. Thus, stage IV is characterized by the motion of type 12(d) dislocations of a single slip system with consequent production of type 2 APB's.

Since Figure 27 indicates that superlattice dislocation nucleation in 28.0 at.% Al alloys is difficult at low temperatures, a crystal of this composition, which had been deformed

5.0% at 77°K, was also examined by TEM. Figure 39, although slightly misoriented with respect to the primary slip plane, shows that the predominant feature of this deformation is the cross slip of ordinary $\frac{1}{2}a_o[111]$ dislocations. Indeed, although some loosely coupled type 12(d) dislocations are present in this micrograph, the wavyness of the screw segments indicates that these are rather easily uncoupled at the stress levels attained during deformation at this low temperature. Graphic evidence for the cross slip of ordinary dislocations in this stage V deformation is given in Figure 40. Here, the tortuous path of the $\frac{1}{2}a_o\langle 111\rangle$ dislocations is revealed by the APB's which were produced by their motion.

A similar investigation of stage V deformation was performed for the case of the two phase alloy. In this instance the crystal was strained 17.0% at room temperature and wafered on the primary slip plane. Figure 41 shows that the dislocation arrangement in this crystal is similar to that observed in disordered b.c.c. alloys. That is, the dislocations are contorted and evidence for cross slip is apparent. By way of contrast however, 6.0% deformation of a similar crystal at 573°K produces the dislocation arrangement shown in Figure 42. This arrangement resembles that produced by

Figure 39. Light field micrograph of the primary slip plane of a 28.0 at.% Al compression specimen which was strained to 5.0% γ at 77^{o}K


010
111
101
$\bar{1}11$

Figure 40. 111 dark field micrograph of the 28.0 at.% Al specimen described for Figure 39

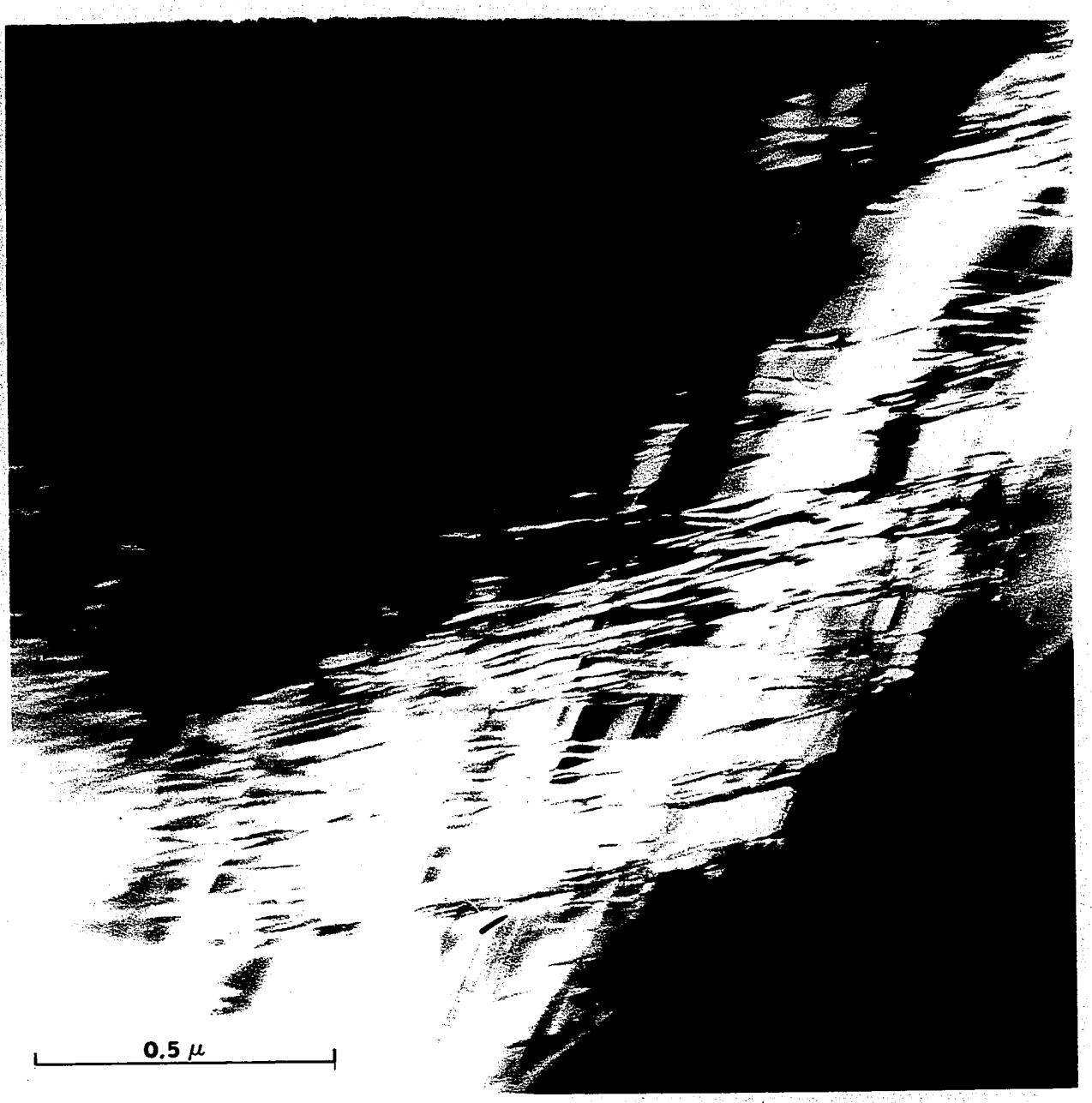
0.5 μ

Figure 41. Light field micrograph of the primary slip plane of a 23.8 at.% Al compression specimen which was strained to 17.0% γ at 298°K

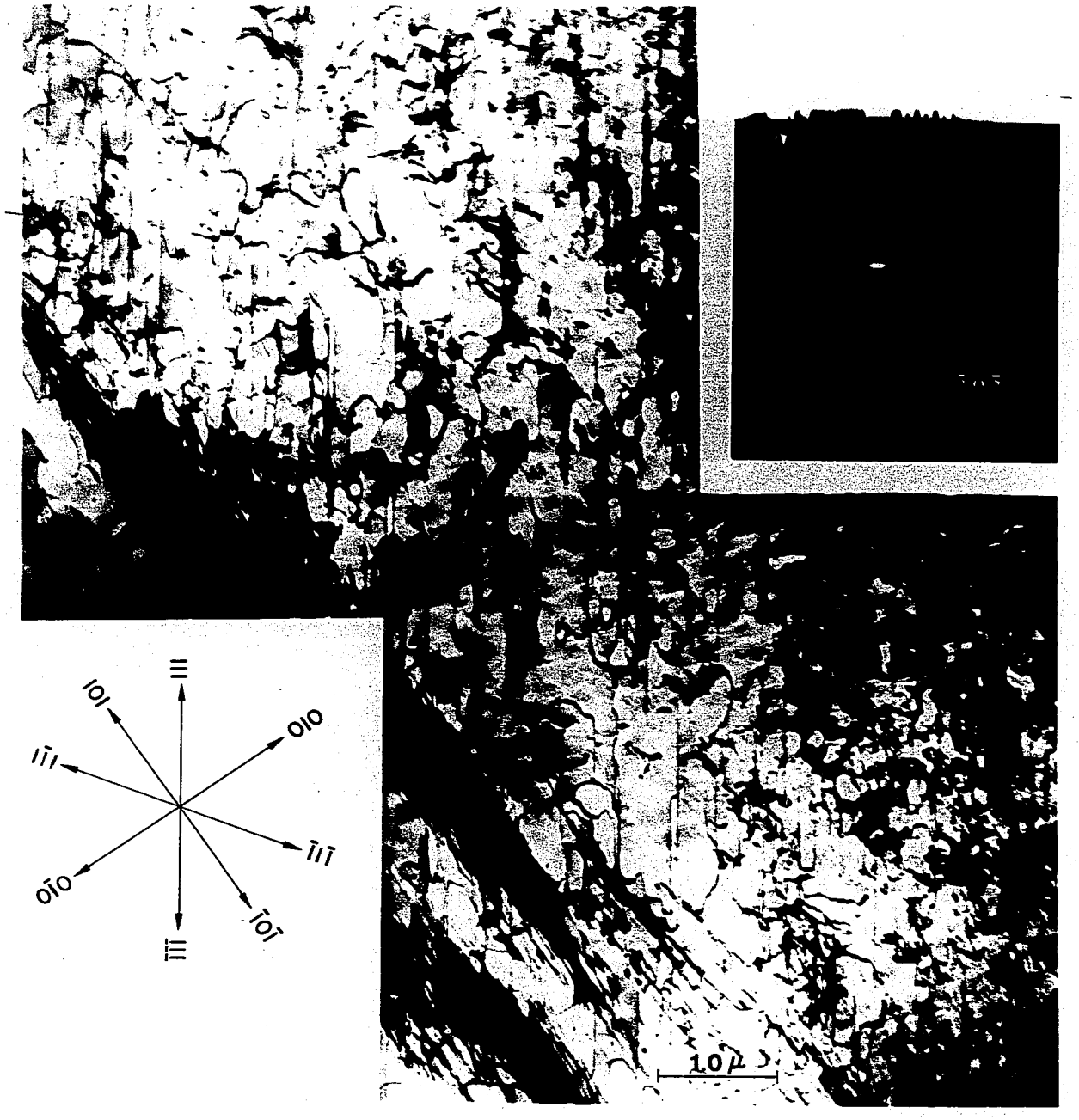
111
101
010
1$\bar{1}$1
1$\bar{1}$$\bar{1}$
0$\bar{1}$0
10$\bar{1}$
$\bar{1}\bar{1}\bar{1}$
10μ

Figure 42. Light field micrograph of the primary slip plane of a 23.8 at.% Al compression specimen which was strained to 6.0% γ at 573^{o}K

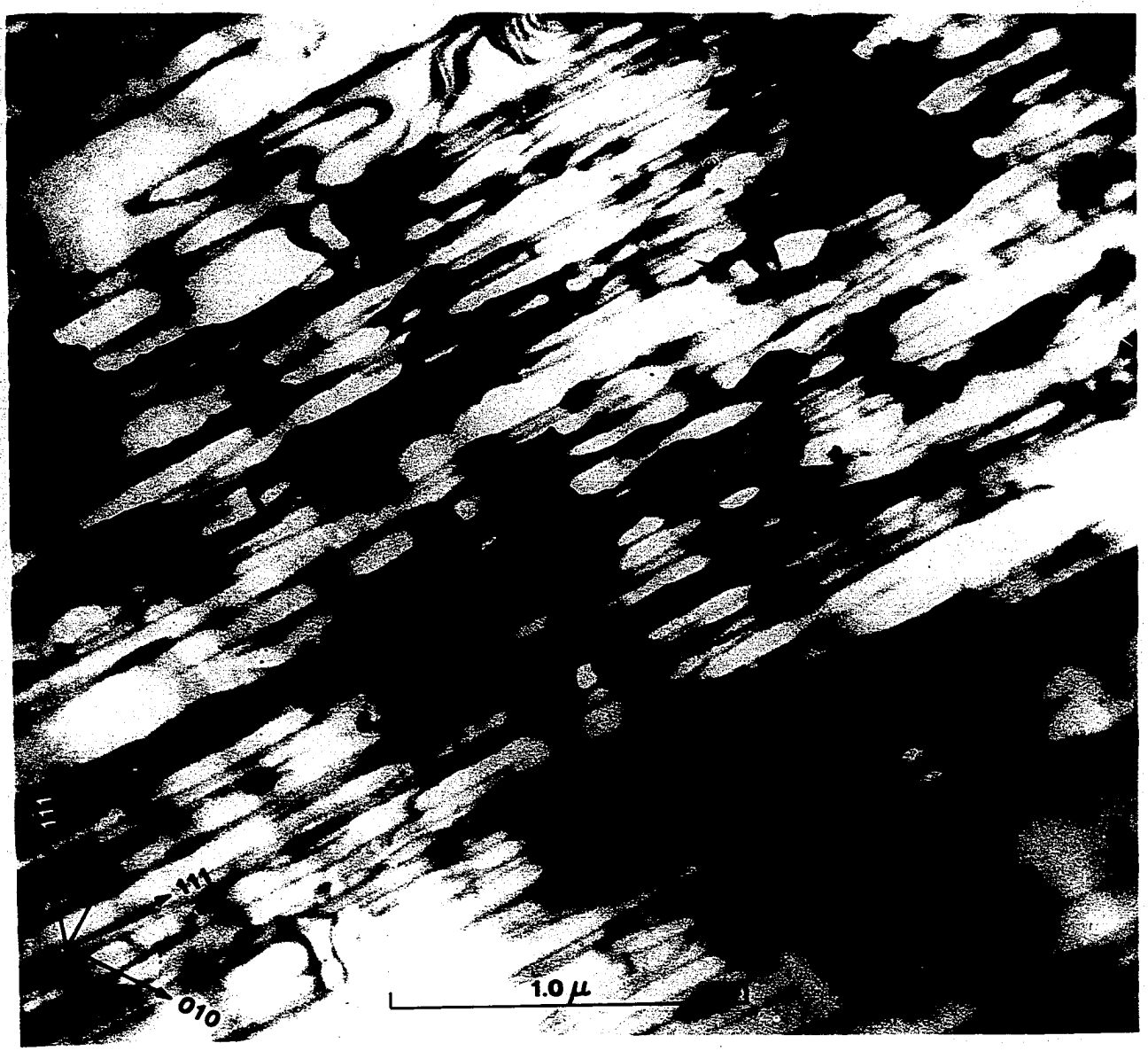
111
-111
010
1.0 μ

stage II deformation in crystals of higher aluminum content, (c.f. Figure 36). It is therefore apparent that the existence of the two phase structure has little influence upon the deformation behavior of these alloys when the volume fraction of ordered phase is large. Figure 43 is a 111 dark field micrograph of the same area which shows that no APB's are produced by dislocation motion, as is characteristic of stage II deformation.* Further evidence for the absence of cross slip in stage II is provided by Figure 44. This micrograph was obtained from a foil oriented perpendicular to the compression axis so that the screw segments of the primary system are inclined at 45° with respect to the foil normal. Here it will be noted that dislocations of the maximum resolved shear stress slip system only are present, and that significant numbers of these are arranged in either dipole or like signed arrays. Since the weak superlattice reflection contrast in this figure is sufficient to reveal the ordered phase boundaries but does not reveal any APB's; no imperfect superlattice dislocations are present within this slip band.

---

*The image contrast parallel to [111] in this figure is produced by foil distortions associated with the long screw segments shown in Figure 42.

Figure 43. 111 dark field micrograph of the same area shown in Figure 42

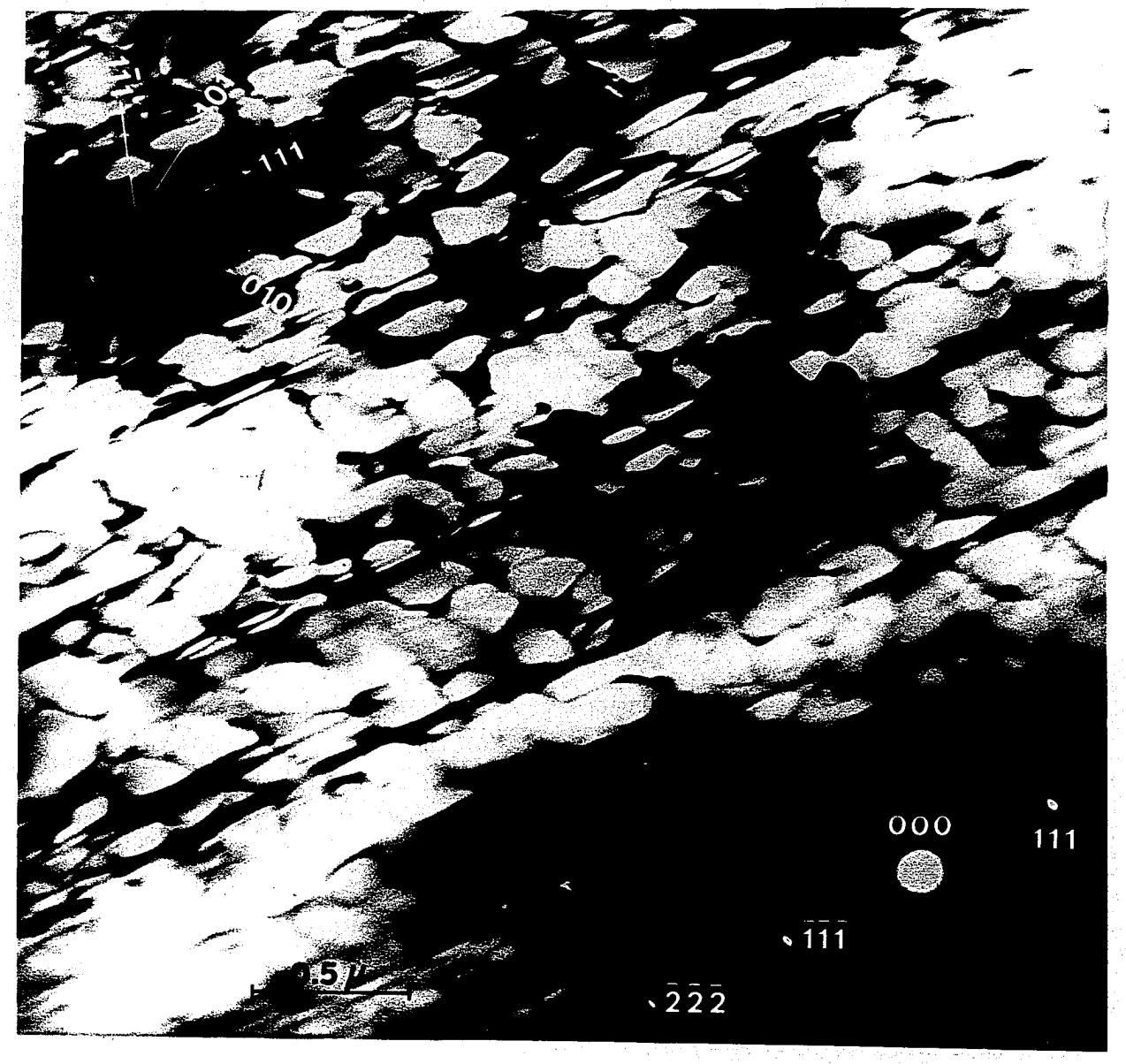
111
010
000
111
$\bar{1}\bar{1}\bar{1}$
$\bar{2}\bar{2}\bar{2}$

Figure 44. Light field micrograph of a foil oriented perpendicular to the compression axis of the specimen shown in Figures 42 and 43


111 (PRO

In all of the preceding examples the absence of cross slip during the linear deformation stages leads to the formation of high dislocation density substructure. A striking example of this substructure is shown in Figure 45, which is a light field micrograph of the primary slip plane of a 28.0 at.% Al crystal which was strained into stage V at 198°K. Even at this high strain, the predominant screw orientation of the dislocations is evident although the array is so dense that resolution of individual dislocations is not possible. It may be further noted that the foil distortion resulting from this array was sufficient to produce all first <101> Laue zone reflections, regardless of the degree of foil tilt. Thus, in contrast to the tangled wall formation observed in pure metal crystals, extensive linear stage deformation of these alloys is associated with the formation of a uniform substructure of very high dislocation density. 020 and 111 dark field images of this specimen are shown in Figures 46 and 47, respectively. Figure 46 reveals a high density of APB's of type 1, as expected for stage V deformation, while Figure 47 shows a similarly high density of APB's of both types. The selected area diffraction patterns of these figures show that the high APB density produces streaking of the superlattice reflections.

Figure 45. Light field micrograph of the primary slip plane of a 28.0 at.% Al crystal which was strained to 60.0% γ at 198^{o}K

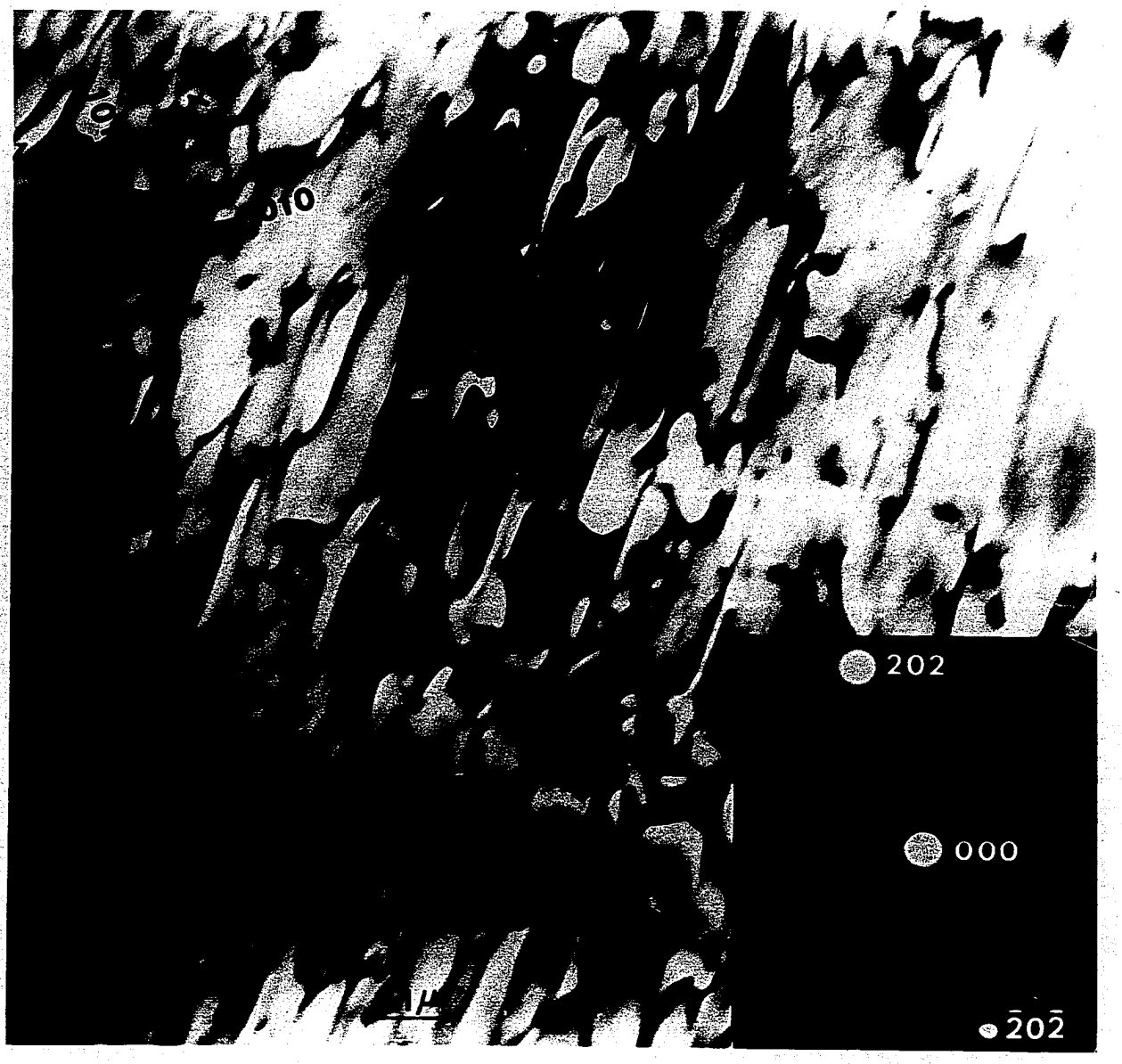
202
000
$\bar{2}0\bar{2}$

Figure 46. 020 dark field image of the specimen shown in Figure 45

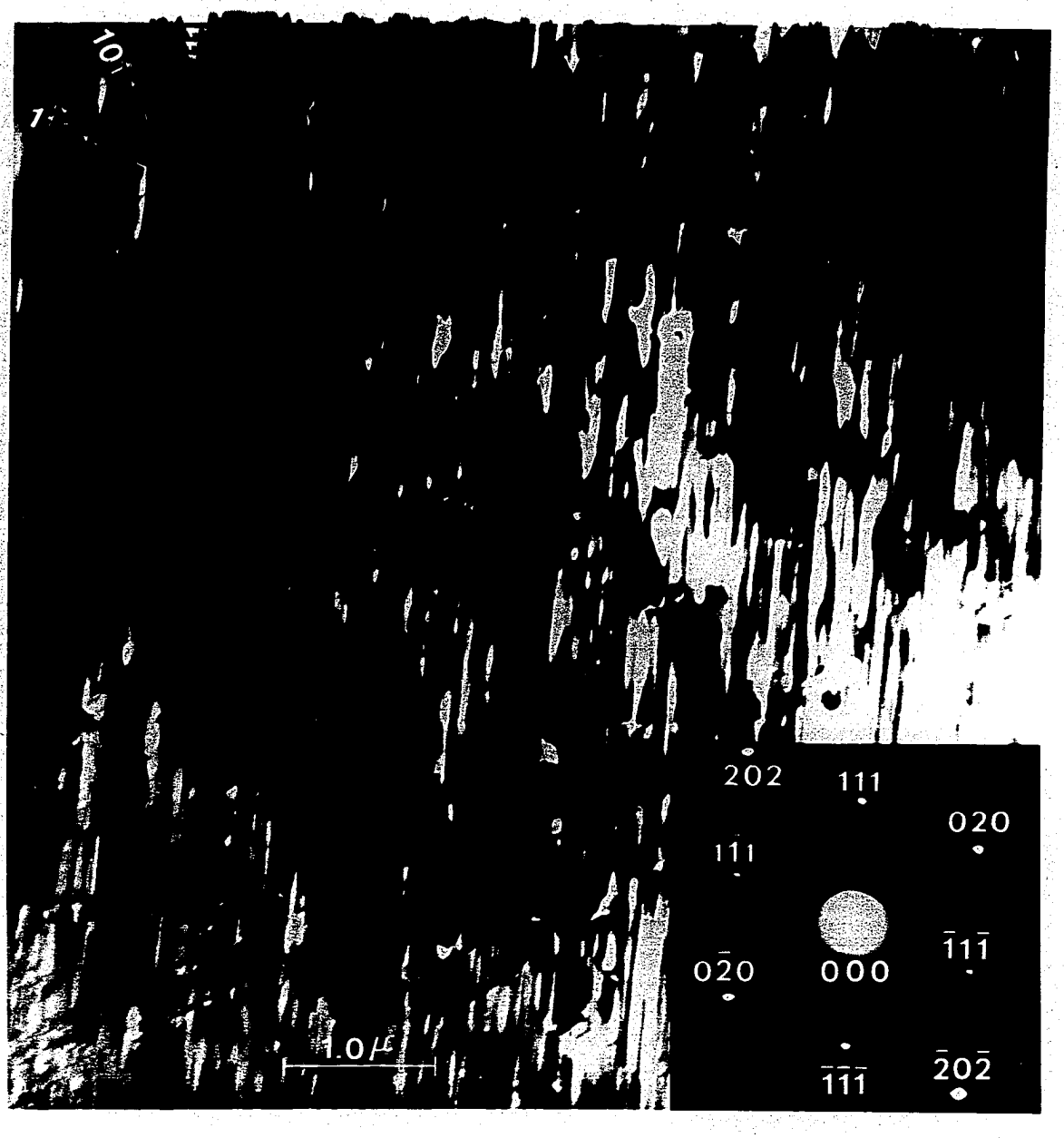
202
111
020
111
020
000
111
111
202
1.0μ

Figure 47. 111 dark field image of the specimen shown in Figure 45

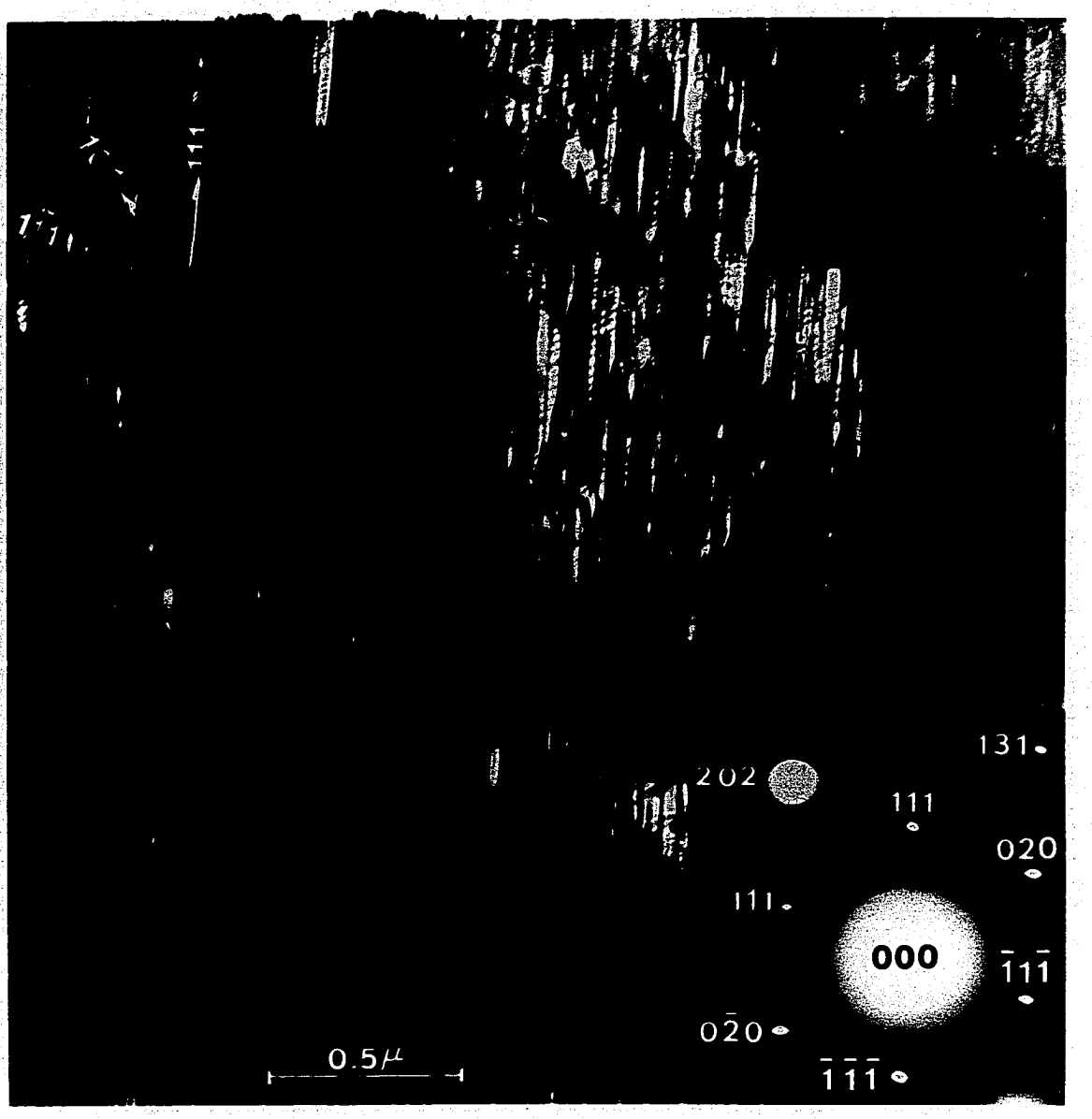
111
111
202
131
111
020
111
000
$\bar{1}\bar{1}\bar{1}$
$0\bar{2}0$
$\bar{1}\bar{1}\bar{1}$
0.5μ

In both cases these streaks are perpendicular to the APB traces and thus may be attributed to ordinary particle size broadening (78). Therefore, the APB traces parallel to [010] in Figure 47 are of type 2 since only the S_{DO_3} reflections are streaked perpendicular to this direction.

Although a majority of the single slip oriented crystals tested in this study did deform by single slip, a few exhibited slip traces of several $\langle 111 \rangle \{110\}$ systems. These crystals, which invariably contained some macroscopic defect, provided opportunity for examination of double slip dislocation interactions. The primary slip plane of one such crystal is shown in Figure 48 where the primary system dislocations exhibit the familiar [111] orientation and an additional $[1\bar{1}1]$ orientation. In many instances these $[1\bar{1}1]$ segments have been pinned by the short secondary system screw segments lying along $[0\bar{1}0]$. Since $[0\bar{1}0]$ is the projected direction of $[\bar{1}\bar{1}1]$ and [111], these dislocations probably glide on the (011) $[\bar{1}\bar{1}1]$ system. The latter possesses the highest Schmid factor of the geometrically possible systems. The evidence for pinning in this micrograph suggests that the intersection - jog model (44) for work hardening is probably inapplicable to this case. Indeed, the dark and light field micrographs of Figure 49

Figure 48. Light field micrograph of a 28.0 at.% Al crystal which was strained 11.0% γ at 298^{o}K

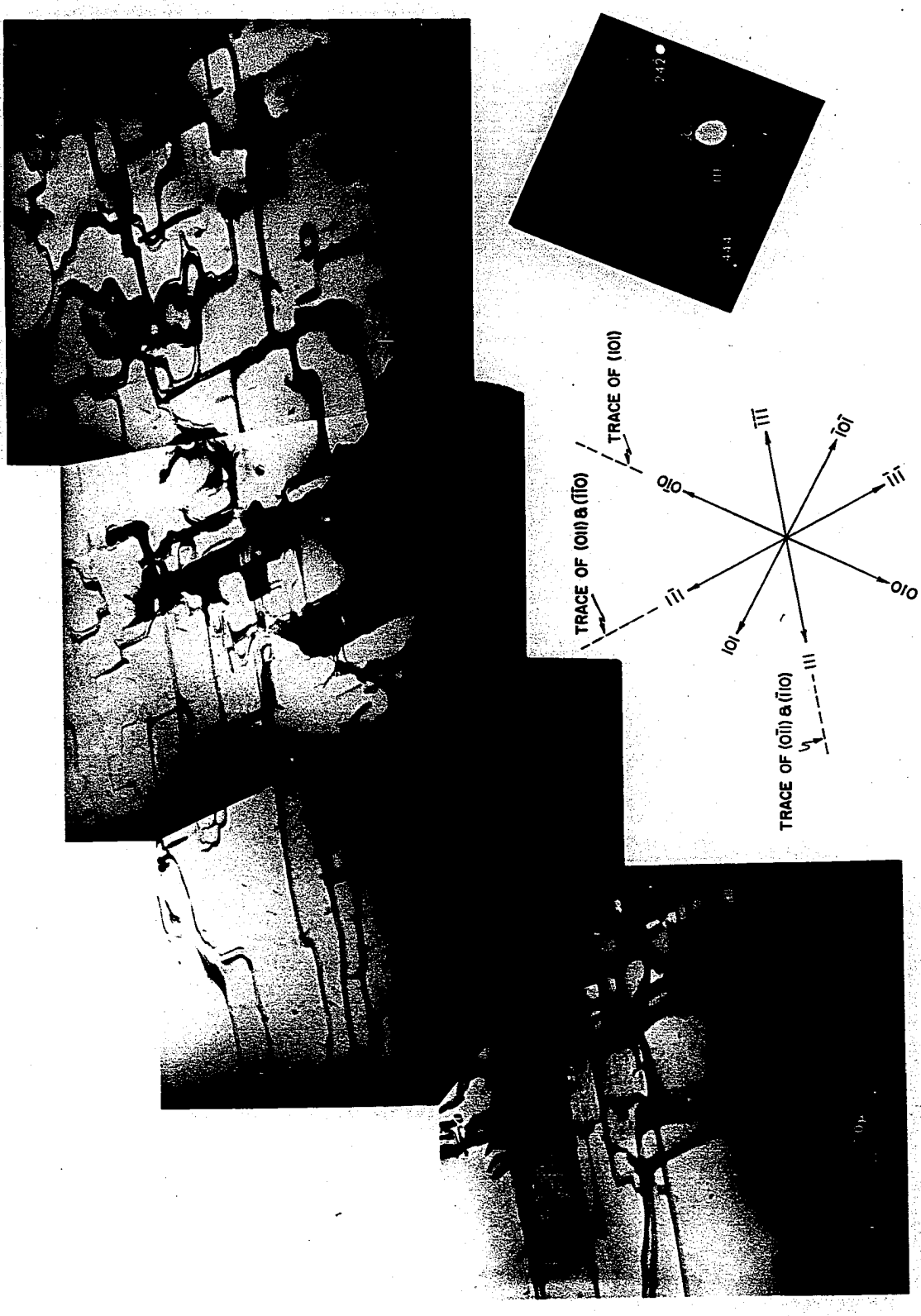
TRACE OF (101)
TRACE OF (011) & (1$\bar{1}$0)
TRACE OF (0$\bar{1}$1) & ($\bar{1}$10)
$\bar{1}\bar{1}\bar{1}$
$\bar{1}0\bar{1}$
$\bar{1}\bar{1}1$
010
$\bar{1}$01
$\bar{1}$11
111
0$\bar{1}$0

Figure 49. Dark and light field observations of double slip interactions in a 28.0 at.% Al alloy

(a) 111 dark field image of the specimen shown in Figure 48

(b) Light field image of the specimen area shown in (a)

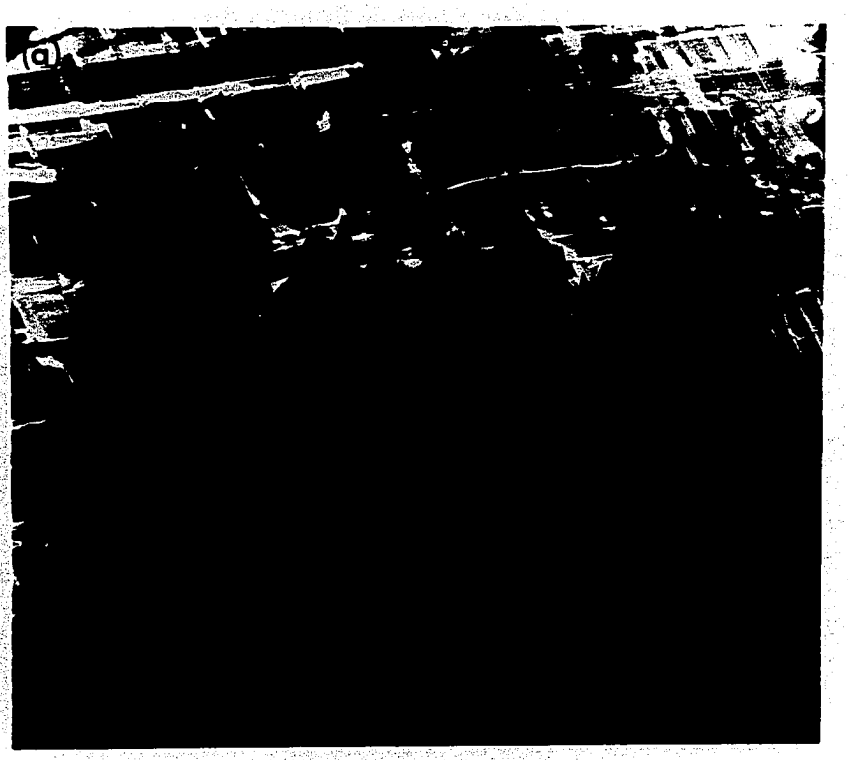

(111) DARK FIELD

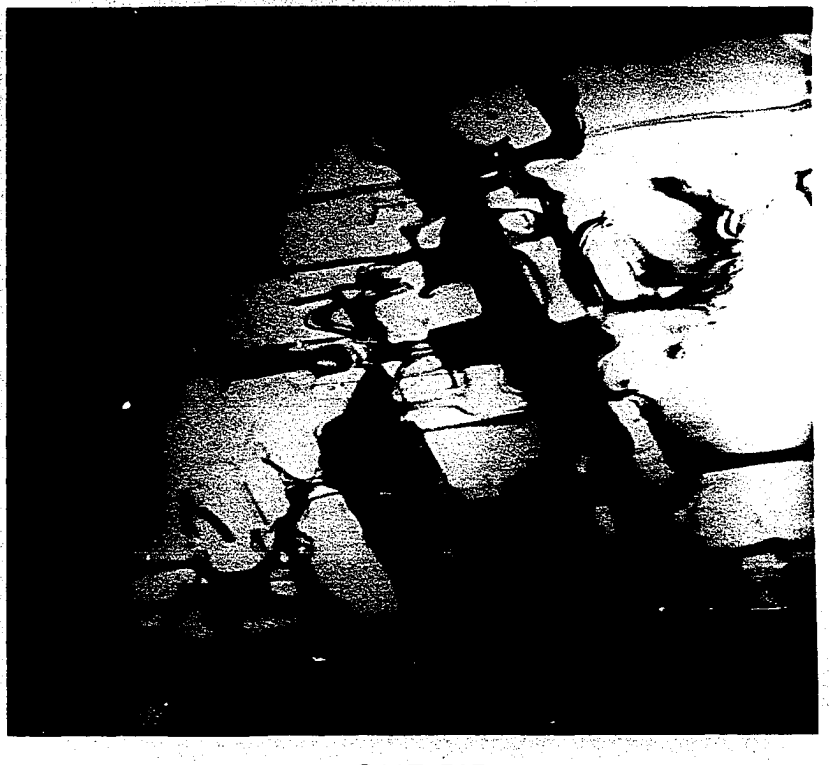

LIGHT FIELD

suggest that the bowing out of superlattice dislocations around the pinning points is the critical event required for further deformation. These micrographs were obtained from the same foil area and foil orientation as that shown in Figure 48. The very weak 111 reflection micrograph reveals APB's which exhibit strong fringe contrast. This arises because the deviation from Bragg orientation of the 111 reflection, $\bar{s}_{111}$, is large so that the effective extinction distance: (79)

$$t_e^w = \frac{t_e}{1+(s_{111}\, t_e)^2} \quad , \tag{21}$$

is decreased. Inspection of Figure 49 shows that both thermal and dislocation produced APB's are present in this foil, the latter oriented along the trace of (011). These were therefore produced by the motion of the secondary system dislocations visible in Figure 49(b). This observation suggests that motion of superlattice dislocations through the dense primary array is so difficult as to lead to the eventual uncoupling of the secondary system dislocations. That is, when the primary array spacing is small, the stress required for APB production will be lower than that required for production of a bow out of critical radius. Thus the inception of secondary

slip in ordered alloys is difficult. In fact, several workers (80,81,82) have reported that long range ordered alloys commonly deform via single slip even after tensile axis rotations well beyond the symmetry line.

ANALYSIS OF EXPERIMENTAL RESULTS

The experimental results presented in the preceding sections clearly indicate that the deformation behavior of long range ordered iron-aluminum alloys is determined by the nucleation and interaction of superlattice dislocations of various types. Analysis of this deformation behavior may therefore be conveniently discussed in terms of one or the other of these processes.

Nucleation of Superlattice Dislocations

The nucleation of superlattice dislocations has recently been treated in some detail by Marcinkowski and Leamy (65). The following analysis is based upon their treatment. Of the many processes by which dislocation line length may be increased, tractable energy expressions may be written only for the case of the expansion of circular loops. Marcinkowski and Leamy therefore treated the nucleation process by considering the formation of such loops under the action of an external stress in an otherwise dislocation free crystal. Although application of this simple model requires the assumption of rather large local stress concentrations, the results of such an analysis are expected to be similar to those

obtained from more refined treatments.

Briefly, these authors have shown that nucleation of type 12(a) dislocation loops is most easily accomplished by a stepwise process in which each $\frac{1}{2}a_o\langle 111\rangle$ loop forms and expands to large size before the following loop is nucleated. Figure 50, which is taken from reference (65), shows that the energy of a single loop attains a maximum, E_{T_c}, at some critical loop radius, R_c. Formation of a stable loop therefore requires thermal assistance in the amount E_{T_c}. For the individual loops which comprise a type 12(a) dislocation the stress, τ_{R_c}, required for formation of a loop of critical radius R_c, and its energy, E_{T_c}, at this radius may be computed from:

$$\tau_{R_c} = \frac{(\frac{2}{\nu} - 1)}{2(\frac{1}{\nu} - 1)} \frac{\mu b}{4\pi R_c} [\ln(4R_c/\epsilon)-1] + \Delta\gamma/b \qquad (22)$$

$$E_{T_c} = \frac{(\frac{2}{\nu} - 1)}{2(\frac{1}{\nu} - 1)} \frac{\mu b^2}{2} R_c[\ln(4R_c/\epsilon)-2] - \pi R^2(b - \Delta\gamma/b) \qquad (23)$$

where b is the Burger's vector, $\mu = (c_{11}-c_{12}+c_{44})/3$ is the shear modulus on the slip plane in the direction of the Burger's vector, ν is Poisson's ratio, ϵ is the inner cut off radius, and $\Delta\gamma$ is the energy of the APB within the loop

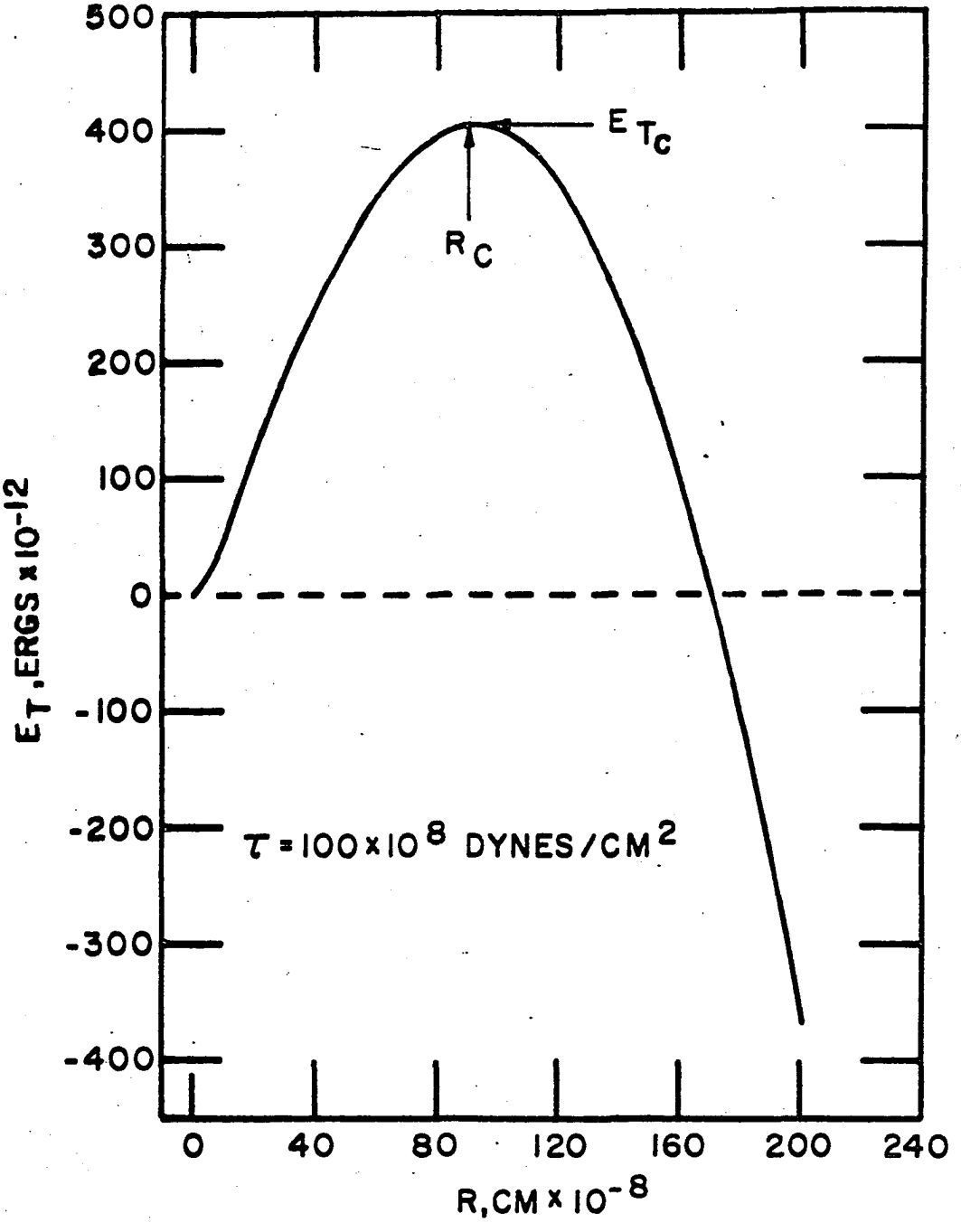

Figure 50. Typical energy versus radius plot for a single dislocation loop

minus that outside the loop. These τ_{R_c} and E_{T_c} values differ from those for ordinary loops in pure metals by the $\Delta\gamma/b$ factor which accounts for the tension of the APB's formed by the loops. The energy required for superlattice dislocation formation on this model, E_Σ, is given by the sum of those required for the individual processes. Calculated values of these quantities for Fe-Al alloys of various composition are given in Figure 51. The lower dashed curve for each alloy describes the energy versus stress relation for an identical disordered alloy while the numbered curves correspond to the individual $\frac{1}{2}a_o\langle 111\rangle$ loops which comprise the complete superlattice dislocation. E_Σ values are also given in this figure where $E_{\Sigma\ 1+2+3+4}$, $E_{\Sigma\ 1+2}$, and $E_{\Sigma\ 1}$ correspond to the formation of loops of type 12(a), 12(d), and 12(c). For alloys of 27.5 and 30.0 at.% Al Figure 51 shows that above stress level "B", formation of the first loop is followed by the formation of the remaining loops without activation. Similarly, above stress "A", formation of the first loop results in the unaided formation of the second loop while formation of the third loop requires the introduction of additional energy. For the case of 22.0 and 25.0 at.% Al alloys however, $\tau_A = \tau_B$ and below this stress additional

Figure 51. Dislocation loop nucleation energies, E_{Σ}, for Fe-Al alloys. Nucleation energies for the individual $\frac{1}{2}a_o\langle 111\rangle$ loops are given by the numbered curves.

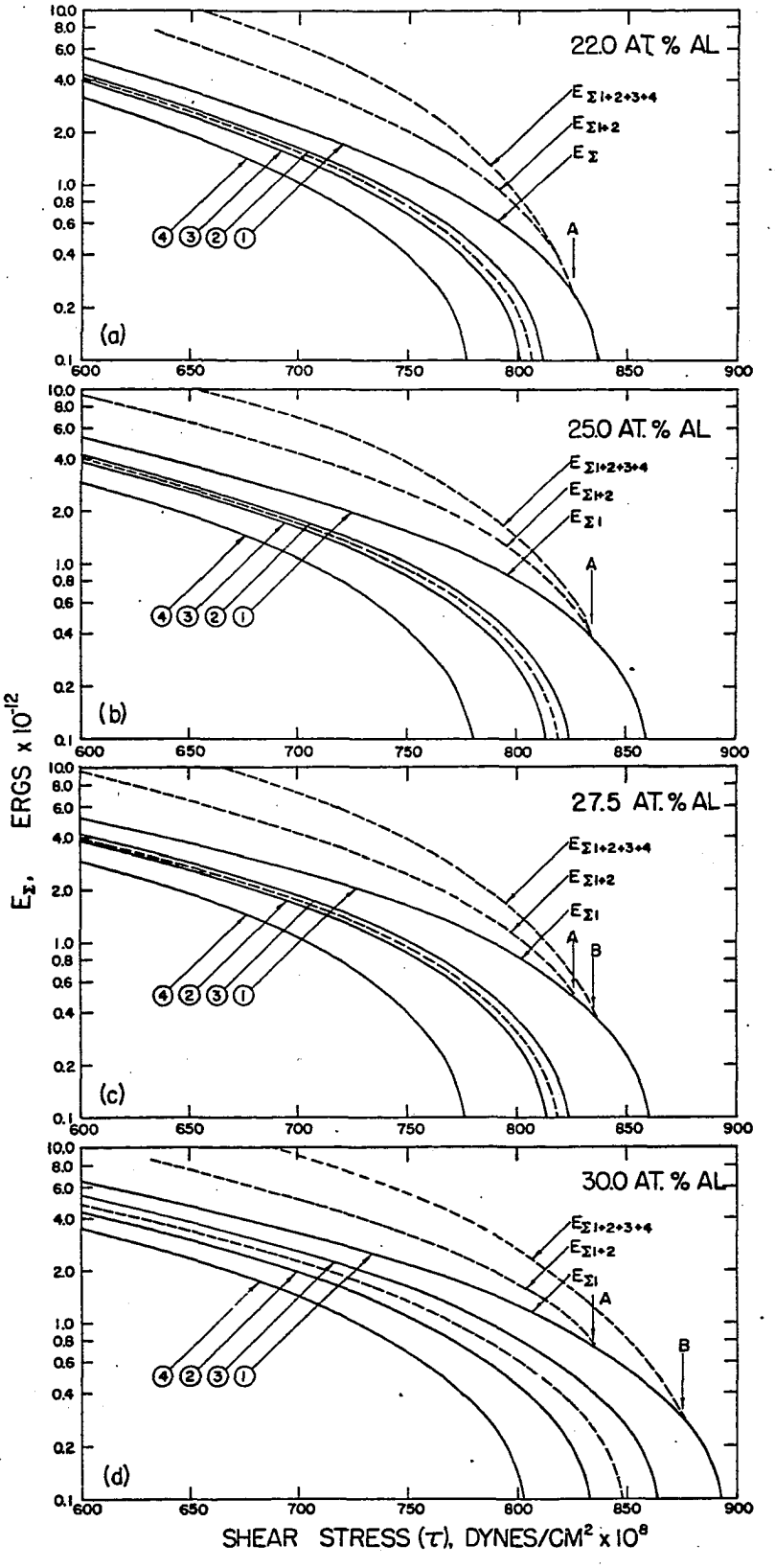
22.0 AT. % AL
25.0 AT. % AL
27.5 AT. % AL
30.0 AT. % AL
(a)
(b)
(c)
(d)
$E_{\Sigma 1+2+3+4}$
$E_{\Sigma 1+2}$
E_{Σ}
$E_{\Sigma 1}$
A
B
E_{Σ}, ERGS x 10^{-12}
SHEAR STRESS (τ), DYNES/CM^2 x 10^8

energy is required for nucleation of both type 12(a) and type 12(d) loops. Because $\gamma_1 < \gamma_2$ for the low aluminum content alloys, the formation of the second loop in these always requires additional energy.

Prediction of the dislocation type responsible for deformation at a given temperature requires that the strain rate, $\dot{e}$, be considered. In general, the plastic strain rate of a crystal may be written:

$$\dot{e} = A \xi \sum_i N_i b_i \exp(-E_{\Sigma i}/kT) \qquad (24)$$

where N is the volume density of nucleation sites, A is the area swept out by each nucleated loop, $\xi = 1.0 \times 10^{12} sec^{-1}$ is the Debye frequency, and T is the absolute temperature. In this equation the summation includes every possible mechanism of dislocation production and b is understood to correspond to the mechanism under consideration.

At ordinary temperatures dislocation loops are produced in pure metal crystals at low stresses, whereas whiskers require stresses on the order of the theoretical shear stress. The model under consideration here is analogous to the case of whisker deformation. Thus the stress value appropriate for consideration of the energies involved in superlattice loop nucleation is that required for formation of single loops

in a disordered lattice at the temperature in question. The temperature dependence of this stress, τ^*, may be calculated if N and A are known. However, for purposes of this discussion, τ^* may be taken equal to the theoretical shear stress, $\sim \mu/7$. This yields τ^* values of 800, 807, 810, and 840 dynes/cm^{2}x10^8 for alloys of 22.0, 25.0, 27.5 and 30.0 at.% Al respectively.

For application of Equation 24 at applied stress levels below τ_{II} only nucleation of type 12(a) loops need by considered. For example, the 28.0 at.% Al data of Figure 27 show that stage I first appears at 240^{o}K. For this alloy τ^* = 808 dynes/cm^{2}x10^8 and $E_{\sum 1+2+3+4} = 1.3\text{x}10^{-12}$ erg. If A is taken as the area of the slip plane, ~0.5 cm^2, N must be approximately 3.6x10^{9}cm^{-3} if the impressed shear strain rate, 16x10^{-4}sec^{-1}, is to be satisfied by the motion of type 12(a) dislocations. Below 240^{o}K however, insufficient thermal energy is available for the activation of N sources so that a portion of the applied strain is accommodated elastically and the work hardening rate increases rapidly with decreasing temperature as is evidenced in Figure 28.

At applied stress levels between τ_{II} and τ_{IV} loops of type 12(d) expand freely once nucleated. Therefore, since

$E_{\Sigma\ 1+2} < E_{\Sigma\ 1+2+3+4}$ only loops of this type need be considered and $N_{12(d)} = 2N_{12(a)}$. The 27.5 at.% Al curves of Figure 51, which are similar to those for the 28.0 at.% Al alloy, show that only in a narrow range of temperature is nucleation of type 12(d) loops sufficient for accommodation of the applied strain rate. Finally, at low temperatures, only nucleation of type 12(f) loops is possible, the number depending upon the temperature, and the stress rises rapidly to τ_{IV} where these dislocations are mobile and account for the applied strain rate.

This same reasoning may be applied to the case of 30.0 at.% Al alloys to show that stage I should first appear at 260°K and that stage IV yield behavior is expected at lower temperatures. The latter conclusion arises from the fact that $E_{\Sigma\ 1} = E_{\Sigma\ 1+2}$ at τ^*. In general, the dislocation type nucleated at the yield depends sensitively upon the values of E_{Σ}, higher temperatures being requires for activation of high E_{Σ} value processes. Inspection of Figure 7, however, shows that stage V deformation persists to high temperatures in alloys in the concentration range from 24 to approximately 27 at.% Al, in apparent contradiction to the reasoning outlined above. This anomalous behavior, which accounts for the

abrupt decrease in yield stress near 27 at.% Al, occurs in the exact composition range where $\gamma_1 < \gamma_2$. Explanation of this behavior requires further consideration of the stepwise nucleation process.

The preceding analysis is based upon the assumption that each loop expands to large size prior to formation of the following loop so that the interaction between loops may be neglected. The effect of such interaction may be estimated, within the limitations of a static analysis, by consideration of Figure 52. In this figure the energy[1], E_T, of a type 12(d) loop configuration in a 28.0 at.% Al alloy, has been plotted against both R_1 and R_2. Here it may be noted that the double loop configuration is metastable with respect to the single loop configuration over a range of R_1 values. In addition, formation of the second loop in the stress field of the first requires additional energy, even when the double loop is the more stable configuration. Thus, when $\gamma_1 > \gamma_2$, the first loop expands until this additional energy has decreased to a value equal to that available thermally, whereupon the second loop is nucleated. These two loops are

---

[1]Interaction energy expressions are given in reference (65) and need not be repeated for purposes of this qualitative discussion.

Figure 52. Energy versus radius curves for a double loop configuration in a 28.0 at.% Al alloy. The numbered curves give the inner loop radius (R_2) energy relations for the fixed outer loop radii (R_1) shown

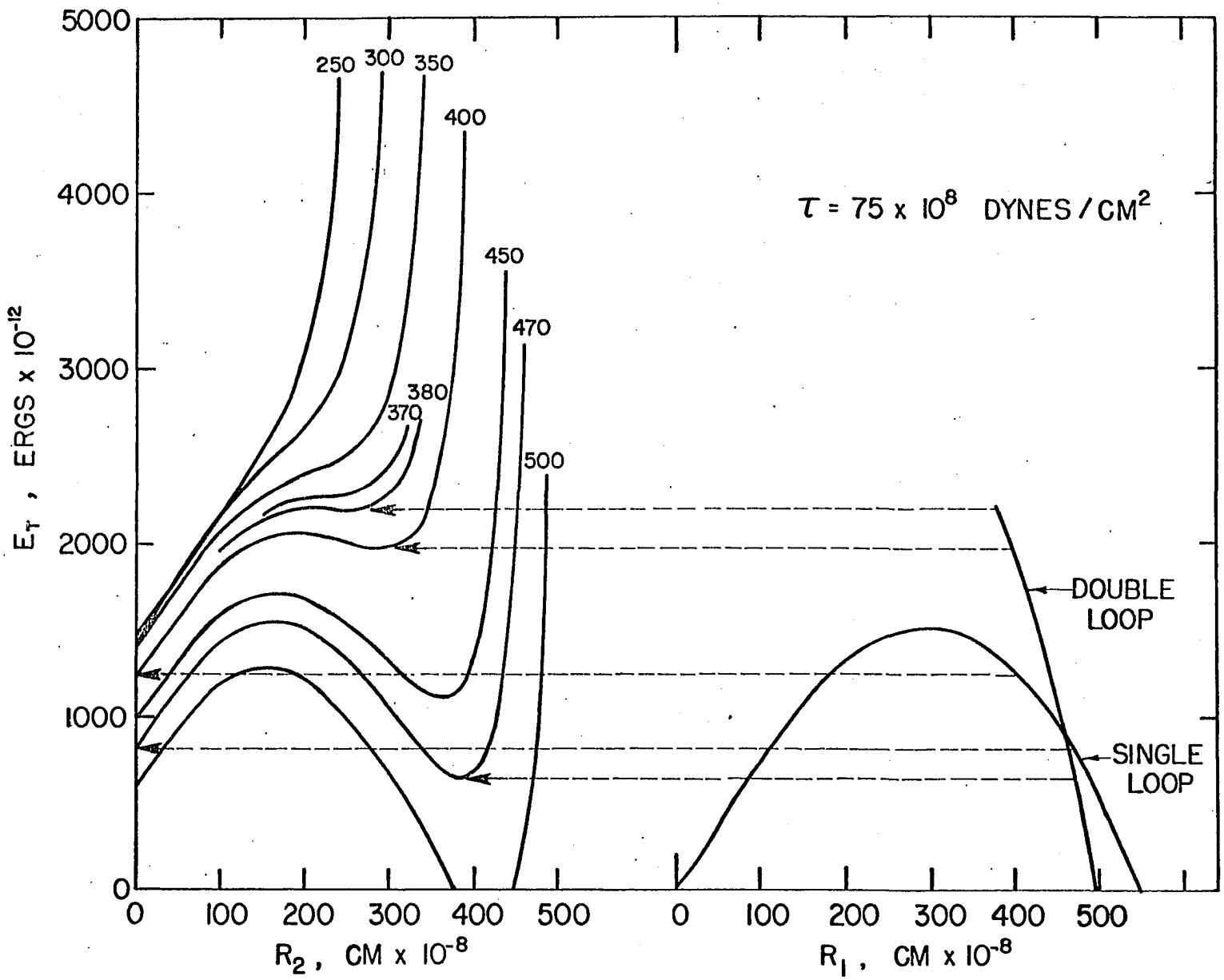
5000
4000
3000
2000
1000
0
250
300
350
400
450
470
500
380
370
τ = 75 x 10^8 DYNES / CM^2
E_T , ERGS x 10^-12
DOUBLE LOOP
SINGLE LOOP
0 100 200 300 400 500
R_2 , CM x 10^-8
0 100 200 300 400 500
R_1 , CM x 10^-8

strongly coupled by the type 1 APB lying between them and are thus constrained to remain on the slip plane during nucleation of the trailing loop pair.

For alloys in the composition range where $\gamma_1 < \gamma_2$, the nucleation process is somewhat more complicated. In these cases the first loop must expand to large distances prior to formation of the second loop since this process requires activation even when $R_1 = \infty$. Formation of the second loop, however, does not constrain either to remain on the nucleation slip plane since the effective energy of the APB between them, $\gamma_1 - \gamma_2$, is negative. These dislocations therefore repel and are free to cross slip under the influence of the high stress field of the source. Once removed from the latter these dislocations are immobile until the applied stress reaches τ_{IV}. Consequently a large percentage of the dislocations nucelated in these alloys do not contribute significantly to the plastic strain at low stresses although a small number of pairs presumably remain coupled and account for the nonlinear deformation stage which occurs prior to the onset of stage V. These same alloys exhibit pronounced stage II deformation when tested at higher temperatures. This behavior is readily explained by the normal temperature dependent

decrease in S_{NNN} which effects a decrease in both γ_1 and γ_2. As shown in Figure 16, the magnitude of the change is greatest for γ_2 so that at sufficiently high temperatures γ_2 becomes smaller than γ_1 and stepwise nucleation becomes possible.

This analysis is applicable to any stepwise nucleation process regardless of the details of the specific nucleation model chosen. Furthermore, as noted in the next section, operation of single-step nucleation processes such as Frank-Read sources leads to neither composition nor temperature dependent yield stress behavior. Further verification of this model may be obtained by reconsideration of the deformation behavior of alloys in which S_{NNN} has been decreased by quenching. Inspection of Figures 10 and 11 shows, as expected, that the yield and linear deformation behavior in these alloys are much more pronounced than in the case of the slowly cooled alloys although the presence of stage II is only suggested in these curves.

In summary, it has been demonstrated that the deformation behavior of the long range ordered alloys of iron and aluminum depends upon the type of dislocation nucleation possible at the temperature and composition in question.

Interaction of Superlattice Dislocations

The scientific literature abounds with work hardening models in which the distribution of dislocations is given as a function of some parameter, q, which increases steadily with strain (63), usually as $\epsilon^{\frac{1}{2}}$. Their form leads to the straightforward calculation of $\partial\sigma/\partial q$ and $\partial\epsilon/\partial q$, and hence to a differential equation for the flow stress curve. The micrographs presented previously suggest an obvious choice for q; the spacing between the straight screw segments. Dislocation interactions which might give rise to significant hardening on such a model will now be considered.

For alloys in which the linear hardening behavior is uncomplicated by nucleation difficulty, the schematic flow stress curve of Figure 25 may be considered as composed of three separate curves, each produced by dislocations of a different type. Stages I and III, the easy glide stages, are analogous to those observed in f.c.c. crystals and it is well known that their extent and hardening rates are extremely sensitive to specimen geometry and surface condition (63). Consideration will therefore be centered upon stages II and IV, the rapid linear hardening stages, for which the density of dipoles formed during the easy glide stages attains signif-

icant dimension. As Marcinkowski and Lakso (49) have pointed out, such dipoles may act as effective barriers to dislocation motion. These authors have analysed the contribution to hardening expected from dipole configurations and have concluded that vertical dipole spacings of about 100 Å are necessary to account for the hardening in Fe_3Si. The micrographs presented previously, however, suggest that when dipole locking or, in the case of double slip, secondary system dislocation pinning, is present the formation of bow outs of critical radius may be the process which governs further deformation. This possibility may be examined by consideration of the stability of superlattice dislocation loops.

As Marcinkowski and Leamy (65) have shown, the line tension of a single dislocation loop is given by

$$T = \tau_{R_c} R_c b \qquad (25)$$

where R_c is obtained from plots such as that shown in Figure 50, and τ_{R_c} is given by Equation 22. This formulation may be applied to the case of circular arcs as a lower limit approximation for T. Calculation of the stress required to maintain a superlattice dislocation at a given radius may therefore be applied directly to the case of the bow out problem for circular superlattice dislocation arcs. The energy of a super-

lattice dislocation loop of type 12(a) is given by

$$E_T = \sum_{i=1}^{i=4} \left\{ E_S(R_i) + \sum_{j}^{j=i-1} E_I(R_i,R_j) + \pi\tau b(R_i^2) \right\} + (R_1^2+R_3^2-R_4^2-R_2^2)\gamma_1 + (R_4^2-R_3^2)\gamma_2 \tag{26}$$

where the individual loop radii are numbered in sequence, the outer loop being number 1. In Equation 26 the self energy of the individual loops, E_S, is given by:

$$E_S(R_i) = \frac{\frac{2}{\nu} - 1}{2(\frac{1}{\nu} - 1)} \frac{\mu b^2}{2} R_i^2 \left[\ln(\frac{4R_i}{6}) - 2 \right] \tag{27}$$

while the interaction energies (83), $E_I(R_i,R_j)$, are given by:

$$E_I(R_i,R_j) = \frac{\frac{2}{\nu} - 1}{2(\frac{1}{\nu} - 1)} \mu b^2 (R_i+R_j) \left[(1 - \frac{k_{ij}^2}{2}) K_{ij} - E_{ij} \right] \tag{28}$$

where

$$k_{ij}^2 = \frac{4R_iR_j}{(R_i+R_j)^2} , \tag{29}$$

$$K_{ij} = \int_o^{\pi/2} \frac{d\phi}{(1-k_{ij}^2\sin^2\phi)^{1/2}}, \text{ and} \tag{30}$$

$$E_{ij} = \int_o^{\pi/2} (1-k_{ij}^2\sin^2\phi)^{1/2} d\phi \tag{31}$$

Solution of Equation 26 for R_c is only possible by numerical methods. For this reason E_T was obtained along with values of R_2, R_3, and R_4 for various fixed values of R_1, μ, b, γ_1, and γ_2 through the use of a standard least squares function minimization technique and an IBM 360 electronic computer. Values obtained in this manner yield E_T versus R_1 curves which are similar to that shown in Figure 50. Values of R_{1_c}, the critical loop radius, may be obtained from these curves for various stresses and alloy compositions. Plots of such values are shown in Figure 53. The curves which appear at low stresses apply to the case of type 12(a) loops while those at higher stresses correspond to loops of type 12(d) and 12(f), respectively, and were calculated by methods given elsewhere (65). For a given stress, pinning distances which are less than or equal to twice the R_{1_c} values given by these curves are sufficient to effectively stop the motion of the superlattice dislocation. In this connection, it should be noted that the effect of composition upon these values is negligible for the type 12(a) loop curves. The bow out process, therefore, cannot account for any compositional variation in either yield stress or work hardening rate.

The superlattice loop curves of Figure 51 also show

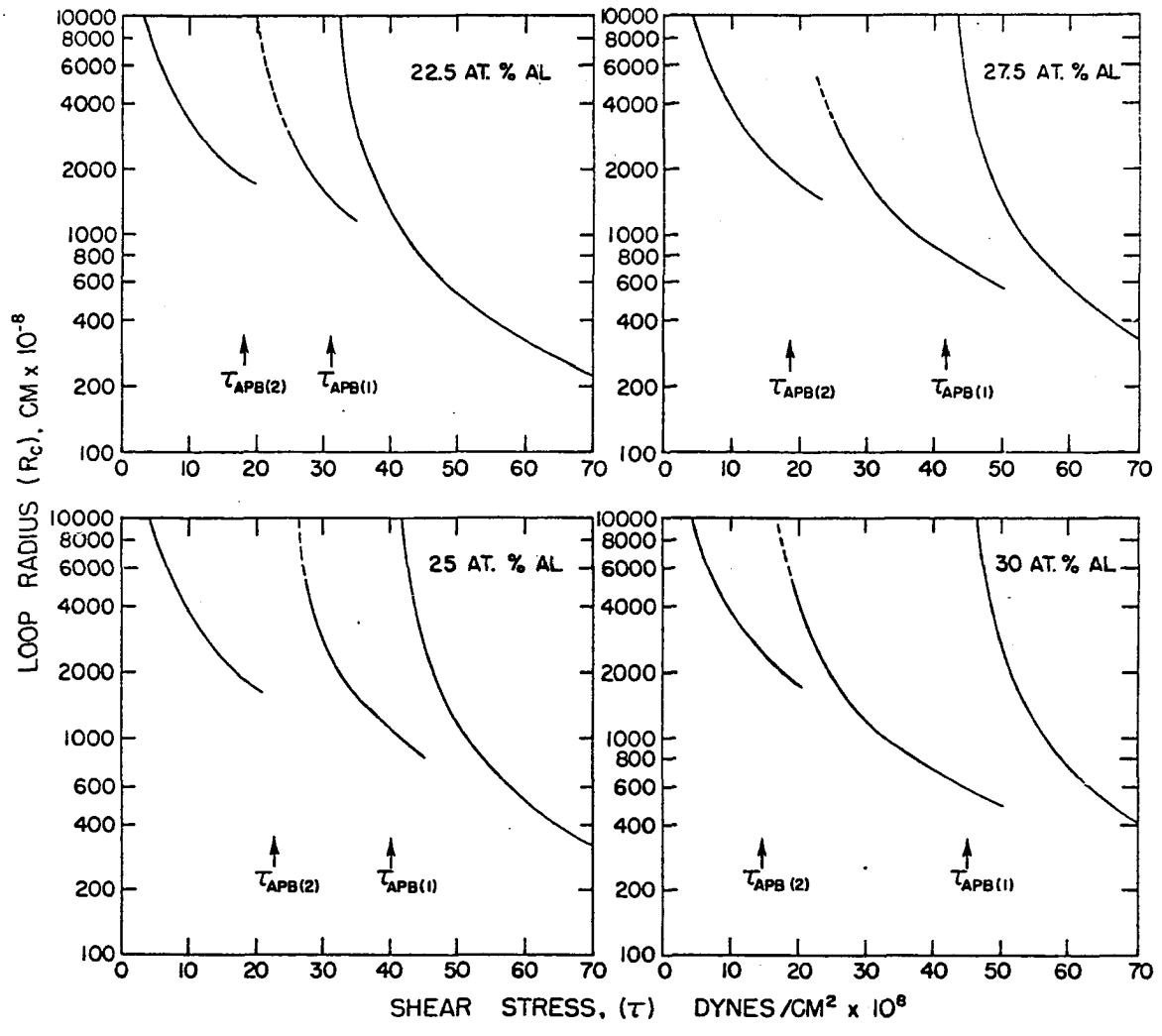

Figure 53. Critical radii of superlattice dislocation loops in Fe-Al alloys of various composition. Taken from left to right the curves correspond to loops of type 12(a), 12(d), and 12(f) respectively

that, in every case, loops of each type become unstable at stresses only slightly greater than those required for production of the corresponding APB. At stresses just above $\tau_{APB(2)}$, pinned dislocations of type 12(a) are expected to dissociate into mobile dislocations of type 12(d). These may then be pinned in stage IV and further decompose at stresses slightly greater than $\tau_{APB(1)}$ to produce single $\frac{1}{2}a_o\langle 111\rangle$ dislocations which are capable of cross slip.

The bow out process, as mentioned previously, is composition independent. On this model therefore, only a composition dependence of the rate at which pinning distances decrease with strain can account for the composition dependence of the hardening rates shown in Figure 19. In fact, such a composition dependence of $q(\epsilon)$, the pinning distance, is expected if pinning is produced by dipole locking of unlike dislocations. As Marcinkowski and Lakso (49) have shown, analysis of this process is complicated. In general however, the stress field of a superlattice dislocation increases with decreasing spacing, r. It follows that the incidence of pinning at a given stress for type 12(a) dislocations should attain a maximum at the stoichiometric composition. On this basis, the increase in $\left[\partial\sigma/\partial\epsilon\right]_{II}$ at the Fe_3Al composition is consistent

with the assumptions of this simple model. Furthermore, when preceded by stages I and II, the hardening rates of stage IV deformation are expected to be strongly influenced by the density of the locked arrays produced during the earlier stages. Thus $\left[\partial\sigma/\partial\epsilon\right]_{IV}$ is expected to increase with the extent of deformation in stage II, in agreement with the data of Figure 19. Finally, for the quenched alloys in which stage IV appears at the yield, $\left[\partial\sigma/\partial\epsilon\right]_{IV}$ should increase only slightly with increasing aluminum content, in general agreement with experiment.

Although the relative importance of the dipole locking and the bow out processes are difficult to assess without extensive and complex calculation, it seems certain that both contribute significantly to the high hardening rates observed in these alloys. The increase in hardening rate observed in crystals oriented for double slip, however, may be ascribed to the bow out process since in this case, the pinning points produced by dislocation intersection may be decomposed only by the formation of superlattice dislocation jogs of very high energy.

SUMMARY

The plastic deformation behavior of long range ordered alloys of iron and aluminum has been examined by means of compressive deformation testing and transmission electron microscopy. Alloys in the range of compositions studied, 22.0 to 30.6 at.% Al, exhibit marked temperature and composition variations in deformation behavior. These variations have been attributed to functional dependencies of the nucleation and interaction of superlattice dislocations upon temperature and antiphase boundary (APB) energies.

Single and polycrystalline flow stress curves indicate that, in general, low temperature deformation is accommodated by the motion of ordinary $\frac{1}{2}a_o\langle 111\rangle$ dislocations. Since these dislocations produce antiphase boundaries and cross slip rather easily, low temperature flow stress curves are characterized by high stress levels, short wavy slip lines, and nearly parabolic work hardening behavior. Deformation at higher temperatures is associated with the production of superlattice dislocations whose nucleation is aided by thermal fluctuations. The resultant flow stress curves are characterized by low yield stresses and from one to four linear work hardening stages. Further deformation in these

proceeds by the motion of ordinary $\frac{1}{2}a_o\langle 111\rangle$ dislocations and the flow stress curve assumes the familiar parabolic form. Transmission electron microscopical observations of deformed single-crystal sections indicate that the linear stages are produced by the interaction of superlattice dislocations of DO_3 (four APB coupled $\frac{1}{2}a_o\langle 111\rangle$ dislocations) or B2 (two APB coupled $\frac{1}{2}a_o\langle 111\rangle$ dislocations) type.

This unique deformation behavior has been treated theoretically on the basis of a simple model for superlattice dislocation nucleation and the work hardening processes have been discussed.

LITERATURE CITED

1. C. Sykes and J. W. Blampfylde, J. Iron and Steel Inst. 130, 389 (1934).

2. A. J. Bradley and A. H. Jay, Proc. Roy. Soc. A136, 210 (1932).

3. A. Taylor and R. M. Jones, J. Phys. Chem. Solids 6, 16 (1958).

4. H. J. McQueen and G. C. Kuczynski, Trans. Am. Inst. Min., Met., & Pet. Engrs. 215, 619 (1959).

5. A. Lawley and R. W. Cahn, J. Phys. Chem. Solids 20, 204 (1961).

6. R. G. Davies, J. Phys. Chem. Solids 24, 985 (1963).

7. L. Rimlinger, P. Antoine, and R. Faivre, Compt. Rend. 260, 148 (1956).

8. H. Sato, Sci. Rep. Tohoku Univ. A3, 13 (1951).

9. S. Matsuda, J. Phys. Soc. Japan 6, 131 (1951).

10. P. S. Rudman, Acta Met. 8, 321 (1960).

11. C. R. Houska, J. Phys. Chem. Solids 24, 95 (1963).

12. F. X. Kayser, [to be submitted for publication circa 1967].

13. H. Thomas, Z. Metallk. 41, 185 (1950).

14. G. Lütjering and H. Warlimont, Z. Metallk. 56, 1 (1965).

15. G. Lütjering and H. Warlimont, Acta Met. 12, 1460 (1964).

16. P. R. Swann and R. M. Fisher [to be published in J. Appl. Phys. circa 1967].

17. E. R. Morgan and V. F. Zackay, Metal Progress 68, 126 (1955).

18. W. Justusson, V. F. Zackay, and E. R. Morgan, Trans. Am. Soc. Metals 49, 905 (1956).

19. A. Lawley, J. A. Coll, and R. W. Cahn, Trans. Am. Inst. Min., Met., & Pet. Engrs. 218, 166 (1959).

20. R. W. Cahn and J. A. Coll, Acta Met. 9, 138 (1961).

21. Ben-Zion Weiss, Bull. Res. Counc. Israel 10F, 81 (1961).

22. A. Lawley, E. A. Vidoz, and R. W. Cahn, Acta Met. 9, 287 (1961).

23. Ben-Zion Weiss, J. Inst. Metals 92, 25 (1962).

24. R. G. Davies, Trans. Am. Inst. Min., Met., & Pet. Engrs. 230, 903 (1963).

25. N. S. Stoloff and R. G. Davies, Acta Met. 11, 1187 (1963).

26. R. G. Davies, Trans. Am. Inst. Min., Met., & Pet. Engrs. 227, 22 (1963).

27. N. S. Stoloff and R. G. Davies, Acta Met. 12, 473 (1964).

28. P. Mouturat, J. Moinet, M. Romeggio, G. Sainfort, and G. Cabane, J. Nucl. Mat. 19, 234 (1966).

29. F. X. Kayser, U.S. Atomic Energy Commission Tech. Rep., WADC-TR-57-298 [Wright Air Development Center, Wright Patterson AFB, Ohio]

30. F. X. Kayser, The effect of order on the plastic behavior of iron-aluminum alloys, (Unpublished paper presented at the AIME Symposium on the Effect of Ordering on Mechanical Properties, Cleveland, Ohio, October, 1958), Ames Laboratory, U.S. Atomic Energy Commission, Ames, Iowa (1958).

31. H. J. Leamy and F. X. Kayser, [to be submitted for publication in Trans. Am. Soc. Metals circa 1967].

32. R. Horiuchi, H. Yoshinaga, and S. Hama, Trans. Japan Inst. Metals 6, 123 (1965).

33. G. W. Ardley, Acta Met. 3, 525 (1955).

34. R. Horiuchi and H. Yoshinaga, Trans. Japan Inst. Metals 6, 131 (1965).

35. D. J. Schmatz and R. H. Bush [to be published in Acta Met. circa 1967].

36. J. S. Koehler and F. Seitz, J. Appl. Mechanics 14, A217 (1947).

37. N. Brown and M. Herman, Trans. Amer. Inst. Min., Met., & Pet. Engrs. 206, 1353 (1956).

38. M. J. Marcinkowski and N. Brown, Acta Met. 9, 764 (1961).

39. M. J. Marcinkowski and N. Brown, J. Appl. Phys. 33, 537 (1962).

40. K. Sumino, Sci. Rep. Tohoku Univ. A10, 283 (1958).

41. P. S. Rudman, Acta Met. 10, 253 (1962).

42. P. A. Flinn, Trans. Amer, Inst. Min., Met., & Pet. Engrs. 218, 145 (1960).

43. A. H. Cottrell, "Interaction of dislocations and solute atoms", in Relation of Properties to Microstructure, pp. 63-136, American Society for Metals, Cleveland, Ohio (1953).

44. A. E. Vidoz and L. M. Brown, Phil. Mag. 7, 1167 (1962).

45. P. S. Rudman, Acta Met. 10, 195 (1962).

46. N. Brown, Phil. Mag. 4, 693 (1959).

47. J. C. Fisher, Acta Met. 2, 9 (1954).

48. G. Lakso and M. J. Marcinkowski, [to be published in Acta Met. circa 1967].

49. M. J. Marcinkowski and G. Lakso, J. Appl. Phys. 38, 2124 (1967).

50. E. Kozlov and L. E. Popov, Soviet Phys.-Doklady 8, 928 (1964).

51. L. E. Popov and E. Kozlov, Fiz. Metal. Metalloved. 17, 755 (1964).

52. L. I. Vasil'yev and A. N. Orlov, Fiz. Metal. Metalloved. 15, 481 (1963).

53. L. I. Vasil'yev, Fiz. Metal. Metalloved. 20, 97 (1965).

54. M. J. Marcinkowski, "Theory and direct observation of antiphase boundaries and dislocations in superlattices" in Electron Microscopy and Strength of Crystals edited by G. Thomas and J. Washburn, pp. 333-441, Interscience Pub., New York (1963).

55. N. S. Stoloff and R. G. Davies, "The mechanical properties of ordered alloys" in Progress in Materials Science 13, edited by Bruce Chalmers, pp. 1-80, Pergamon Press, London (196).

56. M. J. Marcinkowski and R. M. Fisher, J. Appl. Phys. 34, 2135 (1963).

57. E. D. Gibson, U.S. Atomic Energy Commission Report IS-1631 Ames Laboratory, U.S. Atomic Energy Commission, Ames, Iowa (1967).

58. M. J. Marcinkowski and A. H. Lipsitt, Acta Met. 10, 95 (1962).

59. L. G. Heroux and C. P. Sullivan, Trans. Am. Soc. for Metals 56, 861 (1963).

60. E. Schmid and W. Boas, Kristallplastizität, Springer, Berlin (1936).

61. U. F. Kocks, Y. Nakada, and B. Ramaswami, Trans. Amer. Inst. Min., Met., & Pet. Engrs. 230, 1005 (1964).

62. M. J. Marcinkowski and H. Chessin, Phil. Mag. 10, 837 (1964).

63. F. R. N. Nabarro, Z. S. Basinski, and D. B. Holt, Adv. in Physics 13, 194 (1964).

64. H. J. Leamy, [to be published in Acta Met. circa 1967].

65. M. J. Marcinkowski and H. J. Leamy, [to be published in Phys. Stat. Sol. circa 1967].

66. F. Laves, Naturwissenshaften 30, 546 (1952).

67. M. J. Marcinkowski, [to be published in Phil. Mag. circa 1967].

68. T. Taoka and S. Sakata, Acta Met. 5, 61 (1957).

69. T. Taoka and R. Honda, J. Electron Microscopy 5, 19 (1957).

70. M. J. Whelan and P. B. Hirsch, Phil. Mag. 2, 1121 (1957).

71. J. D. Eshelby, W. T. Read, and W. Shockley, Acta Met. 1, 251 (1953).

72. A. K. Head, Phys. Stat. Sol. 6, 461 (1964).

73. A. J. E. Foreman, Acta Met. 3, 322 (1955).

74. L. K. France, C. S. Hartley, and C. N. Reid, Metal Science 1, 65 (1967).

75. A. K. Head, Phys. Stat. Sol. 19, 185 (1967).

76. F. C. Frank, "The Geometrical Thermodynamics of Surfaces" in Metal Surfaces pp. 1-16, American Society for Metals, Cleveland, Ohio (1953).

77. W. W. Mullins, "Solid Surface Morphologies Governed by Capillarity" in Metal Surfaces, pp. 17-67, American Society for Metals, Cleveland, Ohio (1963).

78. R. W. James, The Optical Principles of the Diffraction of x-Rays, G. Bell and Sons Ltd., London (1954).

79. A. Howie and M. J. Whelan, Proc. Roy. Soc. A263, 217 (1961).

80. B. H. Kear, Acta Met. 12, 555 (1964).

81. M. Victoria and A. E. Vidoz, Acta Met. 15, 676 (1967).

82. V. B. Kurfman, Trans. Amer. Inst. Min., Met., and Pet. Engrs. 236, 1050 (1966).

83. E. Kröner, Kontinummstheorie der Versetsungen und Eigenspannungen, Springer-Verlag, Berlin (1958).

84. H. J. Leamy and R. K. Trivedi, [to be published as a U.S. Atomic Energy Commission IS Report] Ames Laboratory, U.S. Atomic Energy Commission, Ames, Iowa, circa 1967.

85. H. J. Leamy, E. D. Gibson, and F. X. Kayser, [to be published in Acta Met. circa 1967].

ACKNOWLEDGEMENTS

The author acknowledges his gratitude to Professor F. X. Kayser whose encouragement and guidance during the course of this study were indispensable. He is also particularly indebted to Professor M. J. Marcinkowski for many hours of invaluable discussion concerning this work, and to G. E. Lakso for many helpful comments.

The author thanks E. D. Gibson and G. L. Stowe for their technical assistance, particularly with the production of single crystals; and D. E. Campbell for his assistance with the electron microscopy portion of this investigation. He also thanks the personnel of Analytical Chemistry Group I for performing the chemical analyses, and H. Baker for help with the metallographic work.

Finally, the author thanks his wife, Janet, for her selfless understanding and patience during the course of his graduate study.

APPENDIX A

As noted previously, the images of type 12(a) dislocations and dislocation dipoles as observed in TEM experiments do not permit unambiguous determination of the dislocation arrangements involved. For this reason, image intensity profiles were calculated from theory and compared with experiment. The purpose of this appendix is to present the results of a few such calculations and to discuss their application.

On the basis of a column approximation, Howie and Whelan (70) have developed a two beam dynamical theory of electron diffraction which includes the effect of absorption. The system of differential equations given by these authors may be written:

$$\frac{dT}{dz} + \pi i\left(s + \frac{d\alpha}{dz}\right)'T = \pi i\left(\frac{1}{t_e} + \frac{i}{\tau_e}\right)S \qquad (32a)$$

$$\frac{dS}{dz} - \pi i\left(s + \frac{d\alpha'}{dz}\right)S = \pi i\left(\frac{i}{t_e} + \frac{i}{\tau_e}\right)T \qquad (32b)$$

where T and S are the amplitudes of the transmitted and diffracted waves respectively, t_e is the extinction distance, τ_e is the absorption distance, s is the excitation error, and z is a Cartesian coordinate axis perpendicular to the foil surface. In these equations α' is a phase angle analogous to that defined by Equation 18 and is given by $\bar{g}\cdot\bar{R}$ where $\bar{R}$

describes the distortion associated with the defect considered. Since results obtained for screw and edge dislocations are qualitatively similar, only screw dislocation images have been considered in the calculations presented here. For screw dislocations $\bar{R}$ is given by:

$$\bar{R} = \frac{\bar{b}}{2\pi} \tan^{-1}\left[\frac{Z-Z_o}{x}\right] \qquad (33)$$

where z_o is the foil depth at which the dislocation is located, and x is the position of the column under consideration, measured along the foil surface perpendicular to both z and the dislocation line. Calculation of the intensities of the scattered and transmitted beams which emerge from the lower foil surface at a particular column position is accomplished by numerical integration (84) of Equations 32 over the foil thickness. Repetition of this procedure for a large number of columns yields profiles of the type shown in Figures 54, 55, and 56 where the intensities are plotted against an arbitrary vertical intensity scale and a horizontal scale graduated in units of one t_e.

The profiles shown in these figures were calculated for the simple case of $\bar{g}\cdot\bar{b} = 1$ at indicated values of X, the deviation parameter, which is given by $t_e s$. In every case the dislocation arrays were centered in a foil of thickness $6t_e$

so that corrections for surface relaxation were unnecessary, and absorption was accounted for by setting $\tau_e = 8t_e$.

Transmitted intensity profiles for several type 12(a) dislocation configurations are shown on the left of Figure 54. These profiles exhibit the contrast asymmetry which is produced by the superposition of like signed dislocation strain fields while the diffracted intensity profiles on the right exhibit the symmetry characteristic of dark field images in the X = 0 diffracting condition (70). For Fe_3Al, $t_e \sim 300$ Å (54) so that the equilibrium spacing, r_1, is approximately 0.2 t_e. Comparison of the top and bottom profiles in Figure 54, which correspond to $r_1 = 0.2\ t_e$ and $r_1 = 0$, respectively, shows that dislocations of type 12(a) and 12(b) produce similar images and thus would be difficult to distinguish by ordinary bright field observations.

The profiles of Figures 55 and 56 were calculated for type 12(b) dipole configurations of various geometry. Figure 55 contains profiles produced by dipoles of various degrees of overlap while Figure 56 contains profiles produced by the fully symmetric configuration at various values of X. In every case it may be noted that dipoles produce symmetric bright field images, regardless of the diffraction conditions.

In addition, Figure 55 shows that the wide dipole contrast observed in Figure 36 corresponds most closely with that of the nonoverlapping array while the narrow dipole contrast present in the same figure is evidently produced by an overlapping array.

APPENDIX B

As noted previously, the long range ordered alloys of iron and aluminum possess high elastic anisotropy (85). Thus, realistic calculation of the energies of dislocations in these alloys may be accomplished only by application of the equations of anisotropic elasticity (71). Equations 19, 20a and 20b are the required energy expressions and the appropriate energy factors are given in references (72) and (73) for the special cases of edge and screw dislocations. The anisotropic formulation facilitates the calculation of several other important parameters. For example, the dislocation width, ζ , in the Peierls sense is estimated to be:

$$\zeta = \tfrac{1}{2}Kd/C \qquad (34)$$

where K is the energy factor, d is the slip plane spacing, and C is the shear modulus on the slip plane in the direction of the Burger's vector. C values for the Burger's vector-slip plane combinations of interest may be calculated from the following equations:

$C = (c_{11}-c_{12}+c_{44})/3$ for $\langle 111\rangle$ $\{110\}$ (35a)

$C = c_{44}$ for $\langle 100\rangle$ $\{100\}$ and $\langle 100\rangle$ $\{110\}$ (35b)

$C = \tfrac{1}{2}(c_{11}-c_{12})$ for $\langle 110\rangle$ $\{110\}$ (35c)

Also, the relative mobilities of dislocations of various

types may be estimated by calculation of the ratio of the stress required to move the dislocation to the stress required to shear the slip plane rigidly. This quantity, S, is estimated to be:

$$S = (4\pi \zeta/b)\exp(-2\pi \zeta/b) \qquad (36)$$

Equation 34, it should be noted, is independent of $\bar{b}$ and applies only to dislocations for which $\bar{b}$ is equal to the shortest possible interatomic vector in the given direction. Dislocation widths and mobilities can not be calculated from this equation when $\bar{b}$ is greater than one interatomic vector. It seems certain, however, that dislocations of this type will possess larger widths and mobility factors. Equations 34 and 36 are admittedly approximate but should be of value when dislocations of different type in the same crystal are compared.

The procedures outlined above were employed in the calculation of 298°K values for K, E, ζ, S, and r for dislocations in Fe-Al alloys at composition intervals of 2.5 at.% Al. Since the results of these calculations are similar for all long range ordered alloys, only those for Fe_3Al are displayed in Table 1.

Table 1 shows that although fully disassociated <111> {110} dislocations of type 12(a) are of lower energy than

similar coalesed dislocations of type 12(b), the energy difference between the two is small. This table also shows that the experimentally observed dislocations, i.e. those of type 12(a), possess higher energies than several of the possible alternatives. This observation may be explained by consideration of the dislocation nucleation event. As noted previously, the nucleation of complete superlattice dislocations occurs via a stepwise process. On this basis, the energies of the individual dislocations which comprise the complete superlattice configuration must be compared. Although the magnitude of the APB energy terms which apply to this case is indeterminate, $\frac{1}{2}a_o\langle 111\rangle$ dislocations possess the lowest self energies. They are therefore the favored type.

Finally, a brief description of the method employed for calculation of the r and r_1 values shown in Figure 34 is in order. These calculations were performed with an IBM 360 computer programed to solve the equation

$$\frac{\partial E_{12(a)}}{\partial r} = 0 \qquad (37)$$

for r_1 at a fixed value of r. The values of r and r_1 were then used to evaluate $E_{12(a)}$, and this process was repeated for 2Å increments in r until a minimum in $E_{12(a)}$ was obtained.

Table 1. Energies, mobilities, and widths for dislocations in Fe_3Al

Dislocation type	b	Slip plane		K* dynes/cm^2 x10^o	E ergs/cm x10^{-4}	ζ ^{o}A	S	r ^{o}A	
12(a)	$\frac{1}{4}a_o\langle 111\rangle$	{110}	edge	11.857	134.30	2.110	0.6459	670	(r_1=205)
			screw	3.596	43.30	0.631	0.0539	202	(r_1= 61)
12(b)	$\frac{1}{2}a_o\langle 100\rangle$	{110}	edge	9.138	39.52	0.7051	0.6626	106	
			screw	13.270	56.73	1.024	0.4820	154	
12(b)	$\frac{1}{2}a_o\langle 100\rangle$	{100}	edge	7.073	30.83	0.772	0.5715	83	
			screw	13.270	56.73	1.448	0.2715	154	
12(b)	$\frac{1}{2}a_o\langle 111\rangle$	{110}	edge	11.857	144.79	---	---	580	
			screw	3.596	45.63	---	---	162	
12(c)	$a_o\langle 100\rangle$	{110}	edge	9.249	44.688	---	---	---	
			screw	12.630	61.024	---	---	---	
12(c)	$a_o\langle 100\rangle$	{100}	edge	7.591	36.384	---	---	---	
			screw	12.630	61.024	---	---	---	
12(c)	$\frac{1}{2}a_o\langle 110\rangle$	{110}	edge	13.270	31.30	---	---	---	
			screw	7.073	16.10	---	---	---	
12(c)	$a_o\langle 111\rangle$	{110}	edge	3.596	50.128	---	---	---	
			screw	11.857	105.28	---	---	---	

*Energy factor values were calculated from the elastic constants given in reference (85).

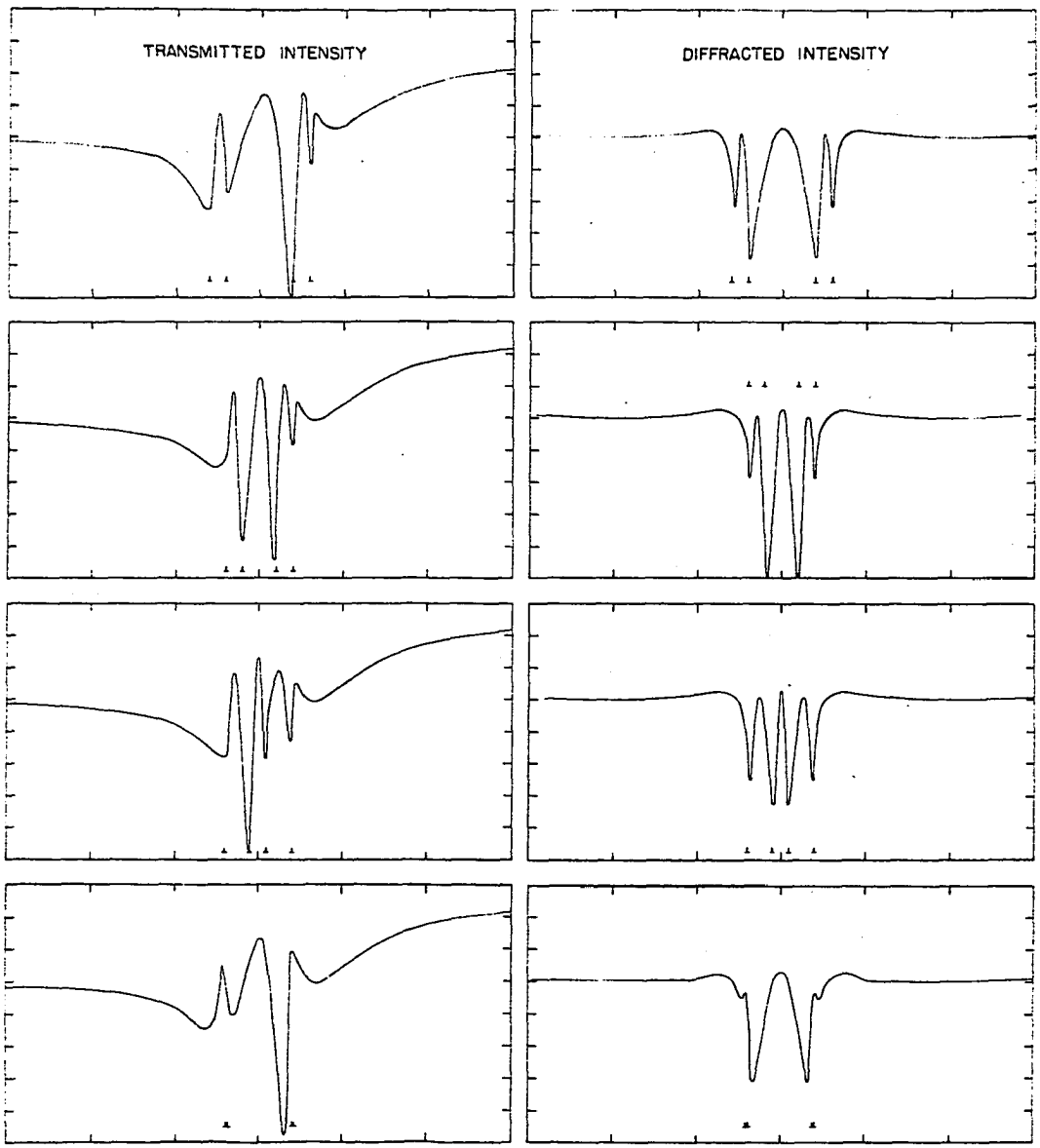

Figure 54. Calculated image profiles for type 12(a) dislocations in the X = 0 position. Dislocation positions are shown by ⊥.

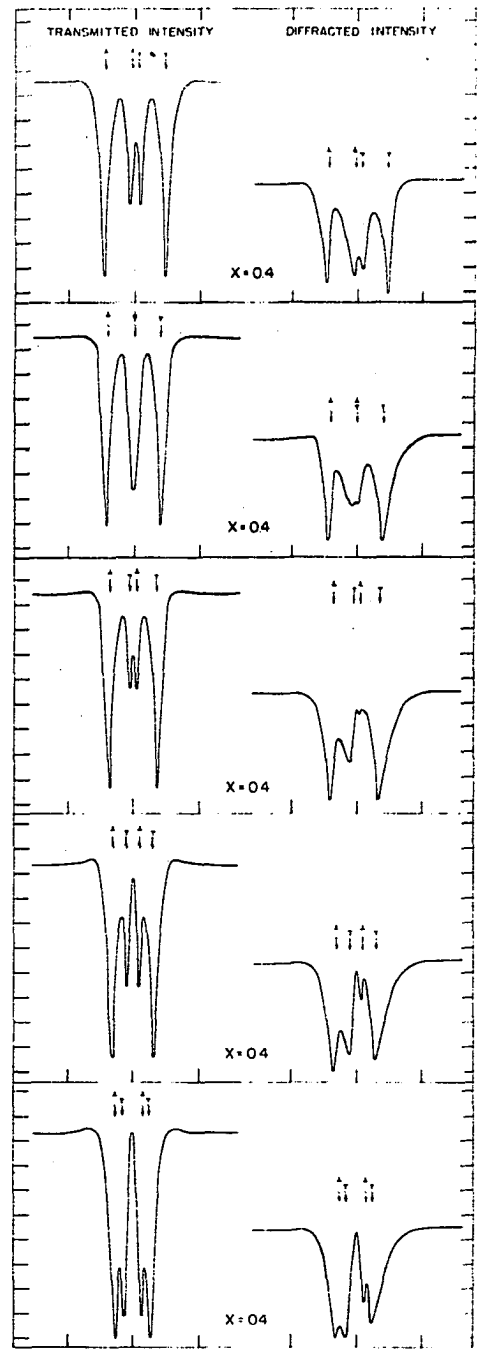

Figure 55. Calculated image profiles for dislocation dipoles of type 12(b)

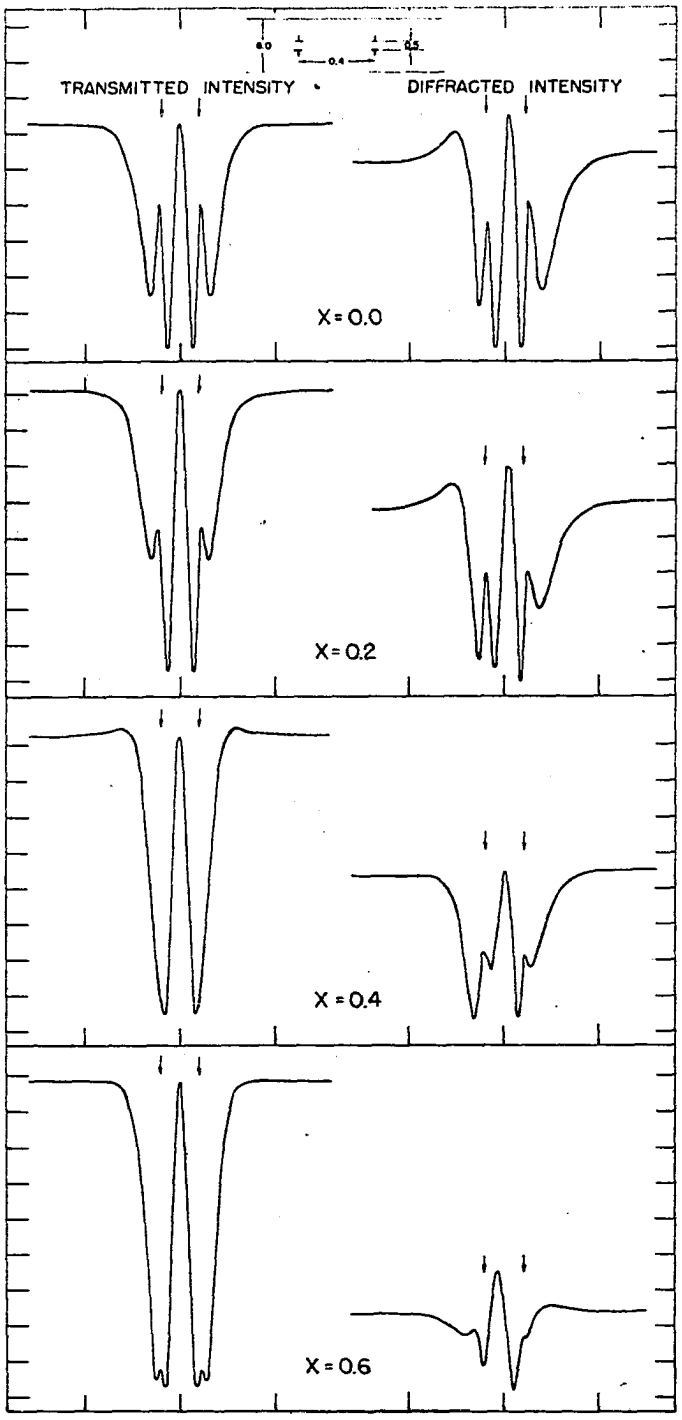

Figure 56. Calculated image profiles for symmetric superlattice dislocation dipoles at various values of X